Galerkin formulations of isogeometric shell analysis: Alleviating locking with Greville quadratures and higher-order elements

Z. Zou[1,6], T.J.R Hughes[1], M.A. Scott[2,6], R.A. Sauer[3,4,5], and E.J. Savitha[3]

[1]Oden Institute for Computational Engineering and Sciences, The University of Texas at Austin, Austin, TX USA
[2]Department of Civil and Environmental Engineering, Brigham Young University, Provo, UT USA
[3]Aachen Institute for Advanced Study in Computational Engineering Science, RWTH Aachen University, Aachen, Germany
[4]Department of Mechanical Engineering, Indian Institute of Technology, Kanpur, UP India
[5]Faculty of Civil and Environmental Engineering, Gdańsk University of Technology, Gdańsk, Poland
[6]Coreform LLC, Orem, UT, USA

2021-01-06

Abstract

We propose new quadrature schemes that asymptotically require only four in-plane points for Reissner-Mindlin shell elements and nine in-plane points for Kirchhoff-Love shell elements in B-spline and NURBS-based isogeometric shell analysis, independent of the polynomial degree p of the elements. The quadrature points are Greville abscissae associated with pth-order B-spline basis functions whose continuities depends on the specific Galerkin formulations, and the quadrature weights are calculated by solving a linear moment fitting problem in each parametric direction. The proposed shell element formulations are shown through numerical studies to be rank sufficient and to be free of spurious modes. The studies reveal comparable accuracy, in terms of both displacement and stress, compared with fully integrated spline-based shell elements, while at the same time reducing storage and computational cost associated with forming element stiffness and mass matrices and force vectors. The high accuracy with low computational cost makes the proposed quadratures along with higher-order spline bases, in particular polynomial orders, $p = 5$ and 6, good choices for alleviating membrane and shear locking in shells.

Keywords: Reissner-Mindlin shell theory; Kirchhoff-Love shell theory; isogeometric analysis; Greville abscissae; membrane and shear locking

1 Introduction

Shells have been dubbed the prima donnas of structural analysis by Ekkehard Ramm [1, 2], aptly describing their physically complex behavior and the challenges facing the development of numerical methods. In this paper we address problem of creating shell finite elements within the Isogeometric Analysis (IGA) paradigm, which, in structural mechanics, amounts to employing the same

kinematic description (i.e., specification of the displacement field) as that being utilized in the definition of geometry emanating from a Computer Aided Design (CAD) representation [3]. There are now a number of alternative geometric descriptions that fall into this category, such as B-splines, NURBS [4], S-splines [5], T-splines [6], U-splines [7], subdivision surfaces [8], etc. However, in industrial applications, B-splines and NURBS still dominate. At first glance, it would seem that IGA offers a fundamental advantage in shell modeling, namely, precise, or even exact, geometric representation, and this is no doubt important as it is well known that even small geometric imperfections can significantly affect results in thin shell buckling, indicating numerical approximations of geometry may also be a primary source of error. The advantages of IGA shell analysis have been demonstrated across a range of formulations and applications [9–13]. Nevertheless, there are still major barriers to creating effective IGA shell elements, and these are shared by traditional finite element methods of all kinds as well. Here our primary concern is on "locking phenomena," specifically, transverse shear locking and membrane-bending locking [14–17].

Transverse shear locking is not a consequence of curved shell geometry; it is present as well in flat plate and straight beam models that emanate from theories permitting transverse shear deformations, namely, Reissner-Mindlin plate theory and Timoshenko beam theory. There are a number of procedures in the literature that have been developed to address this phenomenon and we will not review them here [14, 15, 17–22]. We include this as an issue we must deal with because it also is present in transverse shear deformable shell theory, the most basic example of which is referred to as Reissner-Mindlin shell theory.

In our view, in the development of shell finite elements, the main challenge to overcome, and a remaining open problem, is membrane-bending locking. To the best of our knowledge, there is no general solution. It is apparent that curved, higher-order, traditional shell elements have not distinguished themselves heretofore because curvature is the root cause of membrane-bending coupling, hence locking. It is no wonder that in industrial software there is a heavy reliance on the lowest-order, four-node, quadrilateral shell elements, despite their inherently low accuracy, because they are typically flat, or almost flat, and minimize membrane-bending coupling within elements.

Various techniques have been proposed to overcome locking in both finite element analysis and IGA. These techniques include mixed formulations with displacement, strain and/or stress unknowns [16, 17, 23–27], reduced and selective integration techniques [14, 19, 28–30], assumed strain methods [12, 31–37], and enhanced assumed strain methods [38, 39]. Among these approaches, the reduced and selective integration methods dominate in commercial FEA codes due to their simplicity and efficiency. In the IGA community, a few research works [14, 30, 40] are dedicated to alleviating membrane and shear locking in shells, but none have achieved widespread acceptance. What we would like to have are simple, straightforward, IGA shell elements that would be candidates for inclusion in industrial scale and commercial general-purpose computer programs.

What we have pursued herein, is a study that starts with the most direct "primal" formulations of shell finite elements, and adheres to the finite element analysis orthodoxy of using high-enough accurate Gauss quadrature rules to ensure stability of the stiffness and mass matrices. We note, just as in the case of traditional finite elements, there are no exact quadrature rules for non-affine element geometries. So, sufficiently accurate Gauss rules are generally accepted as about the best one can do.

In addition to Reissner-Mindlin (RM) shell theory [17, 30], we also investigate Kirchhoff-Love (KL) shell theory [9], which precludes transverse shear deformation, in the same way as for Poisson-Kirchhoff plate theory and Bernoulli-Euler beam theory. This solves the problem of transverse shear locking ab initio for KL theory. Another ostensible advantage for KL shell elements based on the IGA paradigm is that they are "rotation free," only requiring displacement degrees of freedom, unlike RM elements, which additionally require rotation or director fields to be independently

interpolated. However, the implementation of boundary conditions involving rotations or bending moments requires more thought in KL theory than for RM theory.

Our study focuses on maximally smooth B-splines and NURBS elements of polynomial order $p = 2$, 3, 4, 5, and 6 for RM theory, and $p = 3$, 4, 5, and 6 for KL theory. The in-plane Gauss point patterns used are $(p+1) \times (p+1)$, or $(p+1)^2$ points per Bézier element. We think of these rules as "full Gauss quadrature." Very often, in the evaluation of shell finite element performance, displacements are compared to benchmark solutions, but stresses are not. In our experience, displacements often achieve acceptable accuracy while, at the same time, stresses do not, in fact, they are often completely unacceptable. For this reason, we advocate evaluating stresses and we do so herein. It is quite an eye opener.

Based on previous studies, we anticipated severe locking to occur for lower orders of p and mitigation of locking for higher orders of p, and indeed this was the case [41]. Furthermore, oscillations in stress fields for lower-order p are typically completely eliminated for higher orders of p. For orders $p = 5$ and 6, we found promising results for all tests considered. It seems higher-order elements cure a multitude of ills, but, of course, the obvious drawback is the computational cost associated with the very large number of Gauss quadrature points per element. It might also be thought that the number of degrees of freedom per element would be an additional concern for increasing p, but this is not the case in IGA because, for maximally smooth Bézier elements, the number of degrees of freedom is asymptotically the same for all p, $p = 1$, 2, 3, ... , etc., unlike for traditional finite elements, in other words, asymptotically, one control point per element. These orders of p may seem quite high, but that is probably due to lingering perceptions emanating from experience with classical finite element analysis. With one control point per element, the order of smooth spline elements is consonant with $p = 1$ in traditional finite element analysis. Given these observations, it seems that the cases $p = 5$ and 6 might provide robust capabilities of the type desired if, and only if, the cost of quadrature could be reduced to an acceptable level, independent of p. Developing this line of thought is the essential contribution of this paper.

From previous studies of integration rules for smooth, spline-based elements, it is known that full Gauss quadrature amounts to overkill [40, 42–49]. However, here we would like to reduce the number of points to be substantially less than full Gauss quadrature. A formulation that achieves what seems to be a minimum number of points is IGA collocation [50–56], which employs the strong residual form of the variational equations. Greville abscissae, or points, have distinguished themselves as efficient and effective locations for evaluation points of the residual. From the variational point of view, these evaluation points may also be viewed as quadrature points. Greville abscissae, which are in one-to-one correspondence with the control points (i.e., nodes), represent a "one-point" quadrature rule in the sense that there is only one quadrature point per control point. This was our first attempt [57], but in the context of Galerkin formulations of shell theories – to make a long story short, it was not effective for the stress. However, we found that Greville abscissae were effective, in comparison with full Gauss rules, if we redefined the space that determined the Greville abscissae to include, in addition to the basis functions, all the derivatives appearing in the weak form of the problem. To be specific, in the case of maximally smooth RM elements, to determine the Greville abscissae, we use the larger space of pth-order splines that are C^{p-2} continuous. Note that this is one order less continuity than for maximally smooth pth-order splines, which are C^{p-1} continuous. For maximally smooth KL elements, we use the still larger space of pth-order splines that are C^{p-3} continuous. In both cases, we then solve linear moment fitting equations in each parametric direction to obtain the weights, and then the two-dimensional quadrature points and weights are generated by a simple tensor product of the corresponding one-dimensional quantities. This results in, asymptotically, four in-plane quadrature points per RM shell element and nine in-plane quadrature points per KL shell element, which are fewer than those required by full Gauss quadrature for all the cases considered,

and substantially fewer in the higher-order cases, with concomitant reductions in computational cost. The accuracy of the Greville rules is generally commensurate with full Gauss quadrature, but asymptotic convergence rates for higher-order elements employing Greville rules are lower than for those utilizing Gauss rules because the Greville rules miss some higher-order monomials necessary for the full rate of convergence. Nevertheless, in situations such as these, the absolute accuracy attained by the higher-order Greville elements is still considerably greater than for the lower-order elements and more than adequate for practical applications. The concept of Greville points is general in that it extends to arbitrary unstructured spline meshes, such as for T-splines [6], S-splines [5], and U-splines [7]. Thus, we anticipate applications to these cases in forthcoming works.

The rest of the paper is organized as follows: Section 2 describes required spline concepts. Section 3 reviews the basic kinematic assumptions and variational forms for KL and RM shells. We then describe the Greville quadrature schemes in Section 4. Linear and geometrically nonlinear numerical calculations are presented in Section 5 followed by conclusions in Section 6.

2 Spline fundamentals

The Ith Bernstein polynomial of degree p on $[\xi_1, \xi_2]$ can be defined as

$$B_I^p(\xi) = \binom{p}{I-1} \left(\frac{\xi_2 - \xi}{\xi_2 - \xi_1}\right)^{p-I+1} \left(\frac{\xi - \xi_1}{\xi_2 - \xi_1}\right)^{I-1}, \tag{1}$$

where $\binom{p}{I-1} = \frac{p!}{(I-1)!(p-I+1)!}$ is a binomial coefficient. A univariate quadratic Bernstein basis on $[0, 1]$ is shown in Figure 1a. A degree p Bézier curve in $\mathbb{R}^d$ can be written as

$$\mathbf{x}(\xi) = \sum_{I=1}^{p+1} \mathbf{P}_I \, B_I^p(\xi), \qquad \xi \in [\xi_1, \xi_2], \tag{2}$$

where $\mathbf{P}_I \in \mathbb{R}^d$ is called a control point.

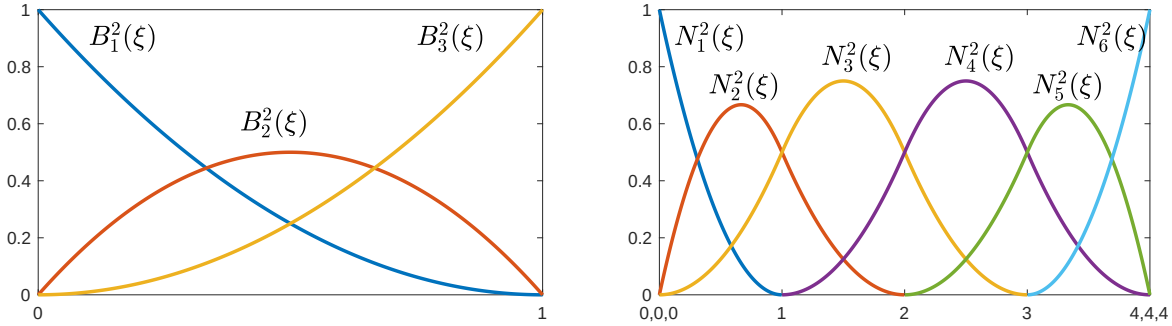

(a) Bernstein basis on $[0, 1]$.

(b) B-spline basis, $\Xi = \{0, 0, 0, 1, 2, 3, 4, 4, 4\}$.

Figure 1: A univariate quadratic Bernstein basis (a), a univariate quadratic C^1 B-spline basis (b).

A univariate B-spline basis can be defined by a knot vector $\Xi = \{\xi_1, \xi_2, \ldots, \xi_{n+p+1}\}$, which consists of a non-decreasing sequence of real numbers, $\xi_I \leq \xi_{I+1}, I = 1, \ldots, n+p+1$, where p is the degree of the B-spline basis and n is the number of basis functions. The Ith B-spline basis function

of degree p, denoted by $N_I^p(\xi)$, can be recursively defined as

$$N_I^0(\xi) = \begin{cases} 1, & \text{if} \quad \xi_I \leq \xi < \xi_{I+1} \\ 0, & \text{otherwise} \end{cases}$$

$$N_I^p(\xi) = \frac{\xi - \xi_I}{\xi_{I+p} - \xi_I} N_I^{p-1}(\xi) + \frac{\xi_{I+p+1} - \xi}{\xi_{I+p+1} - \xi_{I+1}} N_{I+1}^{p-1}(\xi).$$

B-spline basis functions are C^{p-m_I}-continuous across knot ξ_I, where m_I is the multiplicity of ξ_I in Ξ. A univariate quadratic B-spline basis is illustrated in Figure 1b.

A B-spline curve of degree p can be written as

$$\mathbf{x}(\xi) = \sum_{I=1}^{n} \mathbf{P}_I N_I^p(\xi), \quad \xi \in [\xi_1, \xi_{n+p+1}]. \tag{3}$$

For a degree p B-spline with knot vector Ξ, the Ith Greville abscissa [58] is given by

$$x_I = \frac{1}{p}(\xi_{I+1} + \xi_{I+2} + \cdots + \xi_{I+p}), \quad I = 1 \cdots n. \tag{4}$$

Figure 2 illustrates the Greville abscissae for a univariate quadratic B-spline with knot vector $\Xi = \{0, 0, 0, 1, 2, 3, 4, 4, 4\}$. Note that the number of Greville points is equal to the number of B-spline basis functions and therefore equal to the number of control points.

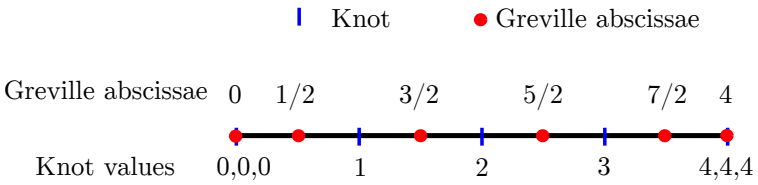

Figure 2: Greville abscissae corresponding to the knot vector $\Xi = \{0, 0, 0, 1, 2, 3, 4, 4, 4\}$.

A pth-degree NURBS curve can be represented as

$$\mathbf{x}(\xi) = \sum_{I=1}^{n} \mathbf{P}_I w_I R_I^p(\xi), \quad \xi \in [\xi_1, \xi_{n+p+1}], \tag{5}$$

where the NURBS basis function R_I^p is defined by

$$R_I^p(\xi) = \frac{N_I^p(\xi)}{W(\xi)}, \tag{6}$$

where $N_I^p(\xi)$ is the Ith p-degree B-spline basis function,

$$W(\xi) = \sum_{I=1}^{n} w_I N_I^p(\xi) \tag{7}$$

is a weighting function, and w_I is the weight corresponding to control point $\mathbf{P}_I$.

Note that unless it is necessary, the superscript p on the basis functions will be dropped hereafter for notation simplicity. Higher dimensional analogs to these spline concepts can be created using tensor products or more advanced construction schemes like hierarchical B-splines [59], T-splines [6], and U-splines [7].

3 Shell Formulation

3.1 Shell kinematics

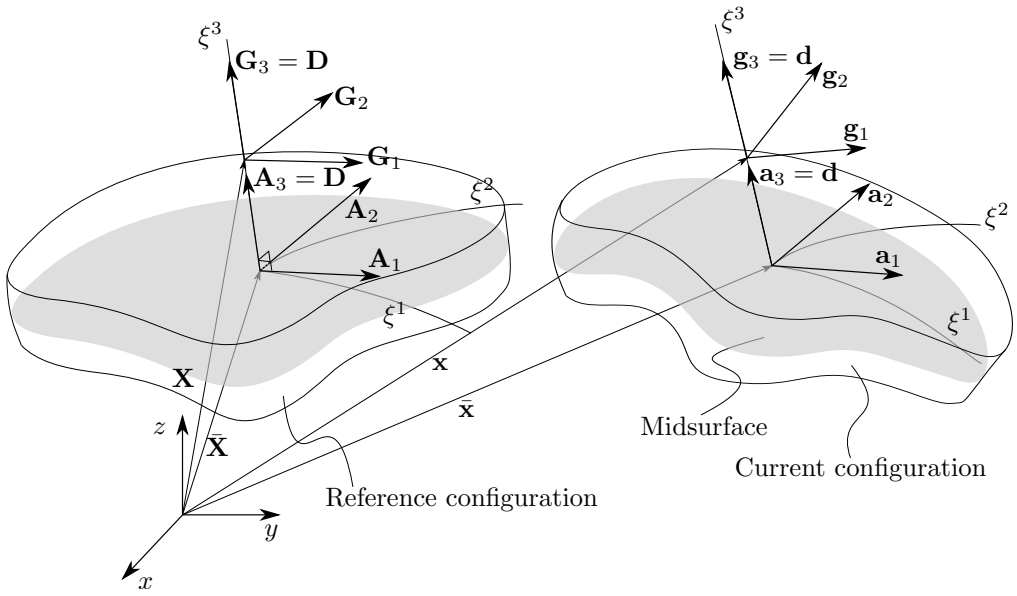

Figure 3: A schematic of shell kinematics.

The reference and current configurations of a shell-like body, as illustrated in Figure 3, can be parameterized as

$$\mathbf{X}(\xi^1, \xi^2, \xi^3) = \bar{\mathbf{X}}(\xi^1, \xi^2) + \xi^3 \mathbf{D}(\xi^1, \xi^2), \tag{8}$$

$$\mathbf{x}(\xi^1, \xi^2, \xi^3) = \bar{\mathbf{x}}(\xi^1, \xi^2) + \xi^3 \mathbf{d}(\xi^1, \xi^2), \tag{9}$$

where $-\frac{h}{2} \leq \xi^3 \leq \frac{h}{2}$, $\bar{\mathbf{X}}$ and $\bar{\mathbf{x}}$ denote the midsurfaces, and $\mathbf{D}$ and $\mathbf{d}$ denote the directors in the reference and current configurations, respectively. For conciseness, we will omit the parametric coordinate ξ^i in the following description, and adopt the established convention for Latin and Greek indices (i.e., $i = 1, 2, 3$ and $\alpha = 1, 2$).

The base vectors of the midsurface can be written as

$$\mathbf{A}_\alpha = \bar{\mathbf{X}}_{,\alpha}, \quad \mathbf{A}_3 = \mathbf{D} = \frac{\mathbf{A}_1 \times \mathbf{A}_2}{\|\mathbf{A}_1 \times \mathbf{A}_2\|}, \tag{10}$$

$$\mathbf{a}_\alpha = \bar{\mathbf{x}}_{,\alpha}, \quad \mathbf{a}_3 = \mathbf{d}, \tag{11}$$

where $(\cdot)_{,\alpha}$ denotes $\partial(\cdot)/\partial\xi^\alpha$. The covariant base vectors at any point in the shell continuum are defined as

$$\mathbf{G}_\alpha = \mathbf{X}_{,\alpha} = \bar{\mathbf{X}}_{,\alpha} + \xi^3 \mathbf{D}_{,\alpha} = \mathbf{A}_\alpha + \xi^3 \mathbf{D}_{,\alpha}\,, \quad \mathbf{G}_3 = \mathbf{X}_{,3} = \mathbf{D}, \tag{12}$$

$$\mathbf{g}_\alpha = \mathbf{x}_{,\alpha} = \bar{\mathbf{x}}_{,\alpha} + \xi^3 \mathbf{d}_{,\alpha} = \mathbf{a}_\alpha + \xi^3 \mathbf{d}_{,\alpha}\,, \quad \mathbf{g}_3 = \mathbf{x}_{,3} = \mathbf{d}. \tag{13}$$

The Green-Lagrange strain tensor $\mathbf{E}$ is defined as

$$\mathbf{E} = \frac{1}{2}(\mathbf{F}^{\mathrm{T}}\mathbf{F} - \mathbf{I}), \tag{14}$$

where $\mathbf{F} = \mathrm{d}\mathbf{x}/\mathrm{d}\mathbf{X}$ is called the material deformation gradient and $\mathbf{I}$ is the identity tensor. In components, it can be written as

$$E_{ij} = \frac{1}{2}(g_{ij} - G_{ij}), \tag{15}$$

where

$$g_{ij} = \mathbf{g}_i \cdot \mathbf{g}_j, \quad G_{ij} = \mathbf{G}_i \cdot \mathbf{G}_j. \tag{16}$$

Substituting (12) and (13) into (15) we get

$$E_{\alpha\beta} = \frac{1}{2}\left[(\mathbf{a}_\alpha \cdot \mathbf{a}_\beta + \xi^3 \mathbf{a}_\alpha \cdot \mathbf{d}_{,\beta} + \xi^3 \mathbf{d}_{,\alpha} \cdot \mathbf{a}_\beta) - (\mathbf{A}_\alpha \cdot \mathbf{A}_\beta + \xi^3 \mathbf{A}_\alpha \cdot \mathbf{D}_{,\beta} + \xi^3 \mathbf{D}_{,\alpha} \cdot \mathbf{A}_\beta)\right], \tag{17}$$

$$E_{\alpha 3} = \frac{1}{2}\left(\mathbf{a}_\alpha \cdot \mathbf{d} + \xi^3 \mathbf{d}_{,\alpha} \cdot \mathbf{d} - \mathbf{A}_\alpha \cdot \mathbf{D} - \xi^3 \mathbf{D}_{,\alpha} \cdot \mathbf{D}\right), \tag{18}$$

$$E_{33} = \frac{1}{2}\left(\mathbf{d} \cdot \mathbf{d} - \mathbf{D} \cdot \mathbf{D}\right), \tag{19}$$

where the higher-order terms with respect to ξ^3 are neglected [60].

The inextensibility assumption of the director, i.e. $\|\mathbf{d}\| = 1$, leads to

$$\mathbf{d} \cdot \mathbf{d} = \mathbf{D} \cdot \mathbf{D} = 1, \tag{20}$$

$$\mathbf{d}_{,\alpha} \cdot \mathbf{d} = \mathbf{D}_{,\alpha} \cdot \mathbf{D} = 0 \tag{21}$$

and according to the definition of $\mathbf{D}$ we also have $\mathbf{A}_\alpha \cdot \mathbf{D} = 0$ and $\mathbf{A}_\alpha \cdot \mathbf{D}_{,\beta} = -\mathbf{D} \cdot \mathbf{A}_{\alpha,\beta} = \mathbf{D}_{,\alpha} \cdot \mathbf{A}_\beta$. As a consequence, (17) to (19) become

$$E_{\alpha\beta} = \frac{1}{2}\left[(\mathbf{a}_\alpha \cdot \mathbf{a}_\beta - \mathbf{A}_\alpha \cdot \mathbf{A}_\beta) + \xi^3(\mathbf{a}_\alpha \cdot \mathbf{d}_{,\beta} + \mathbf{d}_{,\alpha} \cdot \mathbf{a}_\beta - 2\mathbf{D}_{,\beta} \cdot \mathbf{A}_\alpha\right], \tag{22}$$

$$E_{\alpha 3} = \frac{1}{2}\mathbf{a}_\alpha \cdot \mathbf{d}, \tag{23}$$

$$E_{33} = 0. \tag{24}$$

Rewriting the non-zero strains in Voigt notation results in the reduced Green-Lagrange strain vector

$$\tilde{\mathbf{E}} = \begin{bmatrix} \boldsymbol{\epsilon} + \xi^3 \boldsymbol{\kappa} \\ \boldsymbol{\gamma} \end{bmatrix}, \tag{25}$$

where $\boldsymbol{\epsilon}$, $\boldsymbol{\kappa}$ and $\boldsymbol{\gamma}$ are the membrane, bending, and transverse shear strains, respectively, which are defined as

$$\boldsymbol{\epsilon} = \begin{bmatrix} \epsilon_{11} \\ \epsilon_{22} \\ 2\epsilon_{12} \end{bmatrix}, \quad \boldsymbol{\kappa} = \begin{bmatrix} \kappa_{11} \\ \kappa_{22} \\ 2\kappa_{12} \end{bmatrix}, \quad \text{and} \quad \boldsymbol{\gamma} = \begin{bmatrix} \gamma_1 \\ \gamma_2 \end{bmatrix}, \tag{26}$$

where

$$\epsilon_{\alpha\beta} = \frac{1}{2}(\mathbf{a}_\alpha \cdot \mathbf{a}_\beta - \mathbf{A}_\alpha \cdot \mathbf{A}_\beta), \tag{27}$$

$$\kappa_{\alpha\beta} = \frac{1}{2}(\mathbf{a}_\alpha \cdot \mathbf{d}_{,\beta} + \mathbf{d}_{,\alpha} \cdot \mathbf{a}_\beta) - \mathbf{D}_{,\beta} \cdot \mathbf{A}_\alpha, \tag{28}$$

$$\gamma_\alpha = \mathbf{a}_\alpha \cdot \mathbf{d}. \tag{29}$$

For an RM shell, the current director is not necessarily perpendicular to the midsurface. Therefore, the shear strain γ_α may be non-zero. In contrast, the Kirchhoff-Love shell theory assumes the current director to be perpendicular to the midsurface, viz.,

$$\mathbf{d} = \frac{\mathbf{a}_1 \times \mathbf{a}_2}{\|\mathbf{a}_1 \times \mathbf{a}_2\|}. \tag{30}$$

In this case, the shear strain γ_α vanishes and equations (22) to (24) can be further simplified to

$$E_{\alpha\beta} = \frac{1}{2}\left[(\mathbf{a}_\alpha \cdot \mathbf{a}_\beta - \mathbf{A}_\alpha \cdot \mathbf{A}_\beta) + 2\xi^3(-\mathbf{a}_{\alpha,\beta} \cdot \mathbf{d} + \mathbf{A}_{\alpha,\beta} \cdot \mathbf{D})\right] \tag{31}$$

$$= \epsilon_{\alpha\beta} + \xi^3 \kappa_{\alpha\beta}, \tag{32}$$

$$E_{\alpha 3} = E_{33} = 0, \tag{33}$$

where now

$$\kappa_{\alpha\beta} = -\mathbf{a}_{\alpha,\beta} \cdot \mathbf{d} + \mathbf{A}_{\alpha,\beta} \cdot \mathbf{D}. \tag{34}$$

Note that compared to the bending strain for an RM shell shown in (28), the derivatives of the directors $\mathbf{d}$ and $\mathbf{D}$ are instead transferred to the tangent vectors $\mathbf{a}_\alpha$ and $\mathbf{A}_\alpha$ for a KL shell, as shown in (34).

3.2 Variational formulation

In this work, we restrict all attention to linear and geometrically nonlinear elastic problems. For those ends it is sufficient to assume a simple elastic constitutive equation, namely, the Saint-Venant Kirchhoff material, which can be written as

$$\tilde{\mathbf{S}} = \mathbf{C}\tilde{\mathbf{E}} \quad \text{on } \Omega, \tag{35}$$

where Ω is the continuum body with respect to the reference configuration, $\tilde{\mathbf{S}}$ is the second Piola-Kirchhoff stress in Voigt notation and $\mathbf{C}$ is the elasticity matrix defined in the curvilinear coordinate system, which can be calculated as

$$\mathbf{C} = \mathbf{T}^{\mathrm{T}} \begin{bmatrix} \mathbf{C}_{\mathrm{p}} & \mathbf{0} \\ \mathbf{0} & \mathbf{C}_{\mathrm{s}} \end{bmatrix} \mathbf{T}, \tag{36}$$

where $\mathbf{T}$, defined by (69) in Appendix A, is the strain transformation matrix from covariant components to local Cartesian components. Further

$$\mathbf{C}_{\mathrm{p}} = \frac{E}{1-\nu^2} \begin{bmatrix} 1 & \nu & 0 \\ \nu & 1 & 0 \\ 0 & 0 & \frac{1-\nu}{2} \end{bmatrix}, \quad \mathbf{C}_{\mathrm{s}} = \kappa_s \frac{E}{2(1+\nu)} \begin{bmatrix} 1 & 0 \\ 0 & 1 \end{bmatrix} \tag{37}$$

with Young's modulus E, Poisson's ratio ν, and shear correction factor κ_s which is set to be $\frac{5}{6}$ in this work, see [30, 61].

The total potential energy can be written as

$$\Pi(\mathbf{u}) = \frac{1}{2}\int_\Omega \tilde{\mathbf{E}}^{\mathrm{T}} \tilde{\mathbf{S}}\, \mathrm{d}\Omega - \int_\Omega \mathbf{u}^{\mathrm{T}} \mathbf{F}_{\mathrm{b}}\, \mathrm{d}\Omega - \int_{\Gamma_{\mathrm{t}}} \mathbf{u}^{\mathrm{T}} \mathbf{F}_{\mathrm{t}}\, \mathrm{d}\Gamma_{\mathrm{t}}, \tag{38}$$

where $\mathbf{F}_{\mathrm{b}}$ and $\mathbf{F}_{\mathrm{t}}$ are the body force and traction which act on Ω and the traction boundary Γ_{t}, respectively. For simplicity, we assume the loads $\mathbf{F}_{\mathrm{b}}$ and $\mathbf{F}_{\mathrm{t}}$ are independent of the body deformation.

The weak form of the equilibrium equation follows from the stationary point of the total potential function $\Pi(\mathbf{u})$ and can be written as

$$\delta\Pi(\mathbf{u},\delta\mathbf{u}) = \int_\Omega \delta\tilde{\mathbf{E}}^{\mathrm{T}}\mathbf{C}\tilde{\mathbf{E}}\,\mathrm{d}\Omega - \int_\Omega \delta\mathbf{u}^{\mathrm{T}}\mathbf{F}_{\mathrm{b}}\,\mathrm{d}\Omega - \int_{\Gamma_{\mathrm{t}}} \delta\mathbf{u}^{\mathrm{T}}\mathbf{F}_{\mathrm{t}}\,\mathrm{d}\Gamma_{\mathrm{t}} = 0. \tag{39}$$

The linearization of the above variational form of equilibrium yields

$$L[\delta\Pi(\mathbf{u},\delta\mathbf{u})] := \delta\Pi(\mathbf{u},\delta\mathbf{u}) + \Delta\delta\Pi(\Delta\mathbf{u},\delta\mathbf{u}) = 0, \tag{40}$$

where

$$\Delta\delta\Pi(\Delta\mathbf{u},\delta\mathbf{u}) = \int_\Omega \underbrace{\delta\tilde{\mathbf{E}}^{\mathrm{T}}\mathbf{C}\Delta\tilde{\mathbf{E}}}_{\text{material stiffness}} + \underbrace{\Delta\delta\tilde{\mathbf{E}}^{\mathrm{T}}\mathbf{C}\tilde{\mathbf{E}}}_{\text{geometric stiffness}}\,\mathrm{d}\Omega. \tag{41}$$

Here, the first and second variations of the reduced Green-Lagrange strain $\delta\tilde{\mathbf{E}}$ and $\Delta\delta\tilde{\mathbf{E}}$ are given as

$$\delta\tilde{\mathbf{E}} = \begin{bmatrix}\delta\boldsymbol{\epsilon} + \xi^3\delta\boldsymbol{\kappa}\\ \delta\boldsymbol{\gamma}\end{bmatrix} \quad \text{and} \quad \Delta\delta\tilde{\mathbf{E}} = \begin{bmatrix}\Delta\delta\boldsymbol{\epsilon} + \xi^3\Delta\delta\boldsymbol{\kappa}\\ \Delta\delta\boldsymbol{\gamma}\end{bmatrix}, \tag{42}$$

where the components of $\delta\boldsymbol{\epsilon}$, $\delta\boldsymbol{\kappa}$, $\delta\boldsymbol{\gamma}$, $\Delta\delta\boldsymbol{\epsilon}$, $\Delta\delta\boldsymbol{\kappa}$ and $\Delta\delta\boldsymbol{\gamma}$ can be obtained by taking the first and second variations of the strains in (27) to (29) as

$$\delta\epsilon_{\alpha\beta} = \frac{1}{2}(\delta\bar{\mathbf{x}}_{,\alpha}\cdot\bar{\mathbf{x}}_{,\beta} + \delta\bar{\mathbf{x}}_{,\beta}\cdot\bar{\mathbf{x}}_{,\alpha}), \tag{43}$$

$$\delta\kappa_{\alpha\beta} = \frac{1}{2}(\delta\bar{\mathbf{x}}_{,\alpha}\cdot\mathbf{d}_{,\beta} + \delta\bar{\mathbf{x}}_{,\beta}\cdot\mathbf{d}_{,\alpha} + \delta\mathbf{d}_{,\alpha}\cdot\bar{\mathbf{x}}_{,\beta} + \delta\mathbf{d}_{,\beta}\cdot\bar{\mathbf{x}}_{,\alpha}), \tag{44}$$

$$\delta\gamma_\alpha = \delta\bar{\mathbf{x}}_{,\alpha}\cdot\mathbf{d} + \delta\mathbf{d}\cdot\bar{\mathbf{x}}_{,\alpha}, \tag{45}$$

$$\Delta\delta\epsilon_{\alpha\beta} = \frac{1}{2}(\delta\bar{\mathbf{x}}_{,\alpha}\cdot\Delta\bar{\mathbf{x}}_{,\beta} + \delta\bar{\mathbf{x}}_{,\beta}\cdot\Delta\bar{\mathbf{x}}_{,\alpha}), \tag{46}$$

$$\Delta\delta\kappa_{\alpha\beta} = \frac{1}{2}(\delta\bar{\mathbf{x}}_{,\alpha}\cdot\Delta\mathbf{d}_{,\beta} + \delta\bar{\mathbf{x}}_{,\beta}\cdot\Delta\mathbf{d}_{,\alpha} + \delta\mathbf{d}_{,\alpha}\cdot\Delta\bar{\mathbf{x}}_{,\beta} + \delta\mathbf{d}_{,\beta}\cdot\Delta\bar{\mathbf{x}}_{,\alpha} \quad + \bar{\mathbf{x}}_{,\alpha}\cdot\Delta\delta\mathbf{d}_{,\beta} + \bar{\mathbf{x}}_{,\beta}\cdot\Delta\delta\mathbf{d}_{,\alpha}), \tag{47}$$

$$\Delta\delta\gamma_\alpha = \delta\bar{\mathbf{x}}_{,\alpha}\cdot\Delta\mathbf{d} + \delta\mathbf{d}\cdot\Delta\bar{\mathbf{x}}_{,\alpha} + \bar{\mathbf{x}}_{,\alpha}\cdot\Delta\delta\mathbf{d}. \tag{48}$$

The discretizations of the variations of the strains and the resulting stiffness matrices and internal force vectors are given in Appendix B for convenience. Interested readers are also referred to [30, 62] for more details.

For a KL shell, the transverse shear strains are zero. Therefore, (42) is reduced to

$$\delta\tilde{\mathbf{E}}^{KL} = \delta\boldsymbol{\epsilon} + \xi^3\delta\boldsymbol{\kappa} \quad \text{and} \quad \Delta\delta\tilde{\mathbf{E}}^{KL} = \Delta\delta\boldsymbol{\epsilon} + \xi^3\Delta\delta\boldsymbol{\kappa}. \tag{49}$$

The components of $\delta\boldsymbol{\epsilon}$ and $\Delta\delta\boldsymbol{\epsilon}$ for KL shells are the same as (43) and (46) for RM shells. The components of $\delta\boldsymbol{\kappa}$ and $\Delta\delta\boldsymbol{\kappa}$ are obtained by taking the first and second variations of the bending strain $\kappa_{\alpha\beta}$ in (34) as

$$\delta\kappa_{\alpha\beta} = -\delta\bar{\mathbf{x}}_{,\alpha\beta}\cdot\mathbf{d} - \bar{\mathbf{x}}_{,\alpha\beta}\cdot\delta\mathbf{d}, \tag{50}$$

$$\Delta\delta\kappa_{\alpha\beta} = -\delta\bar{\mathbf{x}}_{,\alpha\beta}\cdot\Delta\mathbf{d} - \Delta\bar{\mathbf{x}}_{,\alpha\beta}\cdot\delta\mathbf{d} - \bar{\mathbf{x}}_{,\alpha\beta}\cdot\Delta\delta\mathbf{d}. \tag{51}$$

for a KL shell. The discretized variations of the strains and their matrix formulations are given in Appendix C.

The elasticity matrix for a KL shell is reduced to

$$\mathbf{C}^{\mathrm{KL}} = \mathbf{T}^{\mathrm{KL}}\mathbf{C}_{\mathrm{p}}\mathbf{T}^{\mathrm{KL}} \tag{52}$$

where $\mathbf{T}^{\mathrm{KL}}$ is the in-plane strain transformation matrix from covariant components to local Cartesian components as defined in (70) in Appendix A.

4 Greville quadrature

4.1 Definition of Greville quadrature

Numerical integration of a univariate function, $f(x)$, can be written as

$$\int_{\hat{I}} f \mathrm{d}\hat{I} \approx \sum_{I=1}^{n} f(x_I) w_I, \tag{53}$$

where f is the integrand, $\hat{I}$ is the integral domain, $\{x_I\}_{I=1}^n$ are the n quadrature points, and $\{w_I\}_{I=1}^n$ are the corresponding weights. Given a univariate p-degree ($p \geq 2$) B-spline basis $\{N_I\}_{I=1}^n$ with an open knot vector $\Xi = \{\xi_1, \xi_2, \ldots, \xi_{n+p+1}\}$, we propose a way to determine the quadrature points and weights as follows: the Greville abscissae $\{x_I\}_{I=1}^n$, calculated from (4), are chosen to be the quadrature points, and the weights $\{w_I\}_{I=1}^n$ are determined so that the quadrature rule can exactly integrate all linear combinations of the univariate B-spline basis $\{N_I\}_{I=1}^n$. This can be accomplished by solving the following moment fitting system of equations

$$\begin{bmatrix} \int_{\hat{I}} N_1(\xi)\mathrm{d}\xi \\ \int_{\hat{I}} N_2(\xi)\mathrm{d}\xi \\ \vdots \\ \int_{\hat{I}} N_n(\xi)\mathrm{d}\xi \end{bmatrix} = \begin{bmatrix} N_1(x_1) & N_1(x_2) & \cdots & N_1(x_n) \\ N_2(x_1) & \ddots & \cdots & N_2(x_n) \\ \vdots & & \vdots & \vdots \\ N_n(x_1) & \cdots & \cdots & N_n(x_n) \end{bmatrix} \begin{bmatrix} w_1 \\ w_2 \\ \vdots \\ w_n \end{bmatrix}, \tag{54}$$

where the left-hand side contains the moments [63, 64], which are computed exactly using full Gauss quadrature. As the Greville abscissae are taken as quadrature points, we refer to this quadrature rule as the Greville quadrature. Figure 4 shows the Greville quadrature points and weights for a univariate quadratic B-spline basis associated with the knot vector $\Xi = \{0, 0, 0, 1, 2, 3, 4, 4, 4\}$.

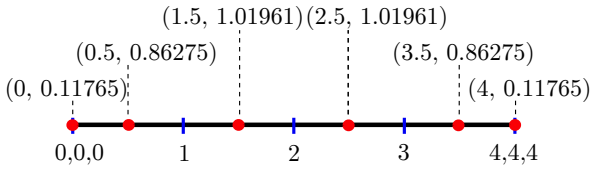

Figure 4: Greville quadrature points and weights for a quadratic B-spline basis with knot vector $\Xi = \{0, 0, 0, 1, 2, 3, 4, 4, 4\}$. Red dots denote the locations of the quadrature points and $(\cdot, \cdot)$ indicates $(x_i, w_i), i = 1, 2, \cdots, 6$.

Note that the Greville quadrature points and weights are calculated with respect to the global parametric domain of the patch. To utilize the method in existing FEA routines we can easily map these quadrature points into a parent element coordinate system through an affine mapping. The mapped quadrature weights can be obtained by dividing computed weights w_i by the determinant of the Jacobian matrix that maps the parametric coordinate system into the parent coordinate system. Figure 5 illustrates this process with the Greville points and weights given in Figure 4.

For a bivariate B-spline or NURBS basis, the quadrature points and weights are efficiently obtained through a simple tensor product of the corresponding univariate quantities. Figure 6 illustrates the distribution of Greville quadrature points for a bivariate B-spline basis that are generated through a tensor product of the univariate quantities shown in Figure 4. Detailed Greville

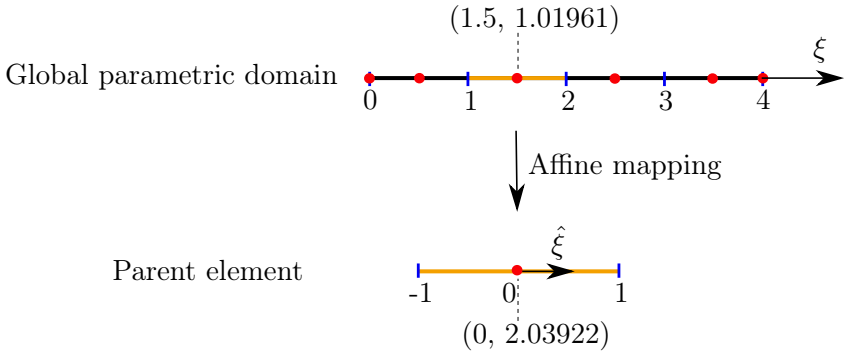

Figure 5: Schematic illustration of mapping the global Greville quadrature points and weights, given in Figure 4, from the parametric coordinate system (ξ) into the parent element coordinate system ($\hat{\xi}$).

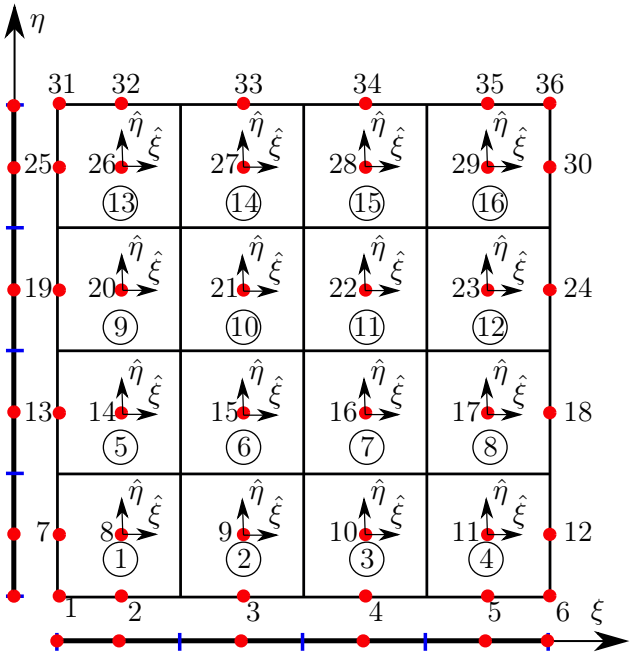

Figure 6: Greville quadrature point layout for a bivariate quadratic B-spline basis generated by a tensor product of the univariate quantities as shown in Figure 4. Quadrature points and elements are labeled with numbers and circled numbers, respectively. (ξ, η) and $(\hat{\xi}, \hat{\eta})$ indicate the global parametric and parent coordinate systems, respectively.

quadrature point and weight information in terms of the parent coordinate system is shown in Table 1.

Table 1: Parent element quadrature points and weights corresponding to Figure 6.

Element IDs	Point IDs	Points	Weights	Element IDs	Point IDs	Points	Weights
1	1	(-1, -1)	0.05536332179931	9	19	(-1, 0)	0.47981545559400
	2	(0, -1)	0.40599769319493		20	(0, 0)	3.51864667435602
	7	(-1, 0)	0.40599769319493				
	8	(0, 0)	2.97731641676278				
2	3	(0, -1)	0.47981545559400	10	21	(0, 0)	4.15840061514802
	9	(0, 0)	3.51864667435602				
3	4	(0, -1)	0.47981545559400	11	22	(0, 0)	4.15840061514802
	10	(0, 0)	3.51864667435602				
4	5	(0, -1)	0.40599769319492	12	23	(0, 0)	3.51864667435602
	6	(1, -1)	0.05536332179931		24	(1, 0)	0.47981545559400
	11	(0, 0)	2.97731641676278				
	12	(1, 0)	0.40599769319493				
5	13	(-1, 0)	0.47981545559400	13	25	(-1, 0)	0.40599769319493
	14	(0, 0)	3.51864667435602		26	(0, 0)	2.97731641676278
					31	(-1, 1)	0.05536332179931
					32	(0, 1)	0.40599769319493
6	15	(0, 0)	4.15840061514802	14	27	(0, 0)	3.51864667435602
					33	(0, 1)	0.47981545559400
7	16	(0, 0)	4.15840061514802	15	28	(0, 0)	3.51864667435602
					34	(0, 1)	0.47981545559400
8	17	(0, 0)	3.51864667435602	16	29	(0, 0)	2.97731641676278
	18	(1, 0)	0.47981545559400		30	(1, 0)	0.40599769319493
					35	(0, 1)	0.40599769319493
					36	(1, 1)	0.05536332179931

4.2 Greville quadrature for shells

The Greville quadrature proposed in Section 4.1 lays down a general framework for determining quadrature points and weights, i.e., preselecting the Greville points as the quadrature points and then generating the quadrature weights by solving a moment fitting equation system. However, for a specific isogeometric Galerkin formulation, a proper integration accuracy is necessary to ensure that the resulting linear equation system is stable and accurate. By construction, the Greville quadrature rule can exactly integrate all B-spline basis functions $\{N_I\}_{I=1}^n$ adopted in (54). Therefore, one can easily control the quadrature accuracy by using specific B-spline bases to build the quadrature rule. In this section, we propose different B-spline bases to build quadrature rules for KL and RMC shells.

Assuming the highest order of derivatives in the Galerkin formulation is k and the univariate B-spline basis along one of the parametric directions in the Galerkin formulation is $\left\{N_I^p\right\}_{I=1}^n$ with knot vector $\Xi = \{\xi_1, \xi_2, \ldots, \xi_{n+p+1}\}$, the Greville quadrature rules for analysis should be constructed in a way such that all basis functions $\left\{N_I^p\right\}_{I=1}^n$ and their derivatives of order less than or equal to k are integrated exactly. In other words, (54) should be satisfied for all functions in $\left\{N_{I,m}^p \,|\, 1 \leq I \leq n, 0 \leq m \leq k\right\}$. Notice that these functions are equivalent to a set of new B-spline

basis functions $\left\{\tilde{N}_I^p\right\}_{I=1}^{\tilde{n}}$, with knot vector $\tilde{\Xi}$ obtained by increasing the multiplicity of each interior knot of Ξ by k. It is preferable to use $\left\{\tilde{N}_I^p\right\}_{I=1}^{\tilde{n}}$ to build the Greville quadrature rules, because, in this way, we can avoid calculating the derivatives of the B-spline basis functions $\left\{N_I^p\right\}_{I=1}^{n}$ and the quadrature points are naturally the Greville quadrature points calculated from the knot vector $\tilde{\Xi}$. In what follows, we will use the notations

$$\mathcal{S}_0^p = \left\{N_I^p\right\}_{I=1}^{n} \quad \text{and} \quad \mathcal{S}_k^p = \left\{\tilde{N}_I^p\right\}_{I=1}^{\tilde{n}}, \quad k \in \{1, 2\}, \tag{55}$$

to indicate different B-spline bases.

According to the rules given above, for KL shells, the quadrature rule along one direction will be constructed with $\mathcal{S}_2^p$, and for RM shells, it will be constructed with $\mathcal{S}_1^p$. A two-dimensional quadrature rule is simply the tensor product of two one-dimensional quadrature rules as mentioned in Section 4.1. To distinguish these two quadrature rules for KL and RM shells, we will refer to them as GREVI-K and GREVI-R, respectively, hereafter. For a cubic B-spline basis with knot vector $\Xi = \{0, 0, 0, 0, 1, 2, 3, 4, 4, 4, 4\}$, the one-dimensional quadrature points and weights for GREVI-K and GREVI-R are illustrated in Figure 7. It is clear that the GREVI-R and GREVI-K rules, asymptotically, only involve two and three quadrature points in each parametric direction per element, respectively, regardless of the basis degrees. Consequently, only four and nine in-plane quadrature points are required for RM and KL shell elements.

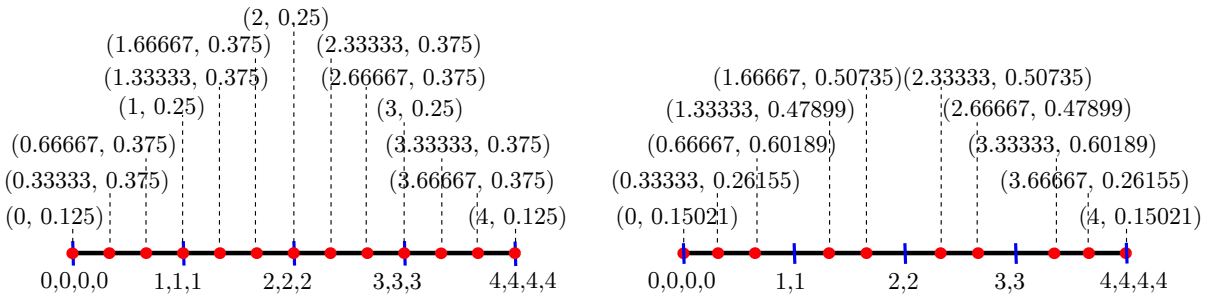

(a) GREVI-K. (b) GREVI-R.

Figure 7: Quadrature points and weights of GREVI-K and GREVI-R for a cubic B-spline basis with knot vector $\Xi = \{0, 0, 0, 0, 1, 2, 3, 4, 4, 4, 4\}$. Red dots denote the locations of the quadrature points, and $(\cdot, \cdot)$ indicates the global quadrature point and weight pair (x_i, w_i).

Remarks.

1. The Greville quadrature weights are not always positive for an arbitrary knot vector. For example, if a knot interval of Ξ is extremely small compared to adjacent intervals, it is possible for the GREVI-K and GREVI-R quadrature rules to exhibit negative weights locally. Quadrature rules with negative weights are prone to instability and not preferred in engineering analysis. In this work we confine ourselves to uniform knot vectors. With uniform knot vectors we only see negative weights for the GREVI-K rule with $p = 4$. How to effectively remove the negative weights for arbitrary knot vectors is non-trivial and will be addressed in future work.

2. For $p = 2$, the multiplicities of the interior knots of the resulting knot vector $\tilde{\Xi}$ will be three for GREVI-K. Therefore, each element is an independent Bézier patch and the quadrature rule needs to be determined on the element level through (54). The resulting quadrature points will be distributed by the Simpson's rule, and unfortunately the two coincident quadrature points at

the element interface can not be combined into one point due to the discontinuous second order derivatives [49]. As a result, the number of quadrature points will be the same as for full Gauss quadrature and thus we will not explore the case of $p = 2$ for GREVI-K further.

4.3 Stability and accuracy of Greville quadrature

Numerical stability requires that the discrete Galerkin forms be rank sufficient under quadrature. Reduced quadrature rules used in traditional C^0-continuous FEA may lead to unstable systems, i.e., the numerically integrated stiffness matrix being rank-deficient and the system producing spurious zero-energy modes. The proposed Greville quadrature schemes can be regarded as reduced quadrature rules for shell analysis utilizing higher-order smooth spline discretizations. In this section, we investigate their stability and accuracy by studying the generalized eigenvalue problem in the context of a flat plate discretized with KL shell elements. This problem is critical because the flat geometry uncouples membrane and bending behavior and the treatment of each does not inherit stabilization from the other. As the transverse shear strains are always coupled with the bending strains for RM shells, sorting out the shear modes alone is challenging. So we studied the bending and shear modes together with RM shells, which shows that the proposed quadratures are free of spurious modes. Detailed results are omitted for conciseness.

4.3.1 The generalized eigenvalue problem

The discrete generalized eigenvalue problem takes the form

$$(\mathbf{K} - \lambda \mathbf{M})\mathbf{\Psi} = \mathbf{0}, \tag{56}$$

where λ is the eigenvalue corresponding to the eigenvector $\mathbf{\Psi}$, $\mathbf{K}$ is the material stiffness matrix of the KL shell described in Section 3, and $\mathbf{M}$ is the mass matrix with

$$M_{IJ} = t \int_A \rho N_I N_J \, \mathrm{d}A, \tag{57}$$

where t is the shell thickness and ρ the mass density. For the displacement-based KL shell formulation considered above, both $\mathbf{K}$ and $\mathbf{M}$ are $n_{\text{eq}} \times n_{\text{eq}}$ square matrices, where n_{eq} denotes the number of degrees of freedom. In this case, there exist n_{eq} eigenvalues and corresponding eigenvectors that satisfy (56). For a given mode, finite element error estimates give the following error bound in terms of the relative error of the eigenvalues [65, 66],

$$\frac{\lambda_l^h - \lambda_l}{\lambda_l} \leq c \left(h \lambda_l^{1/(2k)} \right)^{2(p+1-k)}, \tag{58}$$

where λ_l and λ_l^h are the lth analytical and FEA eigenvalues, respectively, h is the mesh size, k is the highest order of derivatives and c is a constant independent of h and λ_l.

We examine the generalized eigenvalue problem (56) for a square elastic plate with Young's modulus $E = 1000$, Poisson's ratio $\nu = 0$, mass density $\rho = 1000$, thickness $t = 0.1$, and edge length $L = 10$. As the geometry is a flat plate, the bending and membrane stiffness are decoupled. Therefore, the bending and membrane modes can be explored separately by applying different constraints

$$u_x = u_y = 0 \quad \text{and} \quad u_z = 0, \tag{59}$$

which result in three out-of-plane and three in-plane rigid body modes, respectively, as shown in Figures 8a and b. In these cases, the stiffness matrix $\mathbf{K}$ is positive semi-definite and the mass matrix

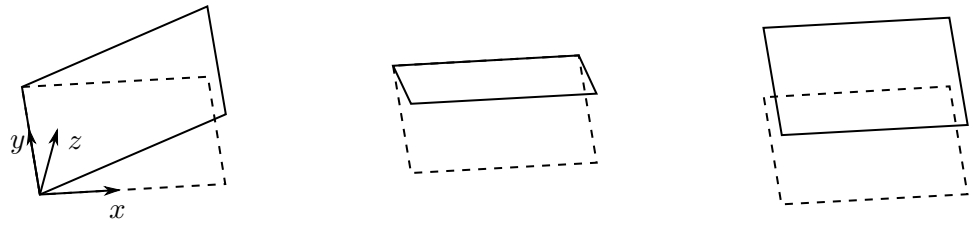

(a) Out-of-plane rigid body modes for $u_x = u_y = 0$.

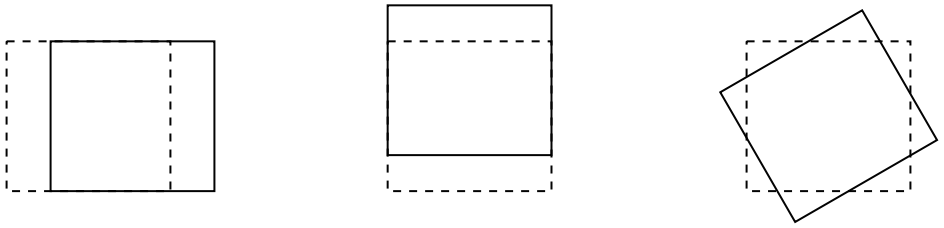

(b) In-plane rigid body modes for $u_z = 0$.

Figure 8: Rigid body modes. Dashed lines indicate initial configurations.

M is positive definite. As a consequence, all eigenvalues should be non-negative real numbers, and the number of zero eigenvalues for each case should be equal to the number of rigid body modes.

Table 2: Reference eigenvalues from full Gauss quadrature with 64×64 maximally smooth elements, $p = 7$.

Mode type	λ_1	λ_2	λ_3
Membrane	6.9670413427e-02	6.9670413427e-02	7.5020070779e-02
Bending	2.0862971829e-05	4.1713658653e-05	4.1713659232e-05

Numerical results with the proposed GREVI-K and GREVI-R quadratures verify that the resulting bending and membrane stiffness matrices have rank deficiency 3 for all mesh sizes and degrees considered, $p = 3$ to 6 for bending and $p = 2$ to 6 for membrane. Additionally, Figure 9 illustrates the convergence of the relative error of the three smallest non-zero eigenvalues. The reference eigenvalues λ_l, $l \in \{1, 2, 3\}$, given in Table 2, are obtained from full Gauss quadrature with 64×64 maximally smooth elements with $p = 7$. Note that here we use GREVI-R for the membrane modes because only first derivatives are required but use GREVI-K for the bending modes as second derivatives are present. Figures 9a, c and e illustrate that all three eigenvalues with GREVI-R converge to the reference solutions. The convergence rates are 4 for $p = 2, 3$ and approximately 5 for $p = 4$ to 6. According to (58), the convergence rate is optimal for $p = 2$. Figures 9b, d and h show that GREVI-K achieves optimal rates for $p = 3$. For $p \geq 4$, the convergence rates are not optimal but they are all greater than 4 before the differences between λ_l^h and λ_l stall at about 10^{-13}, which is close to machine precision. We note that [65] gives an error estimate for numerical integration in the context of C^0-continuous finite elements. However, this error estimate seems conservative for higher-order continuous IGA and cannot explain the convergence rates we see here for eigenvalue analyses and that we will see later for shell benchmarks. The same observation has been made in [49]. Interested readers are referred to [49, 65] for more details.

Tables 3 to 4 list the smallest 50 non-zero eigenvalues corresponding to the membrane modes for $p = 2$ and 3 with 50×50 elements. As can be seen, the eigenvalues produced by the GREVI-R

quadrature scheme are almost identical to those obtained from full Gauss quadrature, which shows that the proposed GREVI-R rule is free of spurious modes [40, 49, 57]. For higher p the accuracy gets even better and the results are omitted here. Similar observation can be obtained for GREVI-K with the bending modes as shown in Tables 5 to 6 for $p = 3$ and 4. Note that the eigenvalues in these tables are sorted in an ascending order.

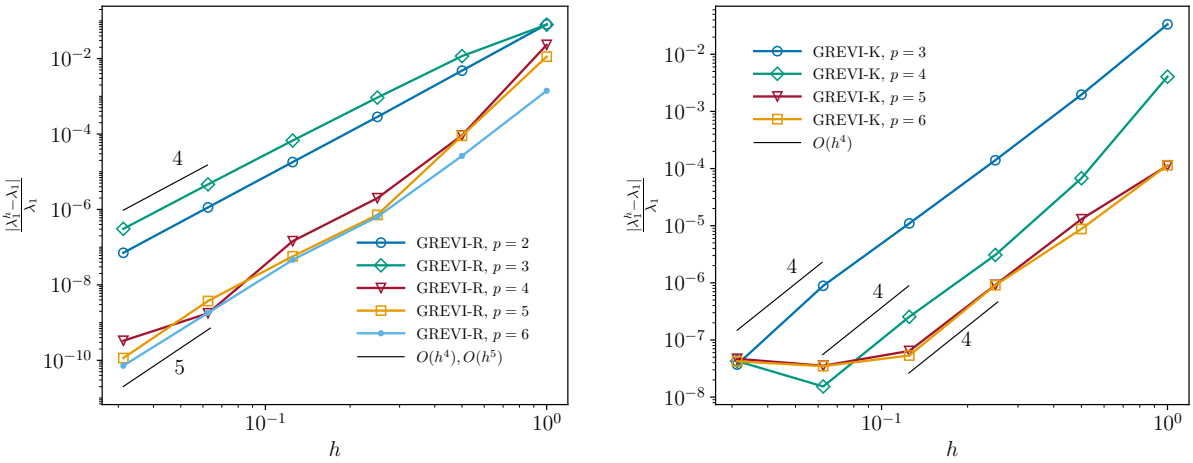

(a) First membrane mode.

(b) First bending mode.

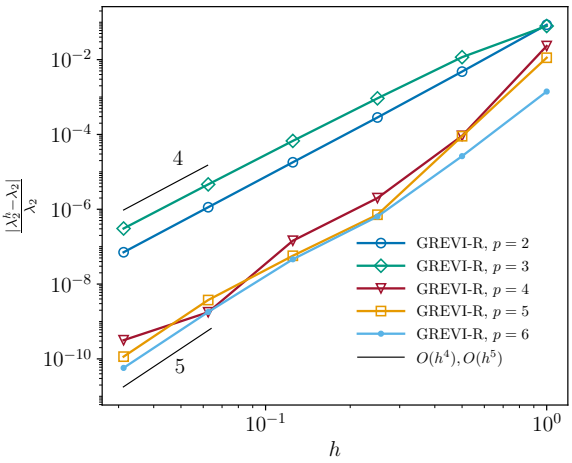

(c) Second membrane mode.

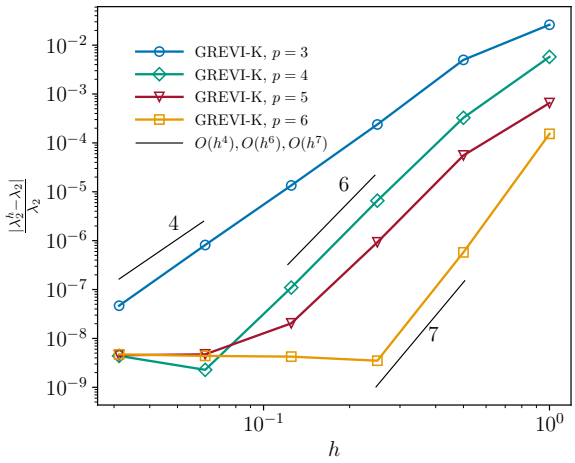

(d) Second bending mode.

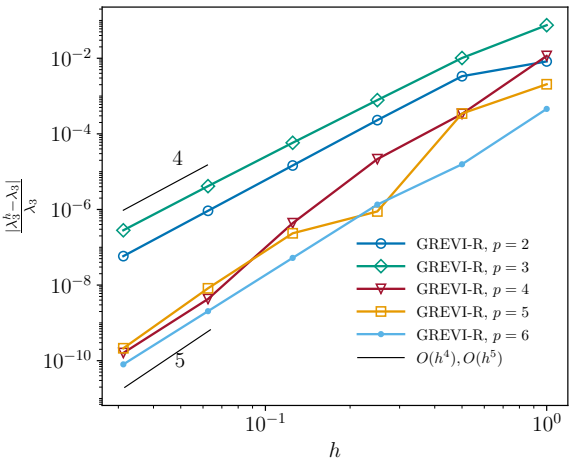

(e) Third membrane mode.

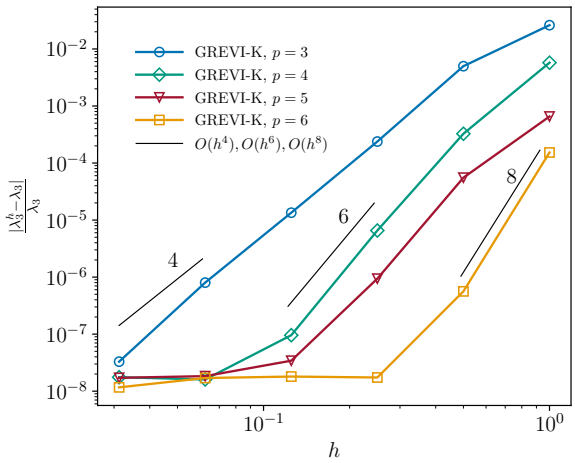

(f) Third bending mode.

Figure 9: Convergence of the relative error of the three smallest eigenvalues: membrane modes with GREVI-R (left column) and bending modes with GREVI-K (right column). Reference eigenvalues λ_l, $l \in \{1, 2, 3\}$, obtained from full Gauss quadrature with 64×64 maximally smooth elements, $p = 7$, are tabulated in Table 2.

Table 3: List of the smallest 50 non-zero eigenvalues corresponding to membrane modes from full Gauss quadrature and GREVI-R, $p = 2$ and 50×50 maximally smooth elements.

l	GAUSS	GREVI-R	ratio	l	GAUSS	GREVI-R	ratio
1	6.96704e-02	6.96704e-02	1.00000	26	7.94834e-01	7.94832e-01	1.00000
2	6.96704e-02	6.96704e-02	1.00000	27	7.94834e-01	7.94832e-01	1.00000
3	7.50201e-02	7.50201e-02	1.00000	28	8.17504e-01	8.17503e-01	1.00000
4	9.86960e-02	9.86960e-02	1.00000	29	8.88266e-01	8.88264e-01	1.00000
5	9.86960e-02	9.86960e-02	1.00000	30	8.88266e-01	8.88264e-01	1.00000
6	9.86961e-02	9.86961e-02	1.00000	31	8.88267e-01	8.88266e-01	1.00000
7	1.83254e-01	1.83254e-01	1.00000	32	9.67027e-01	9.67024e-01	1.00000
8	1.83254e-01	1.83254e-01	1.00000	33	9.67027e-01	9.67024e-01	1.00000
9	2.25664e-01	2.25664e-01	1.00000	34	1.05281e+00	1.05281e+00	1.00000
10	3.11077e-01	3.11077e-01	1.00000	35	1.05281e+00	1.05281e+00	1.00000
11	3.11077e-01	3.11077e-01	1.00000	36	1.10888e+00	1.10888e+00	1.00000
12	3.26054e-01	3.26054e-01	1.00000	37	1.11267e+00	1.11266e+00	1.00000
13	3.37540e-01	3.37539e-01	1.00000	38	1.12017e+00	1.12016e+00	0.99999
14	3.94784e-01	3.94784e-01	1.00000	39	1.20535e+00	1.20535e+00	1.00000
15	3.94784e-01	3.94784e-01	1.00000	40	1.20535e+00	1.20535e+00	1.00000
16	3.94784e-01	3.94784e-01	1.00000	41	1.27578e+00	1.27576e+00	0.99999
17	4.53845e-01	4.53844e-01	1.00000	42	1.31309e+00	1.31308e+00	0.99999
18	5.15234e-01	5.15233e-01	1.00000	43	1.31309e+00	1.31308e+00	0.99999
19	5.19052e-01	5.19052e-01	1.00000	44	1.39427e+00	1.39426e+00	0.99999
20	5.19052e-01	5.19052e-01	1.00000	45	1.41493e+00	1.41492e+00	1.00000
21	6.24449e-01	6.24447e-01	1.00000	46	1.53668e+00	1.53667e+00	0.99999
22	6.31537e-01	6.31536e-01	1.00000	47	1.57533e+00	1.57531e+00	0.99999
23	6.31537e-01	6.31536e-01	1.00000	48	1.57915e+00	1.57913e+00	0.99999
24	7.23353e-01	7.23351e-01	1.00000	49	1.57915e+00	1.57913e+00	0.99999
25	7.72993e-01	7.72992e-01	1.00000	50	1.57915e+00	1.57914e+00	1.00000

Table 4: List of the smallest 50 non-zero eigenvalues corresponding to membrane modes from full Gauss quadrature and GREVI-R, $p = 3$ and 50×50 maximally smooth elements.

l	GAUSS	GREVI-R	ratio	l	GAUSS	GREVI-R	ratio
1	6.96704e-02	6.96705e-02	1.00000	26	7.94828e-01	7.94850e-01	1.00003
2	6.96704e-02	6.96705e-02	1.00000	27	7.94828e-01	7.94850e-01	1.00003
3	7.50201e-02	7.50201e-02	1.00000	28	8.17498e-01	8.17519e-01	1.00003
4	9.86960e-02	9.86961e-02	1.00000	29	8.88264e-01	8.88271e-01	1.00001
5	9.86960e-02	9.86961e-02	1.00000	30	8.88264e-01	8.88271e-01	1.00001
6	9.86960e-02	9.86961e-02	1.00000	31	8.88264e-01	8.88271e-01	1.00001
7	1.83254e-01	1.83254e-01	1.00000	32	9.67011e-01	9.67069e-01	1.00006
8	1.83254e-01	1.83254e-01	1.00000	33	9.67011e-01	9.67069e-01	1.00006
9	2.25664e-01	2.25665e-01	1.00001	34	1.05281e+00	1.05283e+00	1.00002
10	3.11076e-01	3.11079e-01	1.00001	35	1.05281e+00	1.05283e+00	1.00002
11	3.11076e-01	3.11079e-01	1.00001	36	1.10887e+00	1.10892e+00	1.00005
12	3.26053e-01	3.26056e-01	1.00001	37	1.11263e+00	1.11277e+00	1.00012
13	3.37539e-01	3.37542e-01	1.00001	38	1.12014e+00	1.12024e+00	1.00009
14	3.94784e-01	3.94785e-01	1.00000	39	1.20533e+00	1.20539e+00	1.00005
15	3.94784e-01	3.94785e-01	1.00000	40	1.20533e+00	1.20539e+00	1.00005
16	3.94784e-01	3.94785e-01	1.00000	41	1.27576e+00	1.27582e+00	1.00005
17	4.53842e-01	4.53852e-01	1.00002	42	1.31305e+00	1.31319e+00	1.00011
18	5.15232e-01	5.15239e-01	1.00001	43	1.31305e+00	1.31319e+00	1.00011
19	5.19050e-01	5.19058e-01	1.00001	44	1.39424e+00	1.39434e+00	1.00007
20	5.19050e-01	5.19058e-01	1.00001	45	1.41492e+00	1.41496e+00	1.00003
21	6.24447e-01	6.24453e-01	1.00001	46	1.53663e+00	1.53682e+00	1.00012
22	6.31532e-01	6.31550e-01	1.00003	47	1.57522e+00	1.57560e+00	1.00024
23	6.31532e-01	6.31550e-01	1.00003	48	1.57914e+00	1.57917e+00	1.00002
24	7.23345e-01	7.23373e-01	1.00004	49	1.57914e+00	1.57917e+00	1.00002
25	7.72982e-01	7.73024e-01	1.00005	50	1.57914e+00	1.57917e+00	1.00002

Table 5: List of the smallest 50 non-zero eigenvalues corresponding to bending modes from full Gauss quadrature and GREVI-K, $p = 3$ and 50×50 maximally smooth elements.

l	GAUSS	GREVI-K	ratio	l	GAUSS	GREVI-K	ratio
1	2.08630e-05	2.08630e-05	1.00000	26	5.28783e-03	5.28785e-03	1.00000
2	4.17137e-05	4.17137e-05	1.00000	27	5.28783e-03	5.28785e-03	1.00000
3	4.17137e-05	4.17137e-05	1.00000	28	7.39174e-03	7.39178e-03	1.00001
4	1.24771e-04	1.24771e-04	1.00000	29	7.42810e-03	7.42814e-03	1.00000
5	1.24771e-04	1.24771e-04	1.00000	30	7.42810e-03	7.42814e-03	1.00000
6	3.16962e-04	3.16962e-04	1.00000	31	7.93716e-03	7.93720e-03	1.00001
7	3.16962e-04	3.16962e-04	1.00000	32	7.99509e-03	7.99514e-03	1.00001
8	4.13337e-04	4.13337e-04	1.00000	33	8.09602e-03	8.09606e-03	1.00001
9	4.96973e-04	4.96973e-04	1.00000	34	8.09602e-03	8.09606e-03	1.00001
10	5.01329e-04	5.01329e-04	1.00000	35	1.01617e-02	1.01618e-02	1.00001
11	1.08714e-03	1.08714e-03	1.00000	36	1.01791e-02	1.01792e-02	1.00001
12	1.08714e-03	1.08714e-03	1.00000	37	1.21776e-02	1.21777e-02	1.00001
13	1.21814e-03	1.21814e-03	1.00000	38	1.21776e-02	1.21777e-02	1.00001
14	1.21814e-03	1.21814e-03	1.00000	39	1.38504e-02	1.38506e-02	1.00001
15	1.53034e-03	1.53034e-03	1.00000	40	1.38504e-02	1.38506e-02	1.00001
16	1.53034e-03	1.53034e-03	1.00000	41	1.44907e-02	1.44908e-02	1.00001
17	2.25235e-03	2.25235e-03	1.00000	42	1.44907e-02	1.44908e-02	1.00001
18	2.50753e-03	2.50754e-03	1.00000	43	1.53842e-02	1.53844e-02	1.00001
19	2.53129e-03	2.53130e-03	1.00000	44	1.53853e-02	1.53855e-02	1.00001
20	3.32868e-03	3.32869e-03	1.00000	45	1.81432e-02	1.81434e-02	1.00001
21	3.32868e-03	3.32869e-03	1.00000	46	1.81432e-02	1.81434e-02	1.00001
22	3.80163e-03	3.80164e-03	1.00000	47	1.84647e-02	1.84649e-02	1.00001
23	3.80374e-03	3.80374e-03	1.00000	48	1.94223e-02	1.94226e-02	1.00001
24	4.35665e-03	4.35666e-03	1.00000	49	1.95280e-02	1.95283e-02	1.00001
25	4.35665e-03	4.35666e-03	1.00000	50	2.29547e-02	2.29550e-02	1.00002

Table 6: List of the smallest 50 non-zero eigenvalues corresponding to bending modes from full Gauss quadrature and GREVI-K, $p = 4$ and 50×50 maximally smooth elements.

l	GAUSS	GREVI-K	ratio	l	GAUSS	GREVI-K	ratio
1	2.08630e-05	2.08630e-05	1.00000	26	5.28779e-03	5.28779e-03	1.00000
2	4.17137e-05	4.17137e-05	1.00000	27	5.28779e-03	5.28779e-03	1.00000
3	4.17137e-05	4.17137e-05	1.00000	28	7.39169e-03	7.39169e-03	1.00000
4	1.24771e-04	1.24771e-04	1.00000	29	7.42795e-03	7.42795e-03	1.00000
5	1.24771e-04	1.24771e-04	1.00000	30	7.42795e-03	7.42795e-03	1.00000
6	3.16961e-04	3.16961e-04	1.00000	31	7.93708e-03	7.93709e-03	1.00000
7	3.16961e-04	3.16961e-04	1.00000	32	7.99501e-03	7.99501e-03	1.00000
8	4.13337e-04	4.13337e-04	1.00000	33	8.09585e-03	8.09586e-03	1.00000
9	4.96973e-04	4.96973e-04	1.00000	34	8.09585e-03	8.09586e-03	1.00000
10	5.01329e-04	5.01329e-04	1.00000	35	1.01615e-02	1.01616e-02	1.00000
11	1.08714e-03	1.08714e-03	1.00000	36	1.01789e-02	1.01789e-02	1.00000
12	1.08714e-03	1.08714e-03	1.00000	37	1.21775e-02	1.21775e-02	1.00000
13	1.21814e-03	1.21814e-03	1.00000	38	1.21775e-02	1.21775e-02	1.00000
14	1.21814e-03	1.21814e-03	1.00000	39	1.38502e-02	1.38502e-02	1.00000
15	1.53033e-03	1.53033e-03	1.00000	40	1.38502e-02	1.38502e-02	1.00000
16	1.53033e-03	1.53033e-03	1.00000	41	1.44901e-02	1.44901e-02	1.00000
17	2.25235e-03	2.25235e-03	1.00000	42	1.44901e-02	1.44901e-02	1.00000
18	2.50753e-03	2.50753e-03	1.00000	43	1.53836e-02	1.53836e-02	1.00000
19	2.53128e-03	2.53128e-03	1.00000	44	1.53847e-02	1.53847e-02	1.00000
20	3.32865e-03	3.32865e-03	1.00000	45	1.81425e-02	1.81425e-02	1.00000
21	3.32865e-03	3.32865e-03	1.00000	46	1.81425e-02	1.81425e-02	1.00000
22	3.80160e-03	3.80160e-03	1.00000	47	1.84644e-02	1.84644e-02	1.00000
23	3.80370e-03	3.80370e-03	1.00000	48	1.94219e-02	1.94219e-02	1.00000
24	4.35663e-03	4.35663e-03	1.00000	49	1.95276e-02	1.95276e-02	1.00000
25	4.35663e-03	4.35663e-03	1.00000	50	2.29539e-02	2.29539e-02	1.00000

5 Numerical examples

We now evaluate the performance of the proposed Greville quadrature rules on several geometrically linear and nonlinear problems. Two shell formulations are used:

- KL: *Kirchhoff-Love* shell [9];
- RMC: *Reissner-Mindlin* shell with a *continuous* approach to calculate the director [17, 30, 62].

Three different quadrature rules are compared:

- GAUSS: full *Gauss* quadrature for both KL and RMC shells, defined as $(p+1) \times (p+1)$ Gauss points;
- GREVI-K: *Greville* quadrature rule for KL shells, constructed from Bspline basis $\mathcal{S}_2^p$ in (55).
- GREVI-R: *Greville* quadrature rule for RMC shells, constructed from Bspline basis $\mathcal{S}_1^p$ in (55).

We note that two-point GAUSS quadrature is used along the thickness direction in this work.

For geometrically linear problems, the quality of the stress or resultant force is explored. Two types of resultant forces are calculated as follows:

- Bending moments:

$$m_{\alpha\beta} = \int_{-\frac{h}{2}}^{\frac{h}{2}} \xi^3 \sigma_{\alpha\beta} \, \mathrm{d}\xi^3, \tag{60}$$

where $\sigma_{\alpha\beta}$ are the components of the in-plane stress, $\boldsymbol{\sigma}$, defined in the local Cartesian coordinate system as

$$\boldsymbol{\sigma} = \mathbf{C}_{\mathrm{p}} \bar{\mathbf{T}} \bar{\mathbf{B}} \mathbf{U}, \tag{61}$$

where $\mathbf{C}_{\mathrm{p}}$ is the elasticity matrix given in (37) and $\mathbf{U}$ is the solution vector. For RMC shells, $\bar{\mathbf{T}}$ is the in-plane strain transformation matrix which consists of the first three rows of $\mathbf{T}$ in (69), and $\bar{\mathbf{B}}$ is composed of the first three rows of the strain-displacement matrix whose nodal submatrix $\mathbf{B}_I$ is given in (107). For KL shells, $\bar{\mathbf{T}} = \mathbf{T}^{\mathrm{KL}}$, which is given in (70), and $\bar{\mathbf{B}}$ consists of the nodal submatrix $\mathbf{B}_I$ given in (137).

- Membrane forces:

$$n_{\alpha\beta} = \int_{-\frac{h}{2}}^{\frac{h}{2}} \sigma_{\alpha\beta} \, \mathrm{d}\xi^3. \tag{62}$$

Stress or resultant force oscillation is commonly seen in standard FEA and IGA. Post-processing procedures are usually required to achieve smooth stress results. We will demonstrate that the dramatic stress or resultant force oscillation, shown in lower-order elements with the proposed quadrature schemes, can be also removed through a commonly used technique, i.e., the L_2 projection.

Take the membrane forces $n_{\alpha\beta}$ as examples. Assuming $\left\{N_I^p\right\}_{I=1}^{n}$ is a B-spline basis used for IGA and $\left\{N_I^{p-1}\right\}_{I=1}^{\tilde{n}}$ is the corresponding one-order-lower B-spline basis whose continuity is one-order-lower as well , then the smoothed membrane forces $\bar{n}_{\alpha\beta}$ are represented as

$$\bar{n}_{\alpha\beta} = \sum_{i=1}^{\tilde{n}} N_I^{p-1} \bar{n}_{\alpha\beta I}, \tag{63}$$

where the unknown coefficients $\bar{n}_{\alpha\beta I}$ are solved through the standard L_2 projection of the membrane forces $n_{\alpha\beta}$ onto $\{N_I^{p-1}\}_{I=1}^{\tilde{n}}$, i.e.,

$$\int_{\hat{A}} \bar{n}_{\alpha\beta} N_I^{p-1} \mathrm{d}\hat{A} = \int_{\hat{A}} n_{\alpha\beta} N_I^{p-1} \mathrm{d}\hat{A}\,, \tag{64}$$

where $\hat{A}$ is the parametric domain of the midsurface. Note that if a quadrature rule is used for analysis, the same rule is also adopted for projection (64). Therefore, compared to the full GAUSS quadrature, the proposed quadrature rules also help to save computational cost in the post-processing as they use many fewer quadrature points. We also note that instead of the global projection (64), the local projection technique [67] and its more compact varients [68, 69] based on dual bases are also possible options for smoothing stress.

5.1 Cylindrical shell subject to transverse loading in the radial direction

Figure 10 shows a schematic for a cylindrical shell subject to transverse loading in the radial direction. Although ostensibly a very simple problem, it is very challenging numerically and reveals several potential shortcomings of elements. This model has radius $R = 10$, width $b = 1$, and thickness t. Young's modulus and Poisson's ratio are $E = 1000$ and $\nu = 0$, respectively. The cylindrical shell is clamped at one end and subject to a traction, $q_x = -0.1t^3$, at the other end. The analytical membrane force and bending moment, based on static equilibrium, are $n_{11}^{\text{exact}} = q_x \cos\theta$ and $m_{22}^{\text{exact}} = -q_x R \cos\theta$, respectively, where, as illustrated in Figure 10, θ is the central angle and the subscripts "11" and "22" indicate the local coordinate components, i.e., those along the circumferential direction and parallel to the y-axis.

To assess the accuracy of the proposed GREVI-K quadrature, we first explore the convergence rates for the membrane force in terms of the relative error in the L^2-norm. Figure 11 shows that GREVI-K achieves optimal rates for all investigated degrees $p = 3$ to 6 and slenderness ratios $\frac{R}{t} = 100, 1000$, and 10000, except that the convergence rate deteriorates for $p = 6$ and $\frac{R}{t} = 100$. Note that for coarse meshes, the GREVI-K quadrature seems to obtain slightly worse results than GAUSS. This is because here all error norms are calculated with GAUSS quadrature, which is biased toward GAUSS as stress or resultant force is usually more accurate at quadrature points that are used for analysis. As the meshes are refined, this difference disappears and these two quadrature rules achieve comparable results. Figure 12 shows the membrane force convergence rates for the same cases used in Figure 11, but the error norms are calculated with the corresponding quadrature rules used for analysis. As it shows, GREVI-K and GAUSS now achieve comparable results even with coarse meshes. However, we note that for $p = 4$, GREVI-K obtains very small error norms at some points. This is because, for $p = 4$, the GREVI-K quadrature has negative weights. When calculating the L_2-norm via numerical integration, the product of the weight and the square of the absolute error at some quadrature point can be either positive or negative depending on the value of the weight, and positive and negative products at different quadrature points happen to be canceled with each other when calculating the summation in the numerical integration.

Figure 13 shows the convergence rates of the bending moment for GREVI-K and GAUSS. As can be seen, for $p = 2$, slenderness $\frac{R}{t} = 100$ and 1000, optimal rates are achieved, and for slenderness $\frac{R}{t} = 10000$, even superconvergence rate is obtained. For many other cases, the convergence rates are lost. One reason for these unexpected convergence rates is the pathology of membrane locking. In addition, the kinematic assumption given in Section 3.1, i.e., ignoring the second-order terms of ξ^3, also interferes with the convergence rates and eventually levels off the error. We note that this assumption is widely used as it simplifies the shell formulations and improves the computational efficiency, and, from the engineering point of view, the error is small enough, especially for thin shells. Interested readers are referred to [60] for more details about this assumption. Even though we see reduced convergence rates for bending moment, it is consistent that GREVI-K and GAUSS obtain similar results for all cases, and higher-order bases achieve better results than lower-order bases.

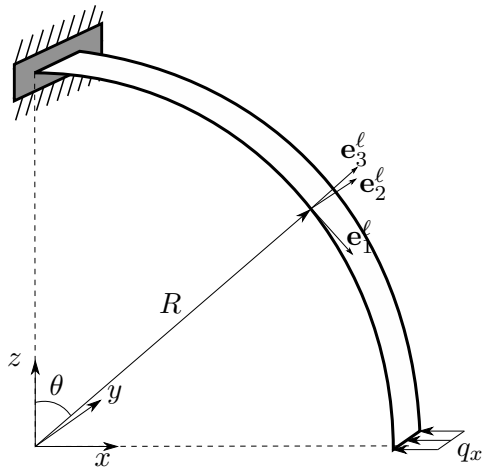

Figure 10: Cylindrical shell subject to transverse loading in the radial direction.

To examine the quality of the resultant force, the membrane force n_{11}, normalized by the maximum value of the exact solution n_{11}^{exact}, for $R/t = 100$, $p = 3$, and various numbers of KL shell elements, is illustrated in Figure 14. As can be seen in Figures 14a and b, GAUSS and GREVI-K quadratures obtain almost identical results, which oscillates significantly even with 64 elements. Figure 15 verifies that the L_2 projection given in (64) can be applied to removing the membrane force oscillation effectively for both GAUSS and GREVI-K quadrature rules.

In the IGA framework, in addition to the usual post-processing techniques, a simple way to alleviate the oscillation is elevating the basis order. Figure 16 shows that quintic basis functions with 16 elements result in smooth membrane force for both GAUSS and GREVI-K rules. In fact, the results are smooth as well for all $p = 6$. Again, GREVI-K achieves similar results as GAUSS for all bases up to $p = 6$ but with many fewer quadrature points.

For this problem, the bending moment does not show significant oscillations for any p, even the lowest order considered, $p = 3$. Figure 17 shows that even with only 16 cubic KL shell elements both GAUSS and GREVI-K achieve a high quality of the bending moment.

We next explore the behavior of the GREVI-R rule with the RMC shell. Figure 18 shows the convergence rates for the RMC shell with GAUSS and GREVI-R rules. For $p = 2$, both GAUSS and GREVI-R achieve optimal rates with slenderness $\frac{R}{t} = 100$, but as the slenderness increases, the RMC shell exhibits increased locking and the convergence is lost completely for $\frac{R}{t} = 10000$. For $p = 3$ to 5, the GREVI-R rule behaves similarly to the GAUSS rule for all slendernesses and obtains optimal rates. These results clearly show that higher-order bases play a crucial rule in alleviating locking. Compared to the GAUSS rules, the convergence rates for GREVI-R are slightly reduced for $p = 6$ as the error norms get very small. However, from the practical point of view, these slightly reduced convergence rates are negligible as the accuracy is already adequate for engineering applications. Note that here the error norms are calculated with the corresponding quadrature rules used for analysis because GREVI-R has positive weights for all cases with uniform knot vectors. Additionally, the convergence plots for the bending moment are omitted since similar behavior, as shown in Figure 13 for KL shells, is observed for RMC shells here.

Figure 19 illustrates that, for quadratic RMC elements and slenderness $R/t = 100$, the GAUSS and GREVI-R quadrature rules obtain similar membrane force results which oscillate significantly even with 128 elements. The L_2 projection (64) improves the membrane force quality and obtains accurate results with 64 elements as shown in Figures 20a and b. Note that the membrane force quality for RMC shells in Figures 19 and 20 is worse than that for KL shells shown in Figures 14

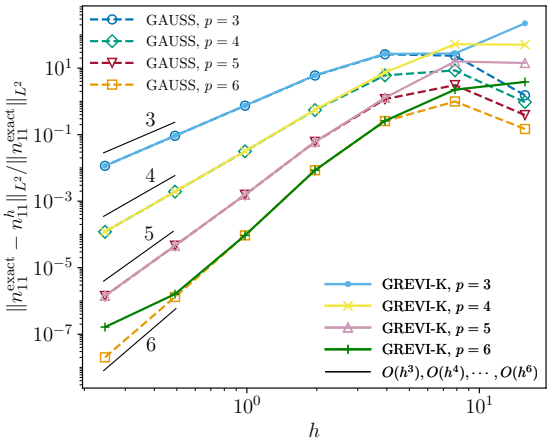

(a) $\frac{R}{t} = 100$.

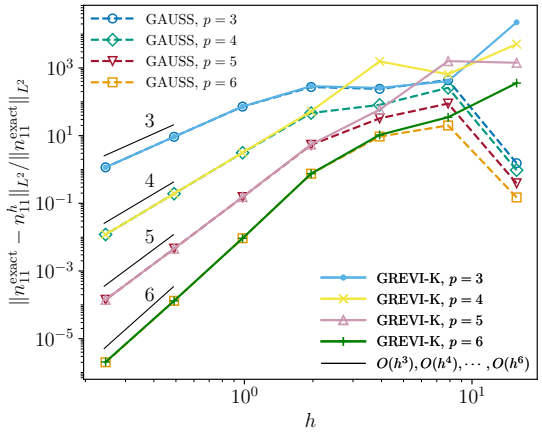

(b) $\frac{R}{t} = 1000$.

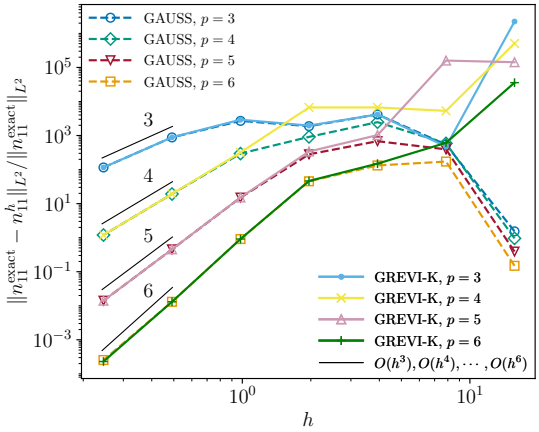

(c) $\frac{R}{t} = 10000$.

Figure 11: Cylindrical KL shell: Membrane force convergence rates for GAUSS and GREVI-K, increasing slenderness $\frac{R}{t} = 100, 1000, 10000$, degrees $p = 3$ to 6, and maximally smooth elements. The error norms are calculated with GAUSS quadrature. The initial mesh consists of 1×1 elements and uniform refinement is then used in the circumferential direction.

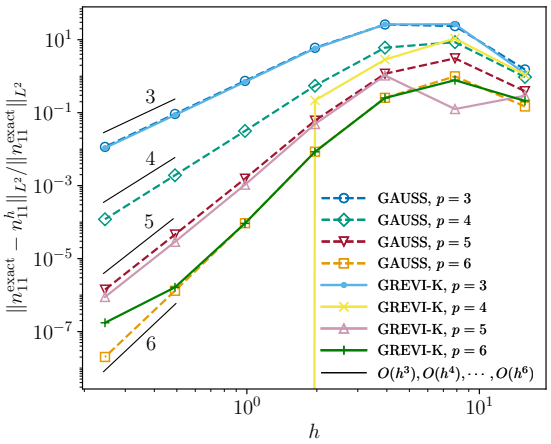

(a) $\frac{R}{t} = 100$, sampled at GAUSS.

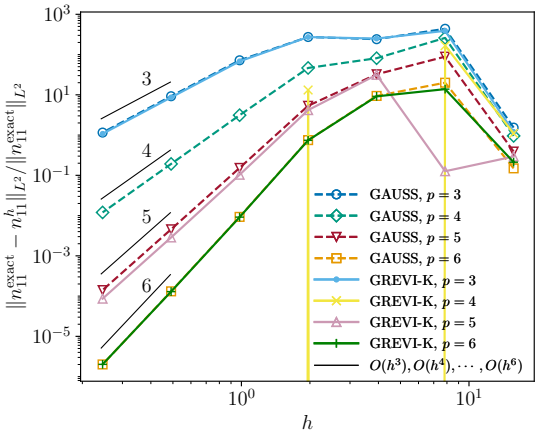

(b) $\frac{R}{t} = 1000$, sampled at GAUSS.

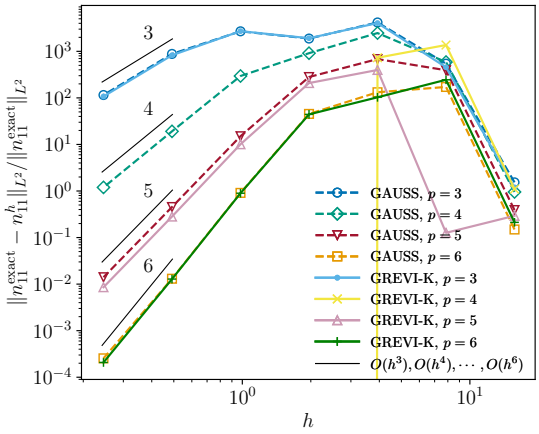

(c) $\frac{R}{t} = 10000$, sampled at GAUSS.

Figure 12: Cylindrical KL shell: Membrane force convergence rates for GAUSS and GREVI-K, increasing slenderness $\frac{R}{t} = 100, 1000, 10000$, degrees $p = 3$ to 6, and maximally smooth elements. The error norms are calculated with the corresponding quadrature rules used for analysis. The initial mesh consists of 1×1 elements and uniform refinement is then used in the circumferential direction.

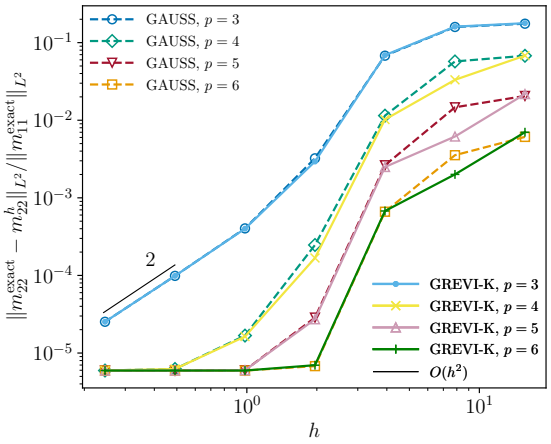

(a) $\frac{R}{t} = 100$.

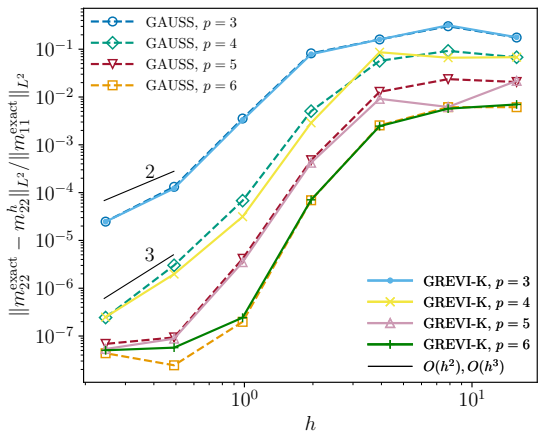

(b) $\frac{R}{t} = 1000$.

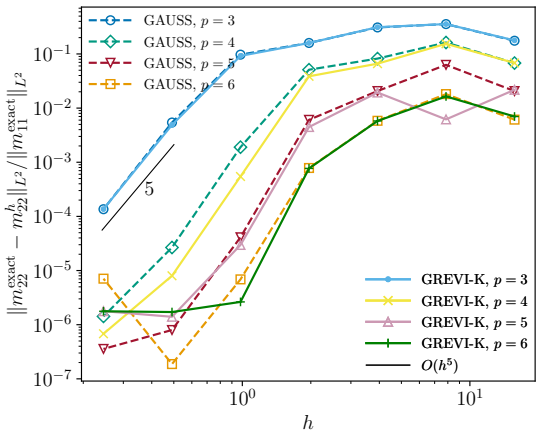

(c) $\frac{R}{t} = 10000$.

Figure 13: Cylindrical KL shell: Bending moment convergence rates for GAUSS and GREVI-K, increasing slenderness $\frac{R}{t} = 100, 1000, 10000$, degrees $p = 3$ to 6, and maximally smooth elements. The error norms are calculated with GAUSS quadrature. The initial mesh consists of 1×1 elements and uniform refinement is then used in the circumferential direction.

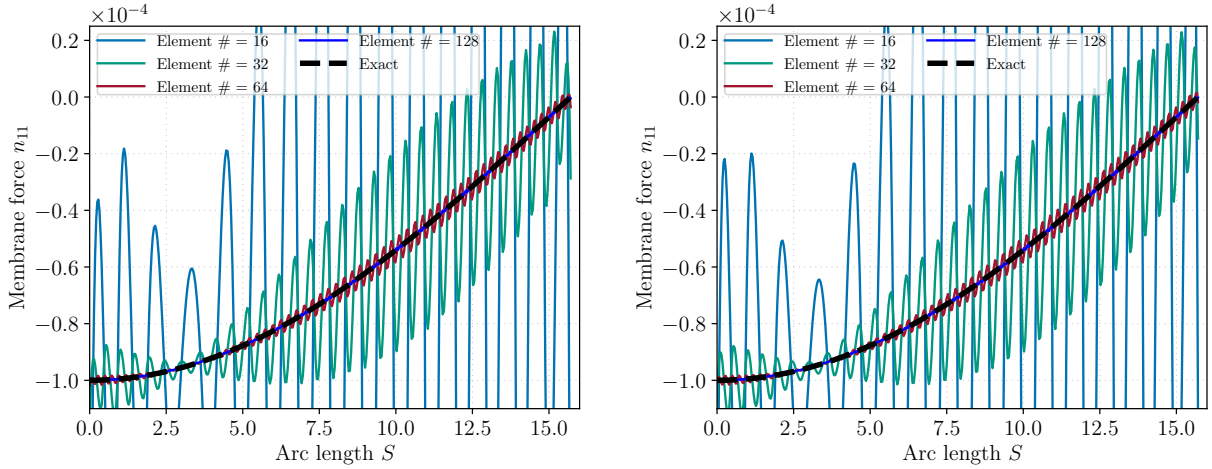

(a) GAUSS. (b) GREVI-K.

Figure 14: Cylindrical KL shell: Normalized membrane force n_{11} for GAUSS and GREVI-K, $R/t = 100$, $p = 3$, and various numbers of elements.

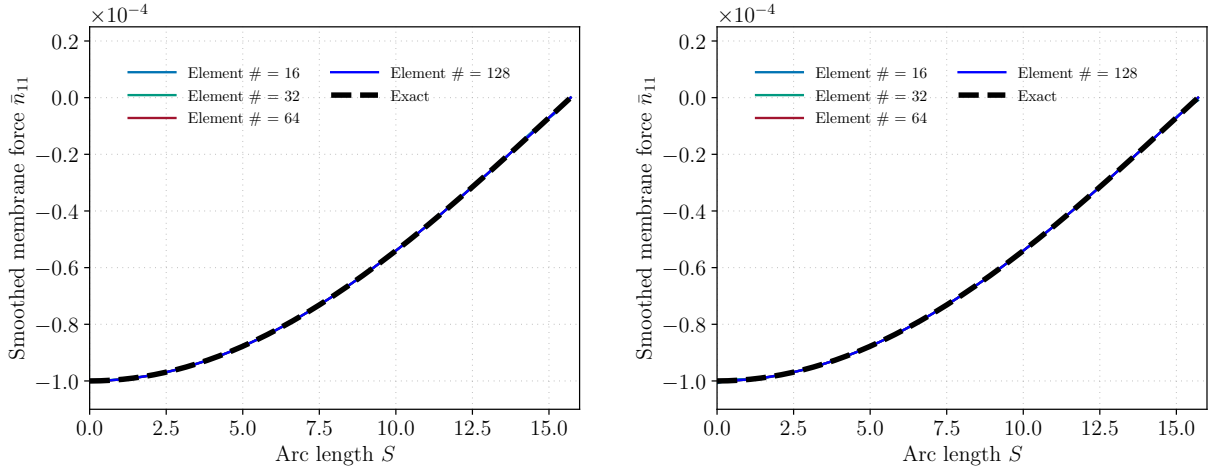

(a) GAUSS. (b) GREVI-K.

Figure 15: Cylindrical KL shell: Normalized membrane force $\bar{n}_{11}$, smoothed by the L_2 projection (64), for GAUSS and GREVI-K, $R/t = 100$, $p = 3$, and various numbers of elements.

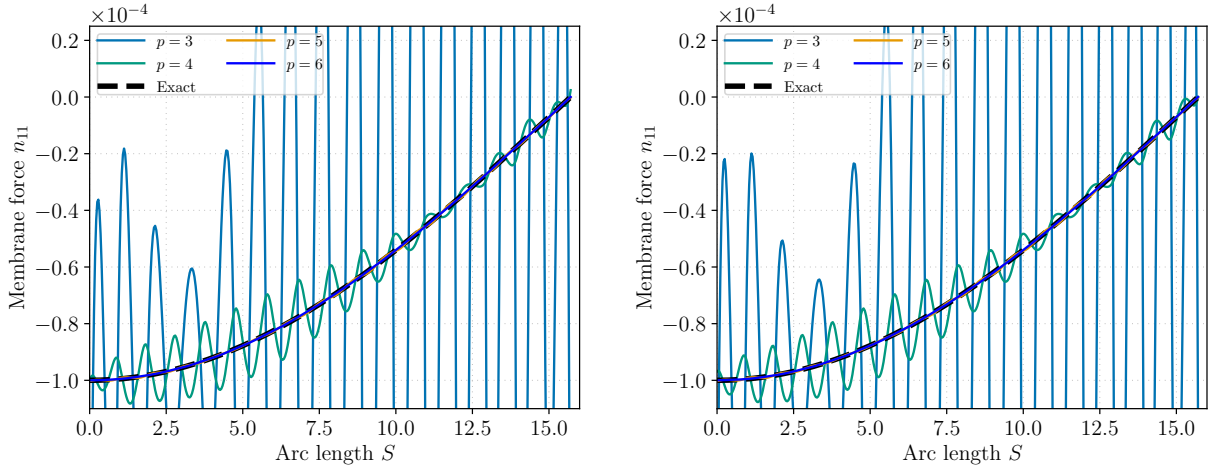

(a) GAUSS. (b) GREVI-K.

Figure 16: Cylindrical KL shell: Normalized membrane force n_{11} for GAUSS and GREVI-K, $R/t = 100$, $p = 3$ to 6, and 16 elements. Note that for $p \geq 5$, the results are free of oscillations.

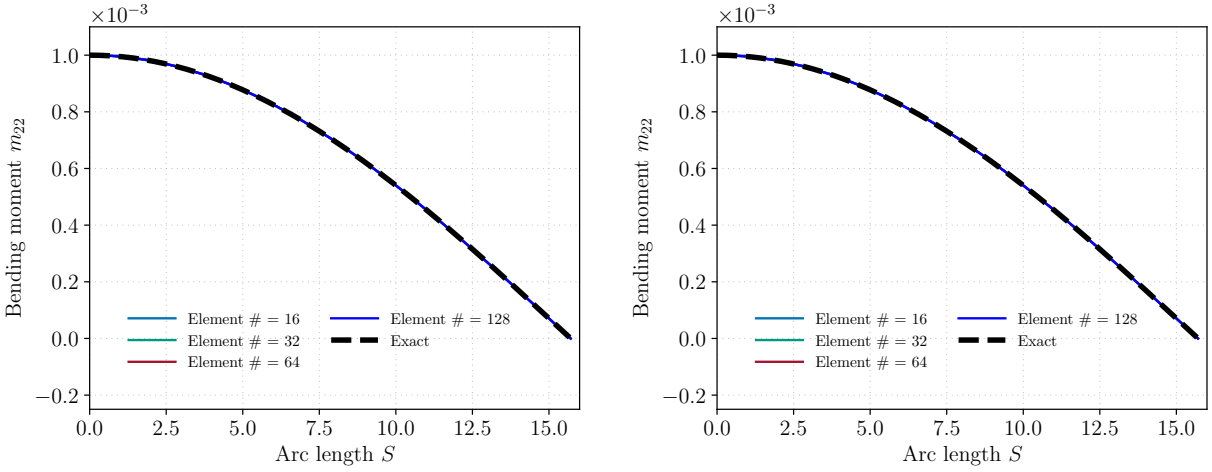

(a) GAUSS. (b) GREVI-K.

Figure 17: Cylindrical KL shell: Normalized bending moment m_{22} for GAUSS and GREVI-K, $R/t = 100$, $p = 3$, and various numbers of elements.

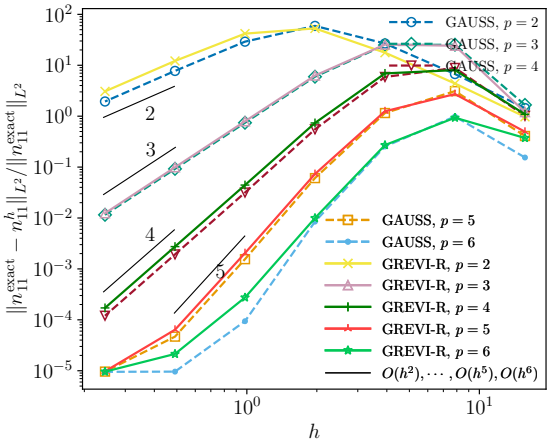

(a) $\frac{R}{t}=100$.

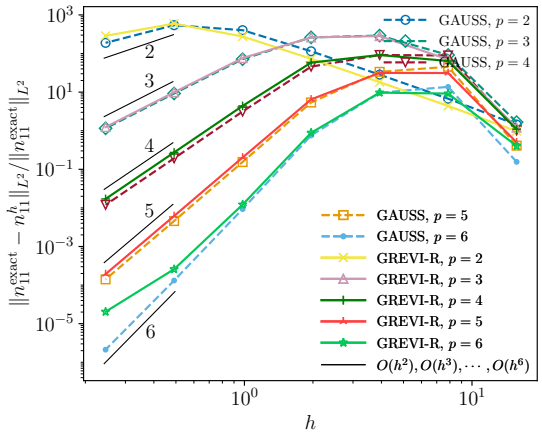

(b) $\frac{R}{t}=1000$.

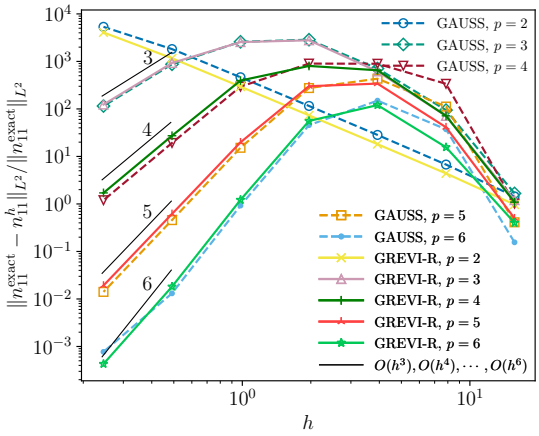

(c) $\frac{R}{t}=10000$.

Figure 18: Cylindrical RMC shell: Membrane force convergence rates for GAUSS and GREVI-R, increasing slenderness $\frac{R}{t}=100,1000,10000$, degrees $p=2$ to 6, and maximally smooth elements. The error norms are calculated with the same quadrature rules used for analysis. The initial mesh consists of 1×1 elements and uniform refinement is then used in the circumferential direction.

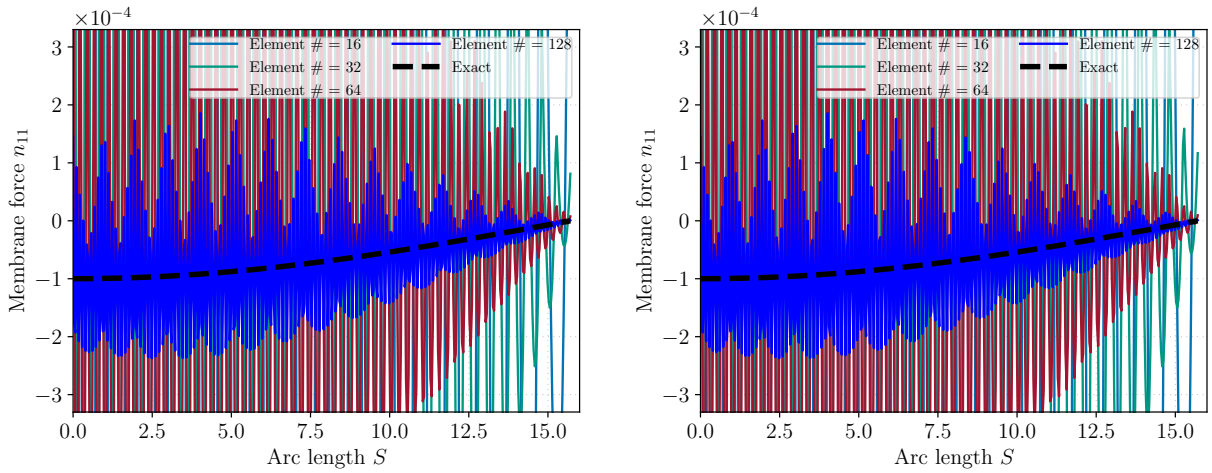

(a) GAUSS.

(b) GREVI-R.

Figure 19: Cylindrical RMC shell: Normalized membrane force n_{11} for GAUSS and GREVI-R, $R/t = 100$, $p = 2$, and various numbers of elements.

and 15, because here only quadratic elements are used rather than cubic elements for KL shells. Again, once we elevate the basis order to $p = 5$ and 6, both GAUSS and GREVI-R obtain smooth membrane force even with only 16 elements as shown in Figure 21.

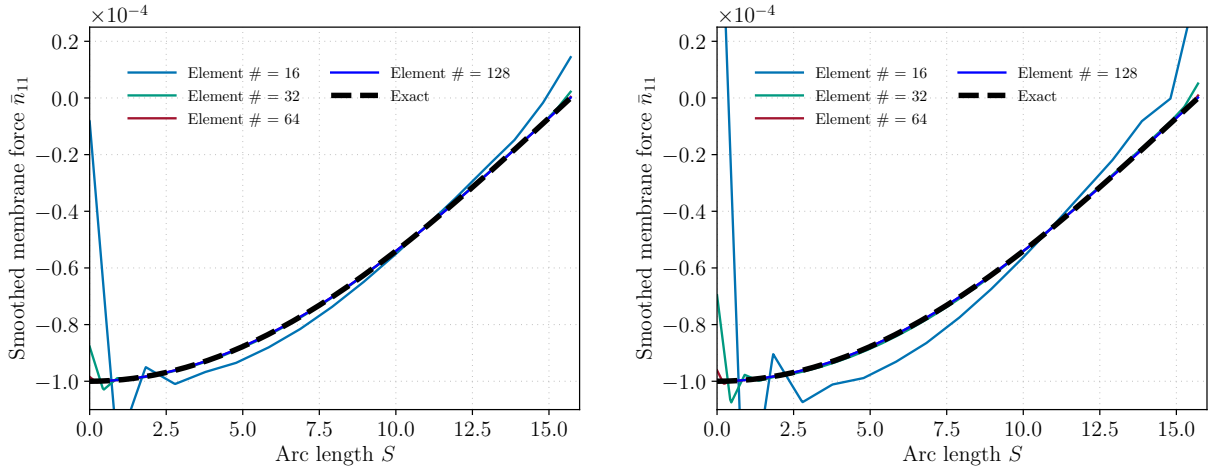

(a) GAUSS. (b) GREVI-R.

Figure 20: Cylindrical RMC shell: Normalized membrane force $\bar{n}_{11}$, smoothed through the L_2 projection (64) of n_{11} in Figure 19, for GAUSS and GREVI-R, $R/t = 100$, $p = 2$, and various numbers of elements.

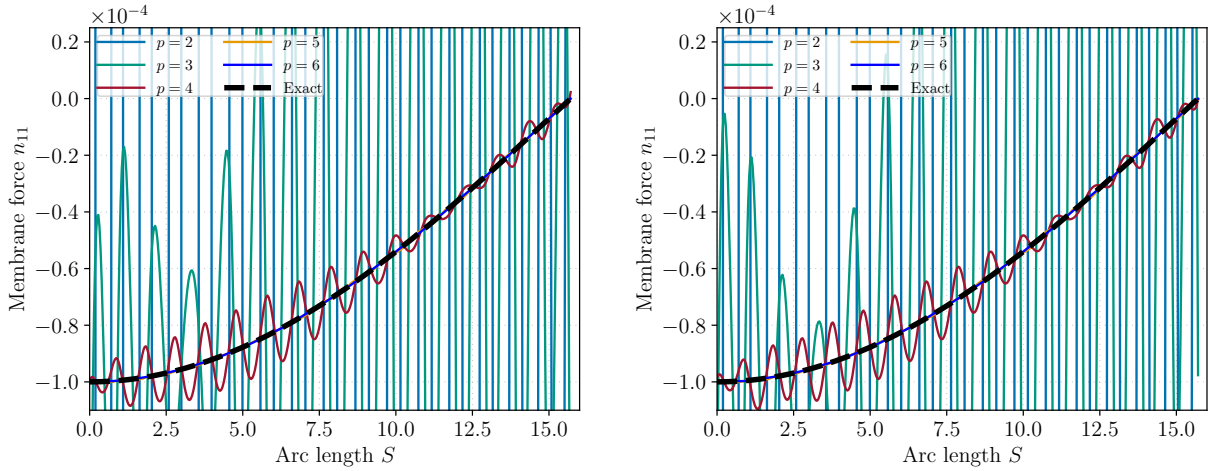

(a) GAUSS. (b) GREVI-R.

Figure 21: A cylindrical RMC shell: Normalized membrane force n_{11} for GAUSS and GREVI-R, $R/t = 100$, $p = 2$ to 6, and 16 elements. Note that for $p = 5$ and 6, the results are free of oscillations.

5.2 Clamped square plate subject to a uniformly distributed load

We now analyze a clamped square plate subject to a uniform distributed load as shown in Figure 22a. The square plate has side length $L = 10$, Young's modulus $E = 1000$, and Poisson's ratio $\nu = 0.3$. The thickness t is varied to give a slenderness ratio $\frac{L}{t}$. The distributed load is set to $q = t^3$. The maximum displacement at the center of the plate is monitored. The exact solution, based on Poisson-Kirchhoff thin plate theory, is $u_{max} = -0.138173$ for all thicknesses [70]. The geometry is initially modeled with one quadratic element as shown in Figure 22b and h- and k-refinements are used afterwards. For a flat plate, the membrane and bending strains are decoupled. Therefore, no membrane locking is present in this problem. Additionally, as KL shells do not suffer from transverse shear locking, for this problem, we only employ the RMC shell to explore the effectiveness of the proposed GREVI-R rule along with higher-order bases in alleviating shear locking.

Figures 23a, c and e give an entire view of the convergence of the maximum displacement u_z at the center of the plate. It shows that, for $p = 2$ and 3, both GAUSS and GREVI-R lock severely and converge at a similar, slow pace, but higher-order bases ($p \geq 4$) alleviate transverse shear locking effectively and achieve good results even with coarse meshes. Figures 23b, d and f give a locally enlarged view of the convergence for higher-order bases and coarse meshes. As can be seen, for $p = 4$ to 6, the GAUSS and GREVI-R rules also behave similarly.

We then explore the accuracy of the GREVI-R rule for skewed meshes. The initial mesh consists of one quadratic element shown in Figure 22c, and h- and k-refinements are used to obtain more refined meshes afterwards. As shown in Figure 24, for both GAUSS and GREVI-R rules, coarse meshes obtain worse results for all cases than those shown in Figure 23, but again GREVI-R achieves comparable accuracy with GAUSS for all degrees, see Figures 24b, d and f for locally enlarged views.

Figure 25 gives the computational time comparison between the GAUSS and GREVI-R rules in computing the stiffness matrix for the clamped square plate problem. Computational efficiency is significantly improved by the GREVI-R rule. Observed speedups are approximately 50% for $p = 2$ and more than 90% for $p = 5$ and 6, as the mesh is refined. Note that the computational time spent on calculating the quadrature points and weights is also included in the time comparison.

We now investigate the shear stress quality for GREVI-R and GAUSS rules. Figure 26 gives a numerical reference solution of the transverse shear stress σ_{xz}, for slenderness $L/t = 100$, at the midsurface, which is obtained with the standard GAUSS quadrature and 32×32 maximally smooth sextic RMC elements. Figure 27 shows that with maximally smooth quadratic elements and various numbers of elements ranging from 8×8 to 32×32, the transverse shear stress σ_{xz} oscillates dramatically for both GAUSS and GREVI-R quadrature rules and the maximum and minimum values are off from the reference values given in Figure 26. Elevating the basis order alleviates the oscillation for both quadrature rules as shown in Figure 28 for 8×8 elements with degrees $p = 3$ to 6. As can be seen in Figures 28c and d, for $p = 4$, the stress oscillation is still obvious for both quadrature rules but the maximum and minimum values obtained by GREVI-R tend to be very close to the reference values which are better than those obtained by GAUSS. As we continue to elevate the basis orders to $p = 5$ and 6, the stress oscillation starts to disappear for both quadrature rules, and in these two cases, GAUSS achieves slightly better stress results than GREVI-R. Again, even though GREVI-R and GAUSS achieve comparable results, GREVI-R is much less expensive than GAUSS as it uses much fewer quadrature points.

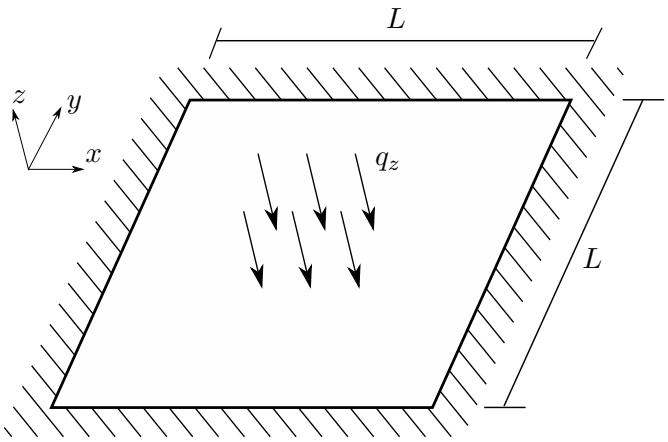

(a) Schematic.

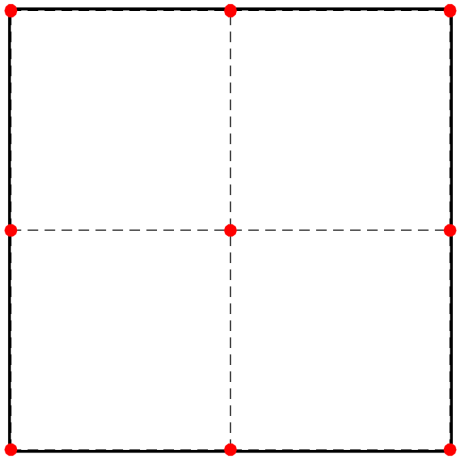

(b) Initial regular mesh.

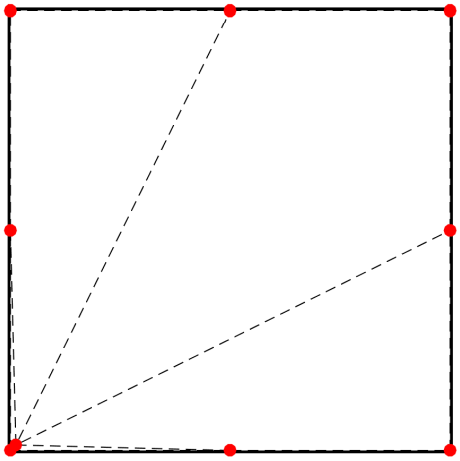

(c) Initial skewed mesh.

Figure 22: Clamped square plate subject to a uniform distributed load. (a) schematic; (b) initial regular mesh and control net; (c) initial skewed mesh and control net. The control nets are depicted by red dots and dashed lines.

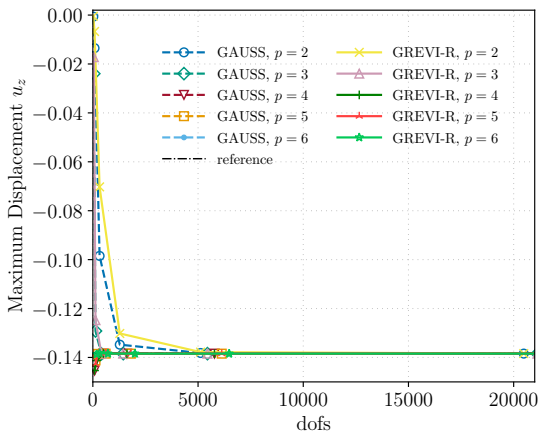

(a) $\frac{L}{t} = 100$, entire view.

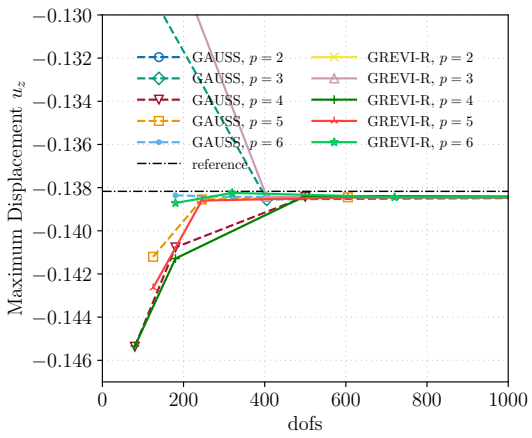

(b) $\frac{L}{t} = 100$, locally enlarged view.

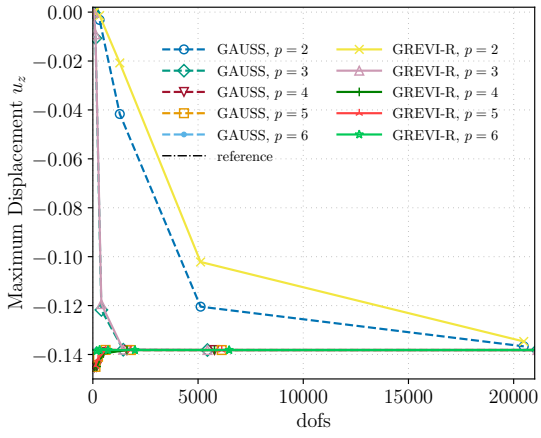

(c) $\frac{L}{t} = 1000$, entire view.

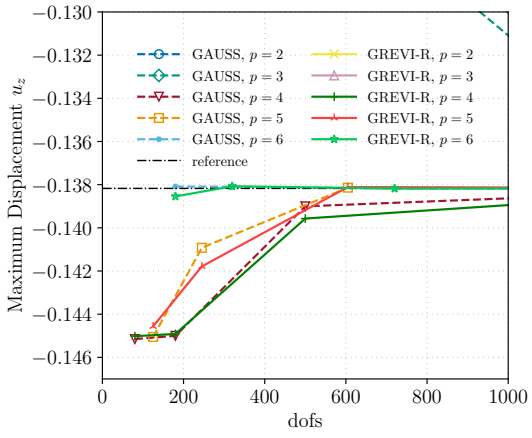

(d) $\frac{L}{t} = 1000$, locally enlarged view.

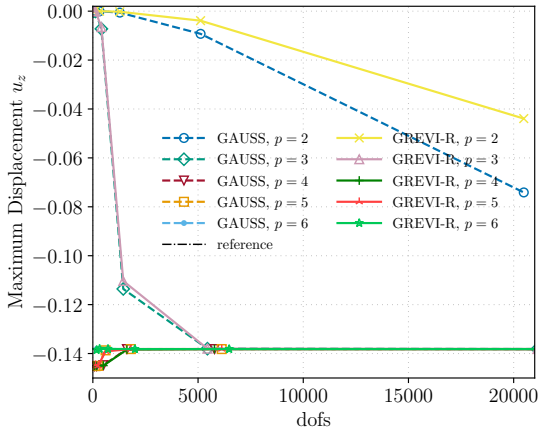

(e) $\frac{L}{t} = 10000$, entire view.

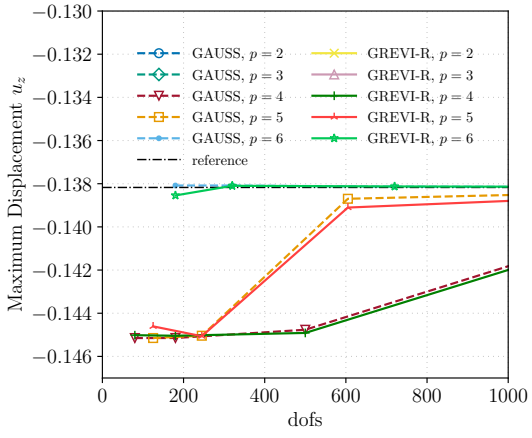

(f) $\frac{L}{t} = 10000$, locally enlarged view.

Figure 23: Clamped square plate under a distributed load modeled as an RMC shell: Maximum deflection u_z with GAUSS and GREVI-R, increasing slendernesses $\frac{L}{t} = 100, 1000, 10000$ and degrees $p = 2$ to 6. The initial mesh consists of a *regular* quadratic element as shown in Figure 22b and h and k-refinements are used afterwards. Left column: entire view of all data points; Right column: locally enlarged view of selected data points.

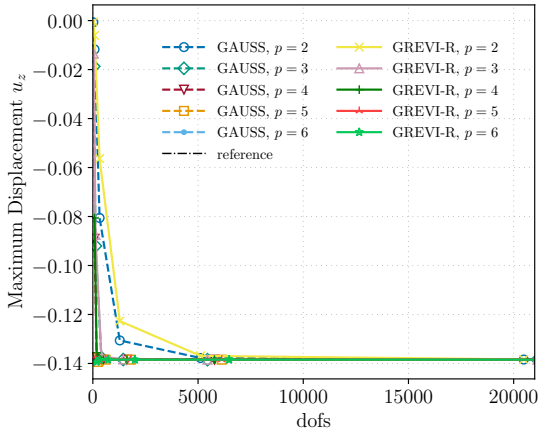

(a) $\frac{L}{t} = 100$, entire view.

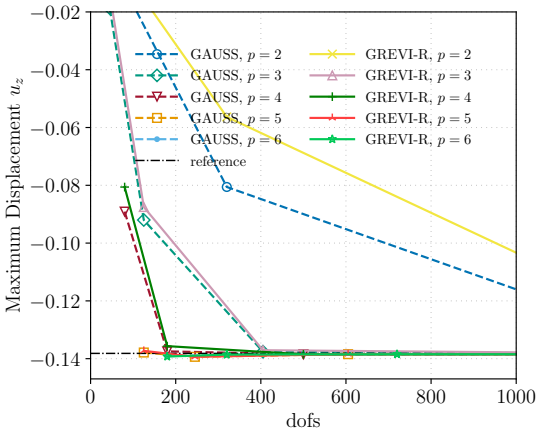

(b) $\frac{L}{t} = 100$, locally enlarged view.

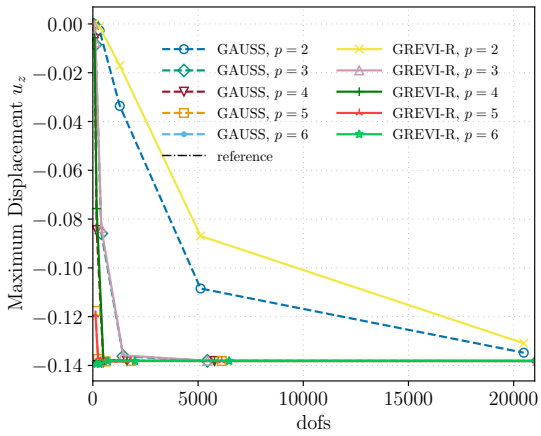

(c) $\frac{L}{t} = 1000$, entire view.

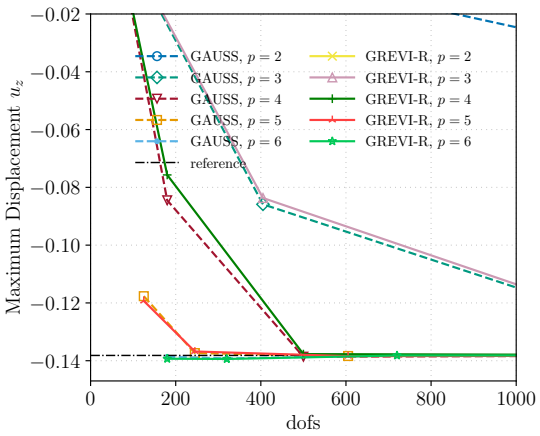

(d) $\frac{L}{t} = 1000$, locally enlarged view.

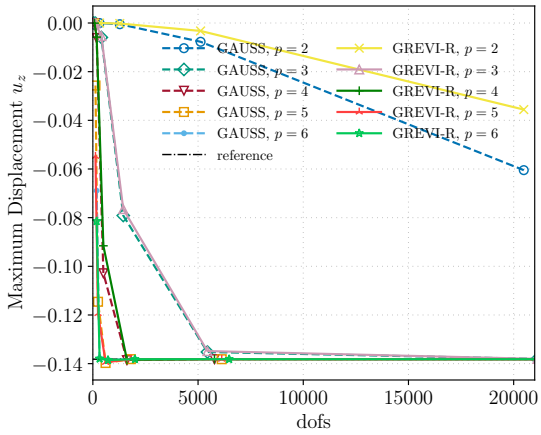

(e) $\frac{L}{t} = 10000$, entire view.

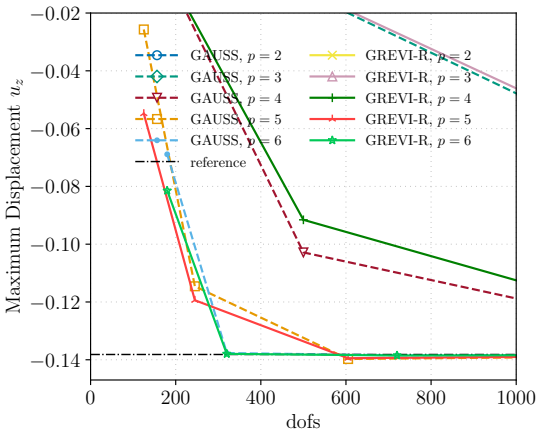

(f) $\frac{L}{t} = 10000$, locally enlarged view.

Figure 24: Clamped square plate under a distributed load modeled with the RMC shell: Maximum deflection u_z with GAUSS and GREVI-R, increasing slendernesses $\frac{L}{t} = 100, 1000, 10000$ and degrees $p = 2$ to 6. The initial mesh consists of a *skewed* quadratic element as shown in Figure 22c and h- and k-refinements are used afterwards. Left column: entire view of all data points; Right column: locally enlarged view of selected data points.

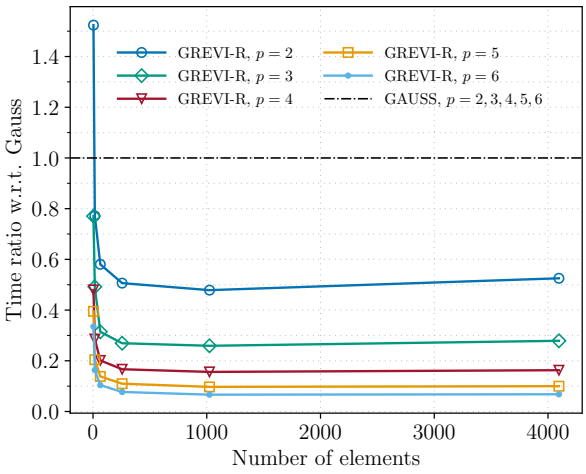

Figure 25: Clamped square plate under a distributed load modeled as an RMC shell: Stiffness matrix compute times for GAUSS and GREVI-R. Note that the time spent on computing the quadrature points and weights are included for GREVI-R.

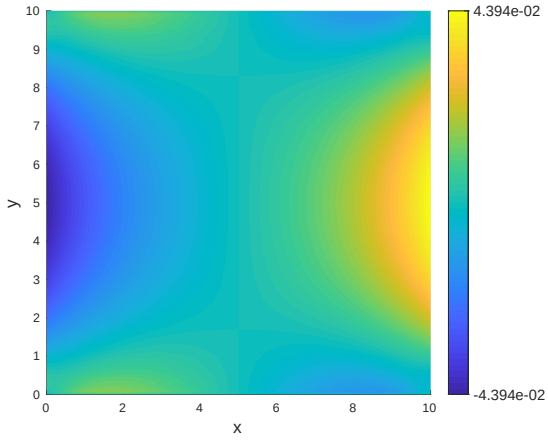

Figure 26: Clamped square plate under a distributed load modeled as an RMC shell: Numerical reference solution of the shear stress σ_{xz} at the middle surface, for slenderness $\frac{L}{t} = 100$, calculated with full GAUSS quadrature and 32×32 maximally smooth sextic elements.

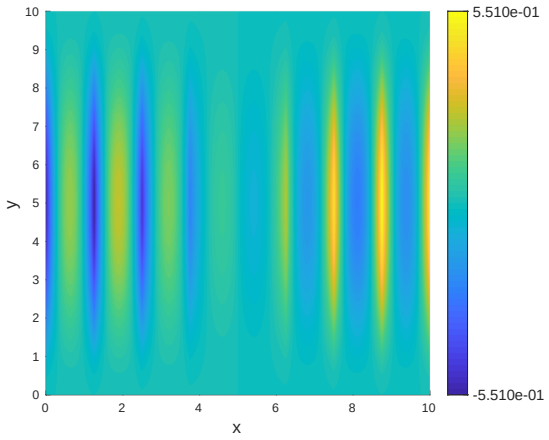

(a) GAUSS, 8×8 elements.

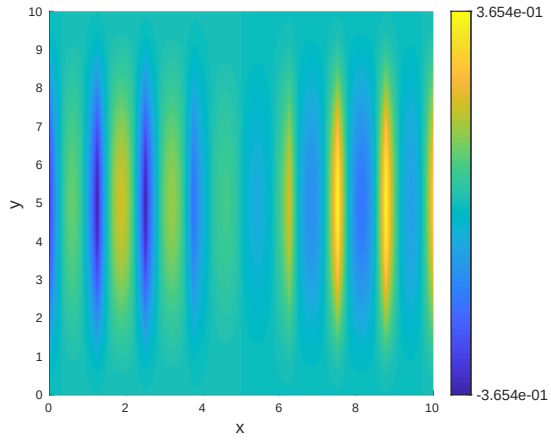

(b) GREVI-R, 8×8 elements.

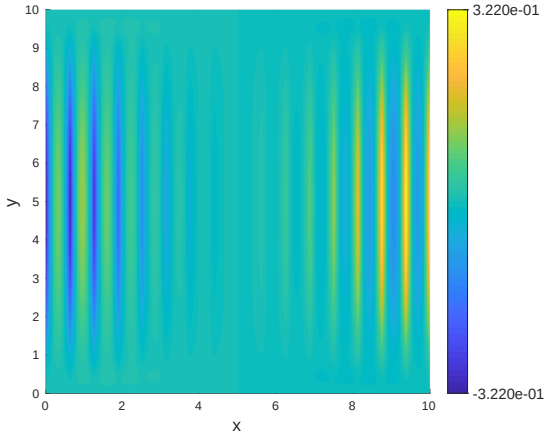

(c) GAUSS, 16×16 elements.

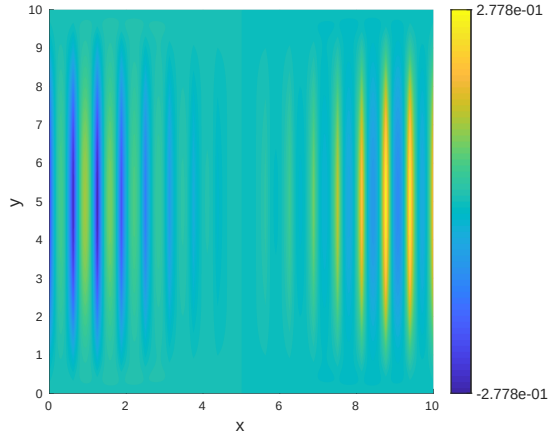

(d) GREVI-R, 16×16 elements.

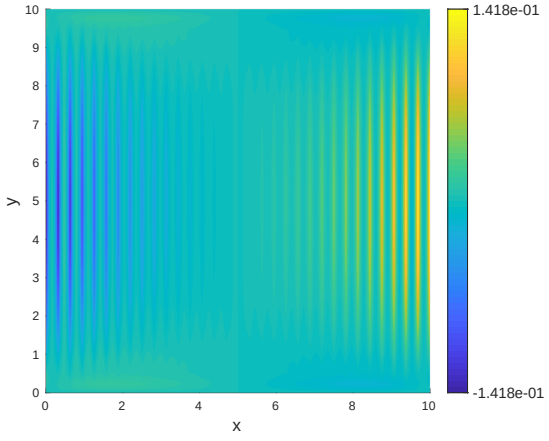

(e) GAUSS, 32×32 elements.

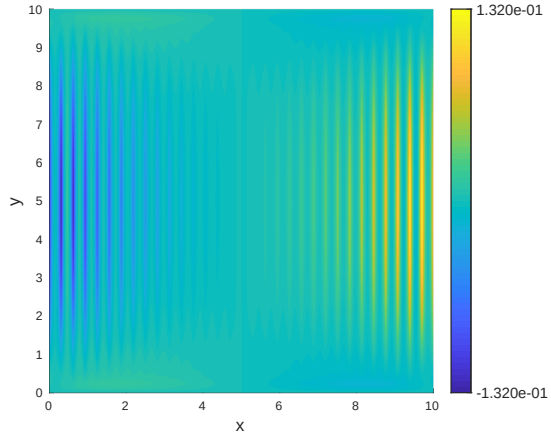

(f) GREVI-R, 32×32 elements.

Figure 27: Clamped square plate under a distributed load modeled as an RMC shell: Transverse shear stress σ_{xz} at the middle surface, for slenderness $\frac{L}{t} = 100$, GAUSS and GREVI-R, and various numbers of maximally smooth quadratic elements.

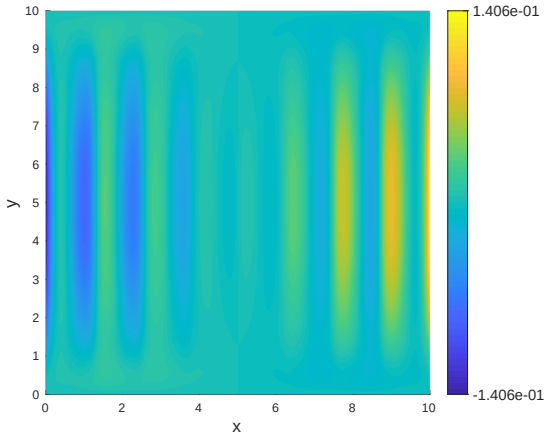

(a) GAUSS, $p = 3$.

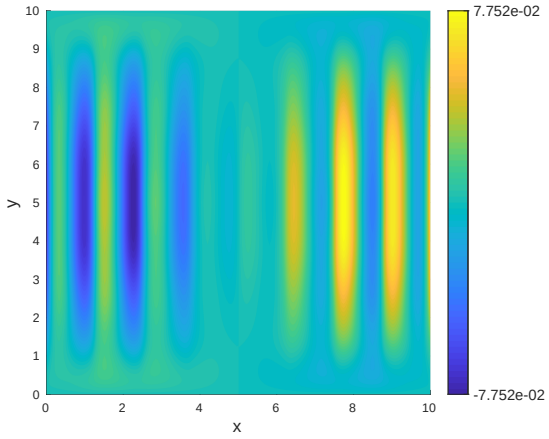

(b) GREVI-R, $p = 3$.

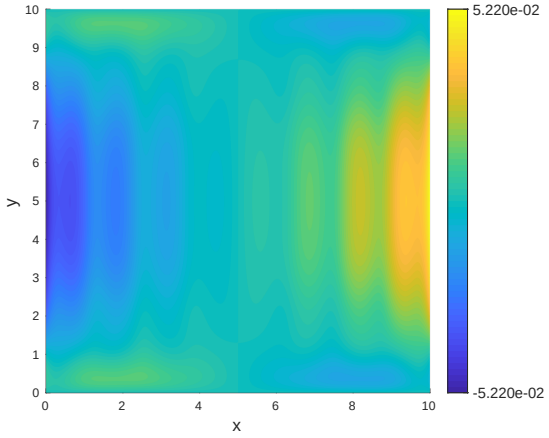

(c) GAUSS, $p = 4$.

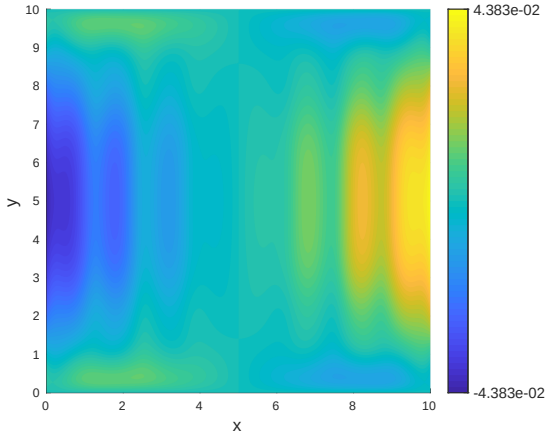

(d) GREVI-R, $p = 4$.

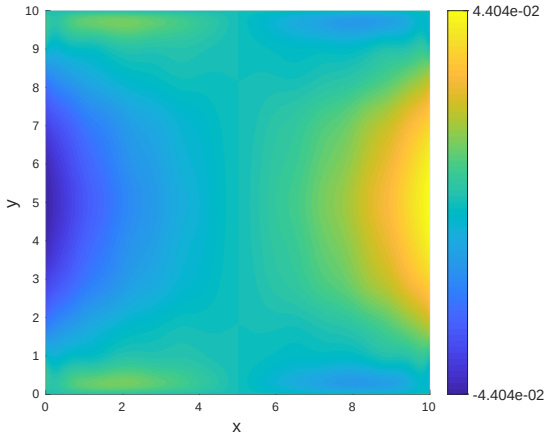

(e) GAUSS, $p = 5$.

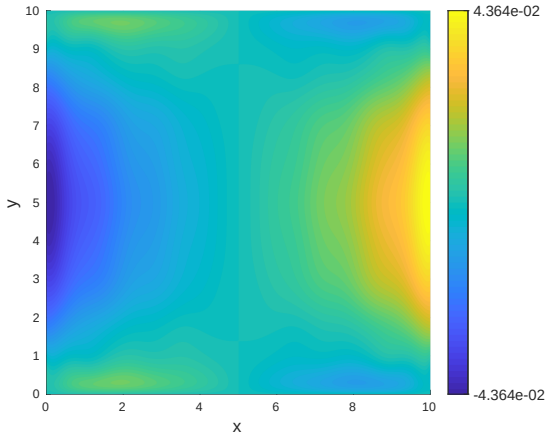

(f) GREVI-R, $p = 5$.

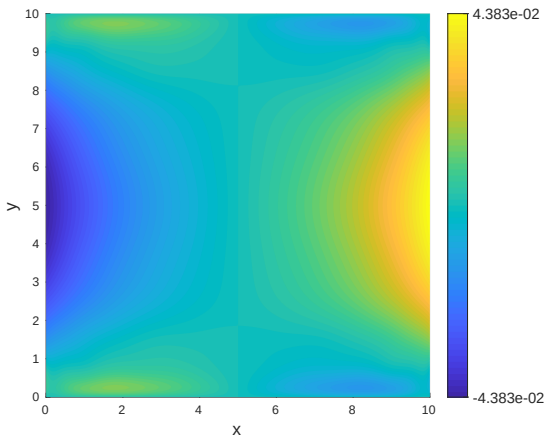

(g) GAUSS, $p = 6$.

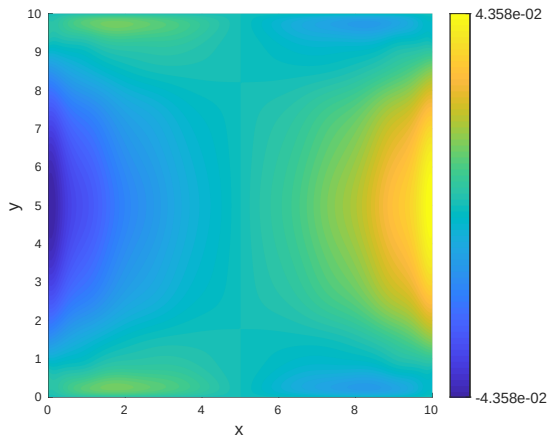

(h) GREVI-R, $p = 6$.

Figure 28: Clamped square plate under a distributed load modeled as an RMC shell: Transverse shear stress σ_{xz} at the midsurface, for slenderness $\frac{L}{t} = 100$, GAUSS and GREVI-R, 8×8 maximally smooth elements with degrees $p = 3$ to 6.

5.3 Scordelis-Lo roof

The Scordelis-Lo roof problem is part of the so-called shell obstacle course [71] and tests a shell element's ability to handle both membrane and bending modes. An 80° arc of a cylinder with radius $R = 25$, length $L = 50$, and thickness $t = 0.25$ or 0.025 is supported on each end by a rigid diaphragm. It is loaded with its own weight $q_z = 90$. The material has Young's Modulus, $E = 4.32 \times 10^8$, and Poisson's ratio $\nu = 0$. Figure 29 shows the problem setup. The initial mesh of the *whole* model consists of 4×4 maximally smooth elements.

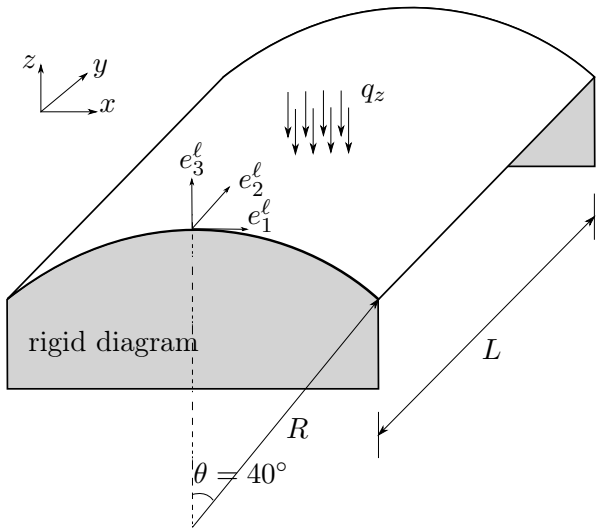

Figure 29: Schematic for the Scordelis-Lo roof problem.

The maximum displacement occurs on the free edge at $\frac{L}{2}$. For $t = 0.25$, the usual FEA solution converges to 0.3006 for KL shells [9] and 0.3024 for RM shells [30, 71]. For $t = 0.025$, the reference solution given in [72] is 32.0 for KL shells and we also take it as the reference solution for RM

shells in this work. The maximum displacement on the free edge at $\frac{L}{2}$ is monitored and results for the KL shell are shown in Figure 30. For $p = 3$ and 4, $t = 0.25$, as shown in Figure 30a, the GREVI-K rule obtains slightly worse results than the GAUSS rule with the initial mesh, but with one refinement they almost achieve identical results that are close to the reference solution. As the degrees increase to $p = 5$ and 6, GREVI-K and GAUSS obtain nearly coincident results and, since locking is alleviated largely by higher-order bases, good results are achieved with even the initial mesh. As the shell thins, i.e., $t = 0.025$, membrane locking becomes more severe and the results converge more slowly for both quadrature rules as shown in Figure 30b. In this case, the GREVI-K rule achieves superior results for $p = 4$ while, for $p = 5$ and 6, the results obtained by GREVI-K and GAUSS hardly differ from each other.

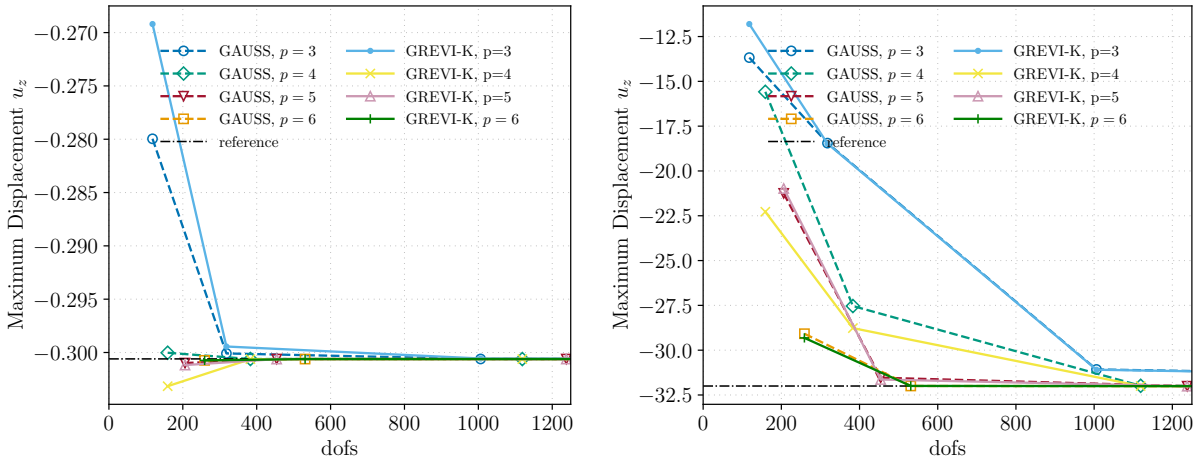

(a) t = 0.25.

(b) t = 0.025.

Figure 30: Scordelis-Lo roof modeled as a KL shell: Convergence of the maximum displacement u_z with GAUSS and GREVI-K, degrees $p = 3$ to 6, and maximally smooth elements. The whole roof is modeled with an initial 4×4 mesh.

Since this problem is membrane dominated, transverse shear locking is not significant. Figure 31 demonstrates that for $p = 3$ to 6 the RMC shell with GAUSS and GREVI-R converges in a similar way as the KL shell with GAUSS and GREVI-K shown in Figure 30. For $p = 2$, the GREVI-R rule underperforms the GAUSS rule but otherwise both rules perform about the same.

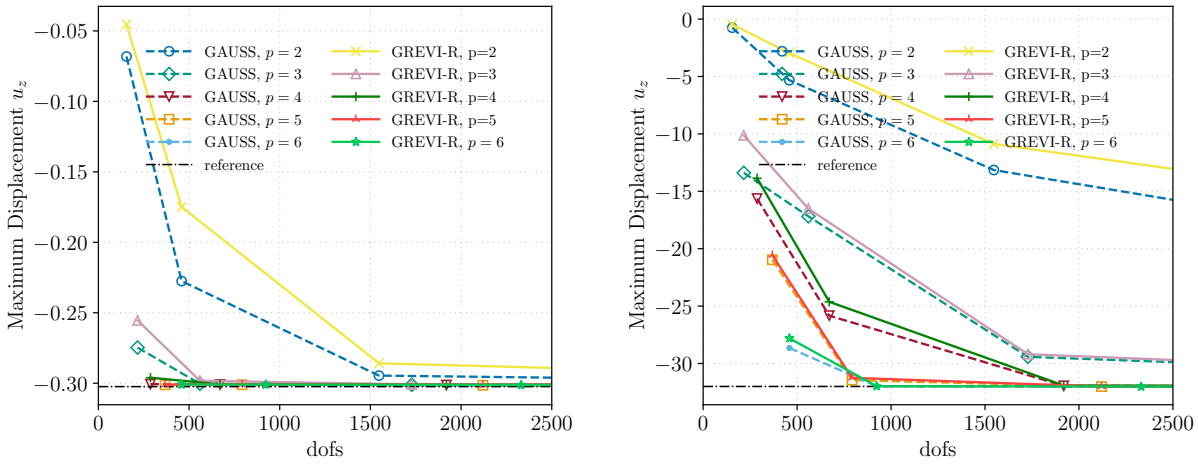

(a) t = 0.25. (b) t = 0.025.

Figure 31: Scordelis-Lo roof modeled as an RMC shell: Convergence of the maximum displacement u_z with GAUSS and GREVI-R, degrees $p = 2$ to 6, and maximally smooth elements. The whole roof is modeled with an initial 4×4 mesh.

We then investigate the stress quality for different quadrature rules. Figure 32 gives a numerical reference of the membrane force n_{11} for thickness $t = 0.25$, which is calculated with 64×64 maximally smooth sextic KL elements and full GAUSS quadrature. The subscript of n_{11} indicates that the membrane force component is along the e_1^ℓ direction of the local Cartesian coordinate system, which is chosen to be the circumferential direction at each point as shown in Figure 29. Figure 33 shows that GREVI-K and GAUSS quadratures obtain comparable membrane force with various numbers of cubic KL elements and significant oscillations occur for coarse meshes. Figure 34 demonstrates that elevating basis orders alleviates the force oscillations shown in Figure 33 with a mesh of 8×8 elements, and GREVI-K performs similarly to GAUSS with various basis degrees. Note that Figures 34e and f still exhibit slightly oscillations, compared with Figure 32, which can be eliminated immediately with a few more elements.

Figure 35 compares the membrane force between GAUSS and GREVI-R with quadratic RMC shell elements. As can be seen, the results oscillate significantly and the values are far from the reference solution shown in Figure 32. Again, the membrane force quality is largely improved by elevating the basis order as shown in Figure 36 with an 8×8 element mesh.

From this problem, we once again conclude that elements of order $p \geq 5$ perform satisfactorily, whereas lower-order elements, with the GAUSS, GREVI-K and GREVI-R quadratures do not.

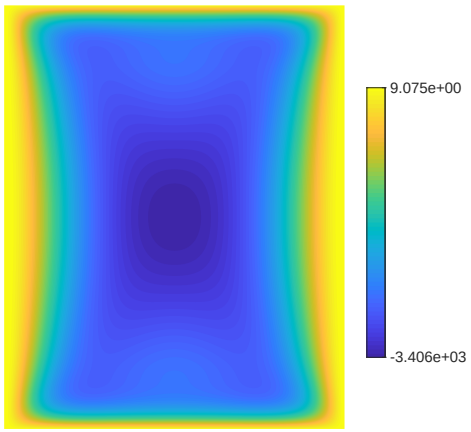

Figure 32: Scordelis-Lo roof modeled as a KL shell: Numerical reference of the membrane force n_{11} for thickness $t = 0.25$, calculated with full GAUSS quadrature and 64×64 maximally smooth elements, $p = 6$.

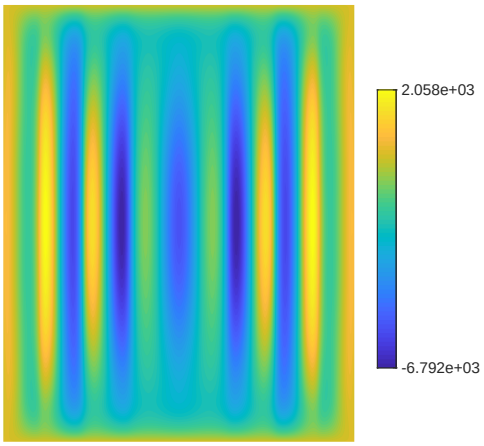

(a) GAUSS, 8×8 elements.

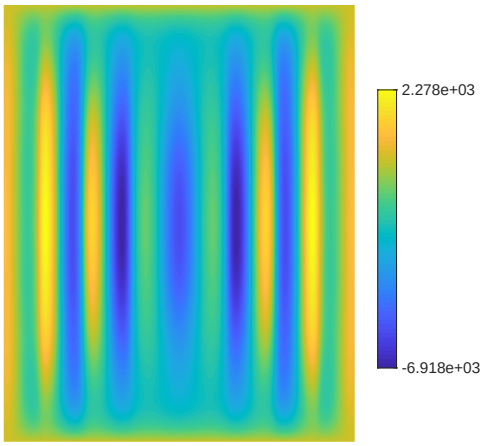

(b) GREVI-K, 8×8 elements.

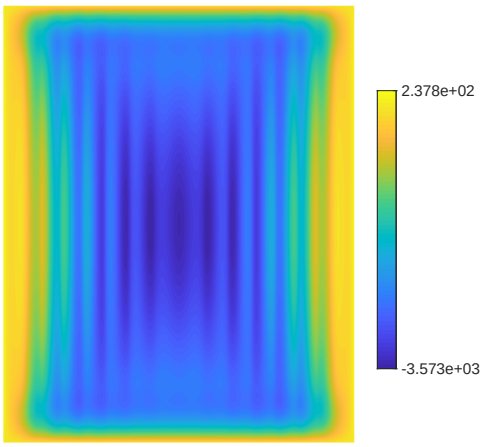

(c) GAUSS, 16×16 elements.

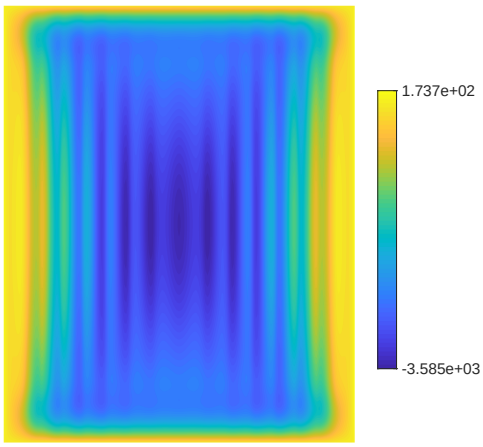

(d) GREVI-K, 16×16 elements.

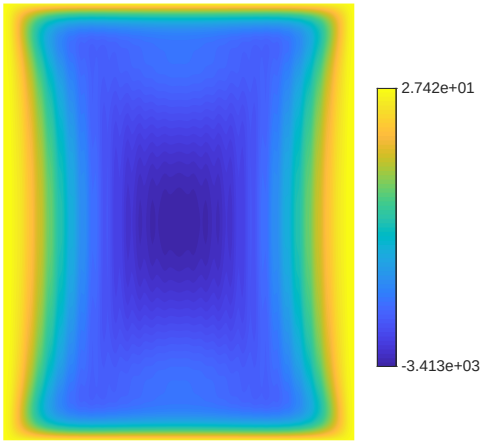

(e) GAUSS, 32×32 elements.

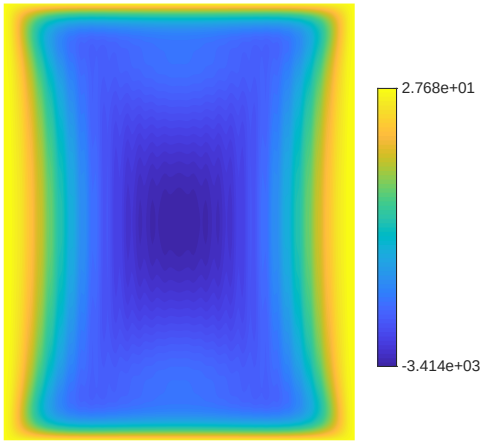

(f) GREVI-K, 32×32 elements.

Figure 33: Scordelis-Lo roof modeled as a KL shell: Membrane force n_{11} for GAUSS and GREVI-K with various numbers of maximally smooth elements, $p = 3$, $t = 0.25$.

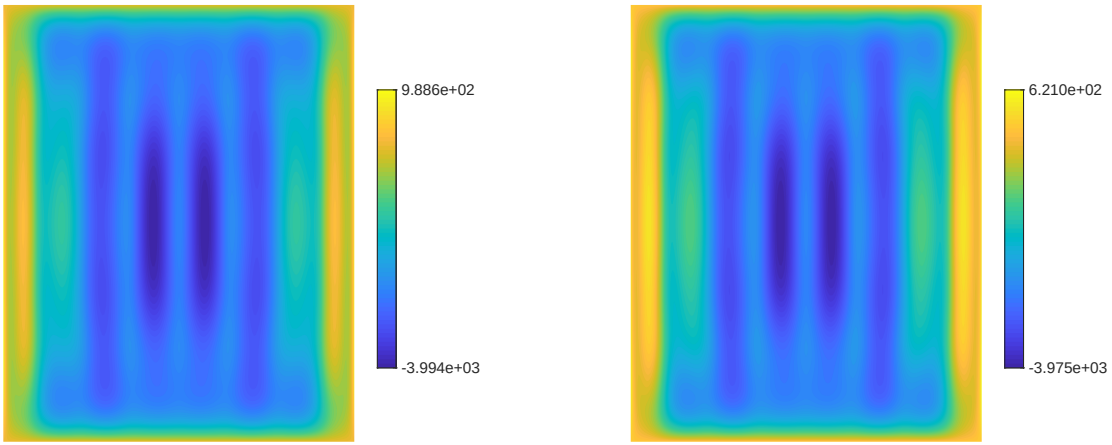

(a) GAUSS, $p = 4$. (b) GREVI-K, $p = 4$.

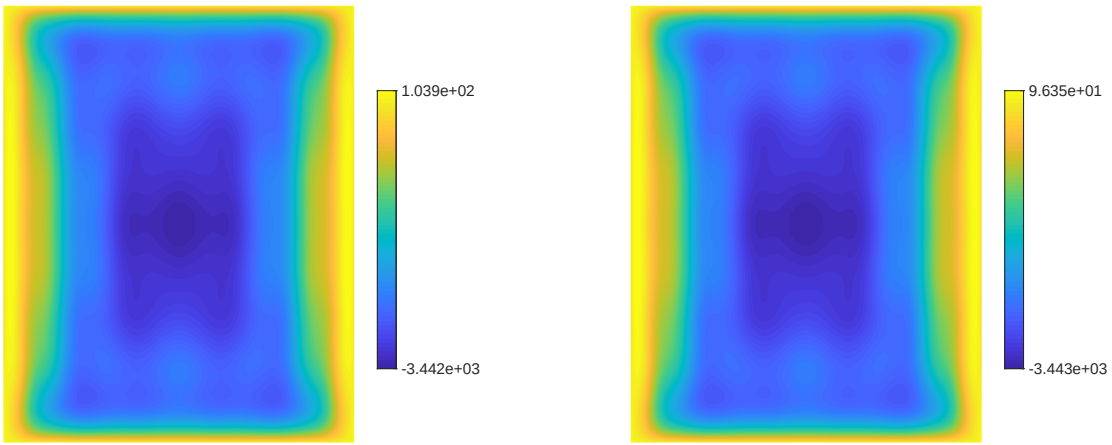

(c) GAUSS, $p = 5$. (d) GREVI-K, $p = 5$.

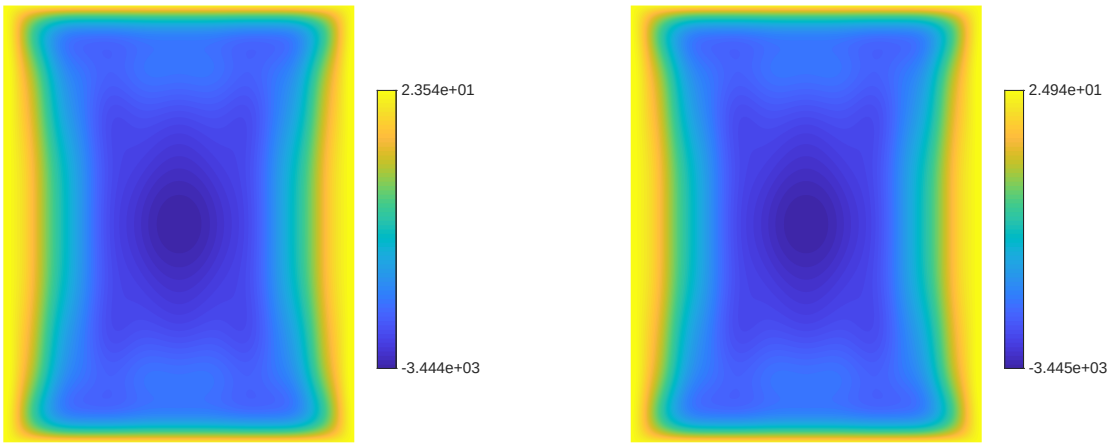

(e) GAUSS, $p = 6$. (f) GREVI-K, $p = 6$.

Figure 34: Scordelis-Lo roof modeled as a KL shell: Membrane force n_{11} for GAUSS and GREVI-K with a mesh of 8×8 maximally smooth elements, $p = 4$ to 6, $t = 0.25$.

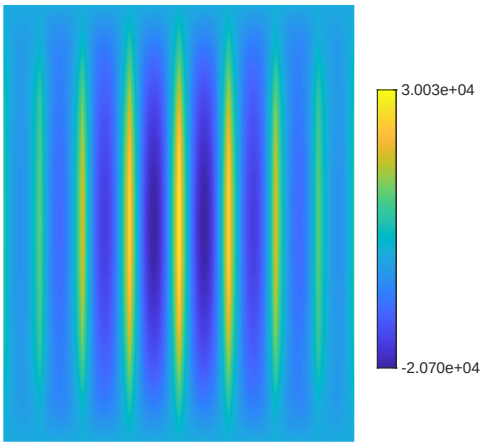

(a) GAUSS, 8×8 elements.

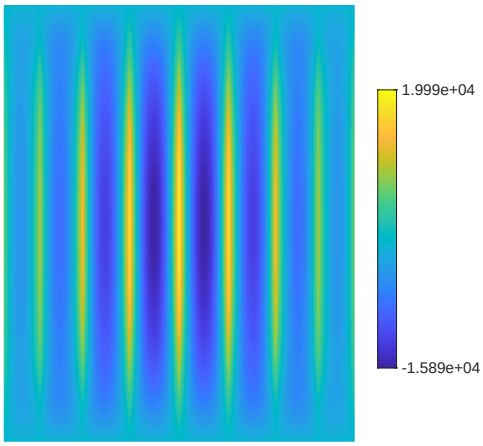

(b) GREVI-R, 8×8 elements.

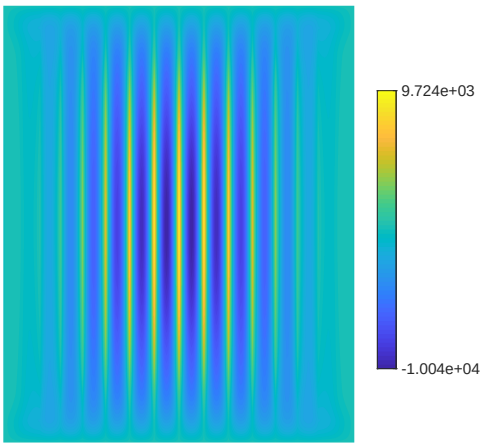

(c) GAUSS, 16×16 elements.

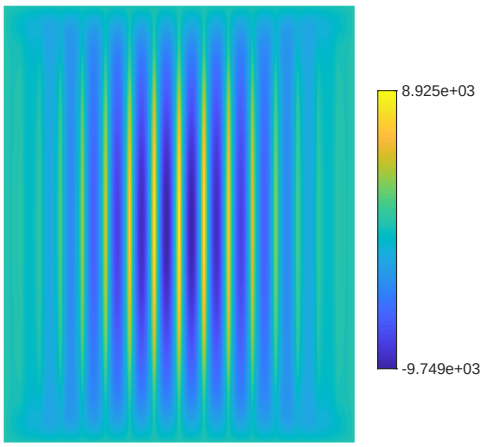

(d) GREVI-R, 16×16 elements.

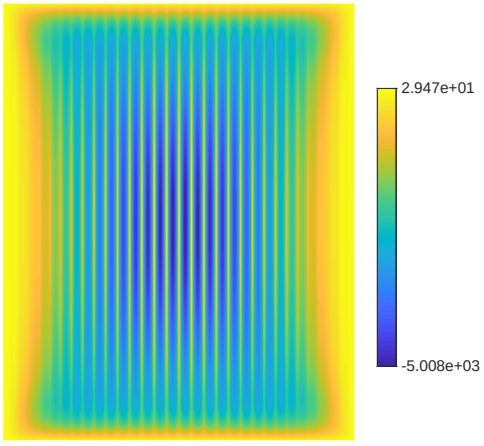

(e) GAUSS, 32×32 elements.

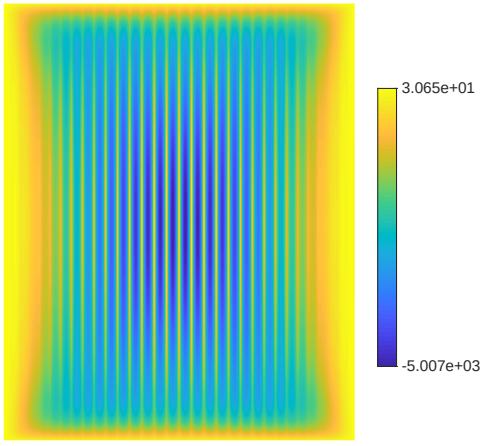

(f) GREVI-R, 32×32 elements.

Figure 35: Scordelis-Lo roof modeled as an RMC shell: Membrane force n_{11} for GAUSS and GREVI-R with various numbers of maximally smooth elements, $p = 2$, $t = 0.25$.

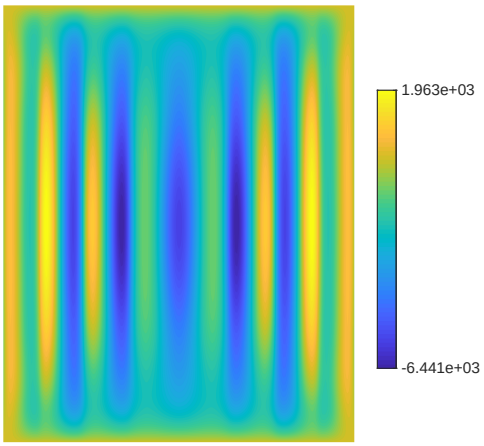

(a) GAUSS, $p = 3$.

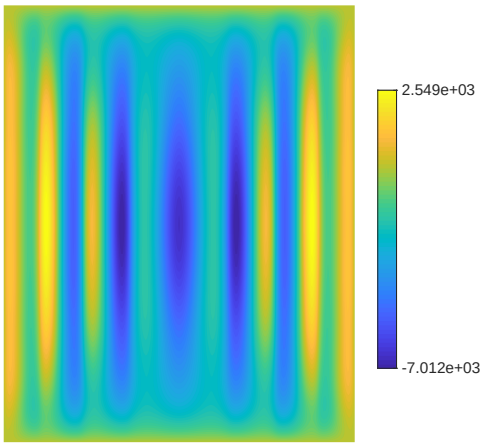

(b) GREVI-R, $p = 3$.

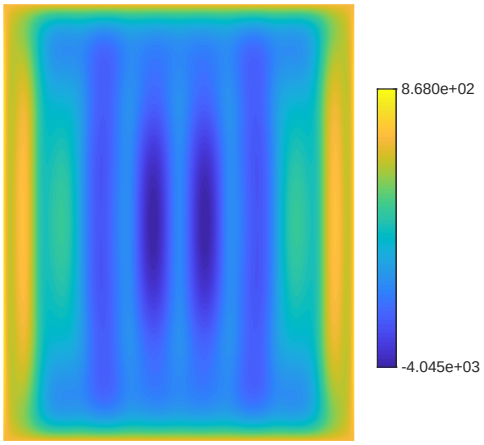

(c) GAUSS, $p = 4$.

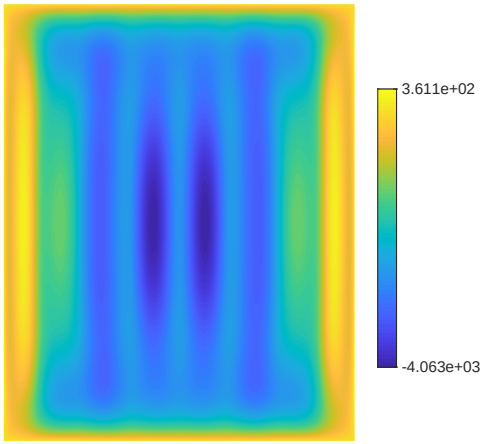

(d) GREVI-R, $p = 4$.

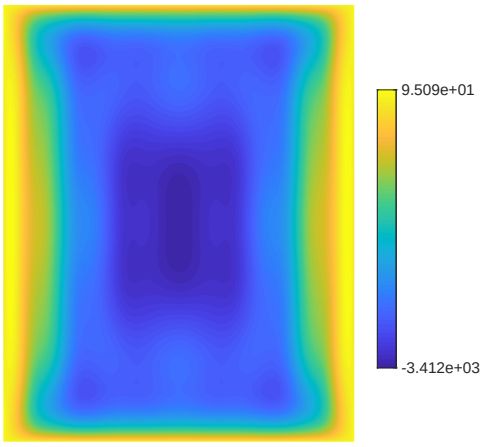

(e) GAUSS, $p = 5$.

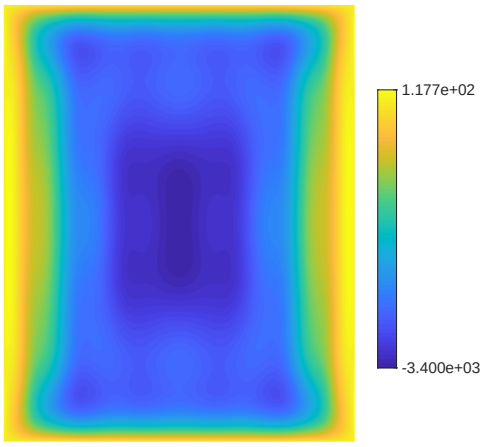

(f) GREVI-R, $p = 5$.

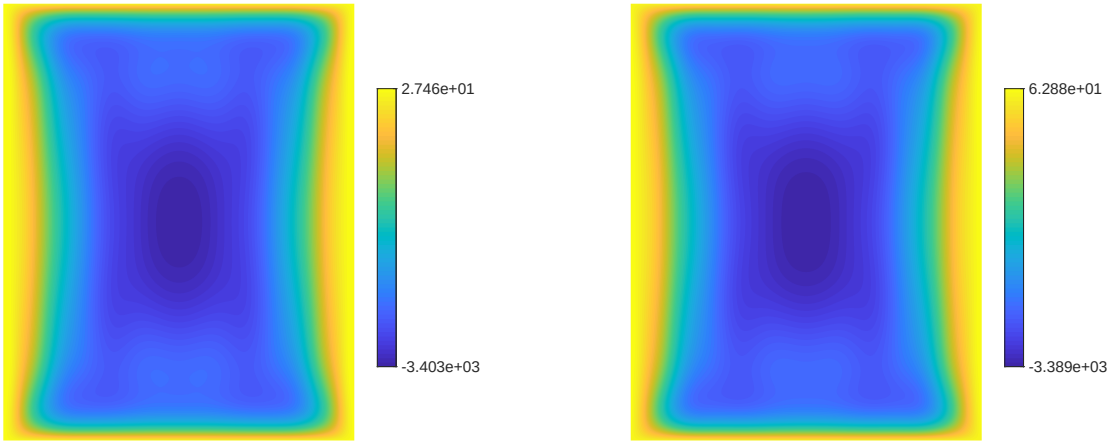

(g) GAUSS, $p = 6$.

(h) GREVI-R, $p = 6$.

Figure 36: Scordelis-Lo roof modeled as an RMC shell: Smoothed membrane force n_{11} for GAUSS and SGREVI-R with 8×8 maximally smooth elements, $p = 3$ to 6, $t = 0.25$.

5.4 Straight cantilever shell subjected to an end moment

In this section, we study the roll-up of a straight cantilever beam (modeled as a shell) as shown in Figure 37. This problem is widely used to test the ability of a shell element to handle large rotations. The beam has a length $L = 12$, width $b = 1$, and thickness $t = 0.1$. It is fixed on one end and subjected to a uniform line moment $m = M/b$ on the free end, which is applied in 10 equal load steps. The material has Young's modulus $E = 1.2 \times 10^6$, and Poisson's ratio $\nu = 0$. The analytical solution for the displacement at the free end is given by $u_x(M) = [\sin(\frac{M}{M_0})\frac{M_0}{M} - 1]L$ and $u_z(M) = [1 - \cos(\frac{M}{M_0})]\frac{M_0}{M}$ with $M_0 = \frac{EI}{L} = \frac{25}{3}$ in [73]. The cantilever beam should roll up into an exact circle for $M = 2\pi M_0$ with a free end rotation of $\theta = 2\pi$. The initial mesh consists of 2×1 maximally smooth B-spline elements with degrees ranging from 2 to 6. Only the RMC shell is used for this problem as it facilitates the application of the end moment exactly. For KL shells, the end moment has to be applied by distributing it over two rows of control points [9] or by weak imposition [74] because of the absence of rotational degrees of freedom.

Figure 38 compares the convergence behavior of the end rotation for the RMC shell with GAUSS and GREVI-R quadratures. As can be seen in Figure 38a, GAUSS performs slightly better than GREVI-R for $p = 2$, but the difference disappears as the polynomial degree increases to $p = 3$, and for $p = 5$ and 6, GREVI-R even achieves better results than GAUSS as shown in 38b.

Figure 39 illustrates the deformed configurations at each load step obtained with GAUSS and GREVI-R for eight maximally smooth elements and various degrees from $p = 2$ to 7. Again, GAUSS (Figures 39a to e) and GREVI-R (Figures 39f to j) give comparable results for all degrees and they both achieve a full circle starting from $p = 5$. Figure 40 shows the load-deflection curves of the free end. As can be seen, with 8 maximally smooth quintic B-spline elements, both GAUSS and GREVI-R rules trace the exact solutions accurately at each load step. Table 7 lists the total iteration count and Newton-Raphson iteration information for the last load step. It is clearly shown that the norms of the global residual force vector for these two quadratures are very close to each other at each iteration. In addition, it takes the same number of iterations, i.e., 110, in total to achieve a full circle for both quadratures.

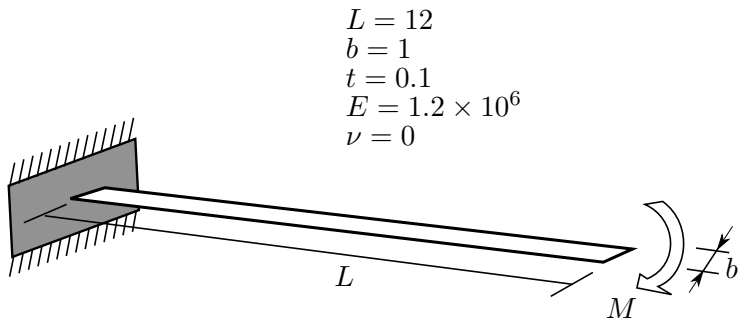

Figure 37: Cantilever beam subjected to end moment.

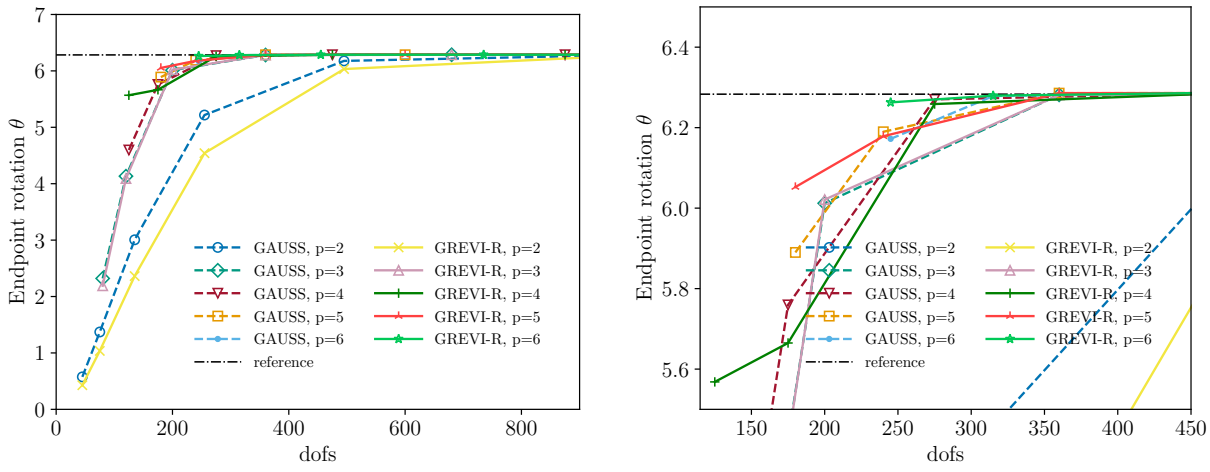

(a) Entire view.

(b) Locally enlarged view.

Figure 38: Cantilever beam subjected to an end moment modeled with the RMC shell: Convergence of the endpoint rotation with GAUSS and GREVI-R, degrees $p = 2$ to 6, maximally smooth elements and 10 load steps. The initial mesh consists of 2×1 elements.

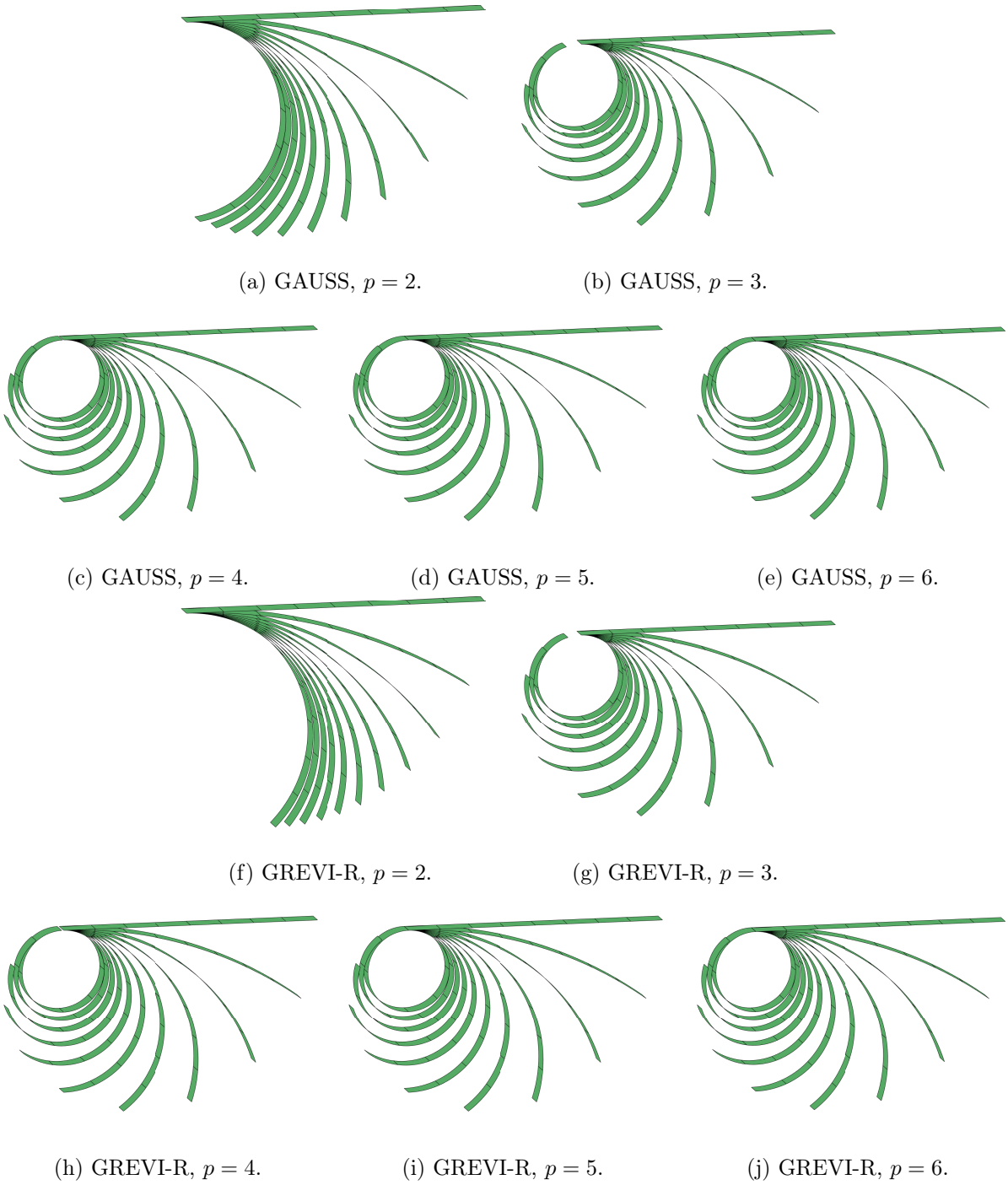

(a) GAUSS, $p = 2$. (b) GAUSS, $p = 3$.

(c) GAUSS, $p = 4$. (d) GAUSS, $p = 5$. (e) GAUSS, $p = 6$.

(f) GREVI-R, $p = 2$. (g) GREVI-R, $p = 3$.

(h) GREVI-R, $p = 4$. (i) GREVI-R, $p = 5$. (j) GREVI-R, $p = 6$.

Figure 39: Cantilever beam subjected to an end moment modeled as an RMC shell: Deformed configurations at each load step for GAUSS and GREVI-R quadrature schemes, $p = 2$ to 6, and eight maximally smooth elements.

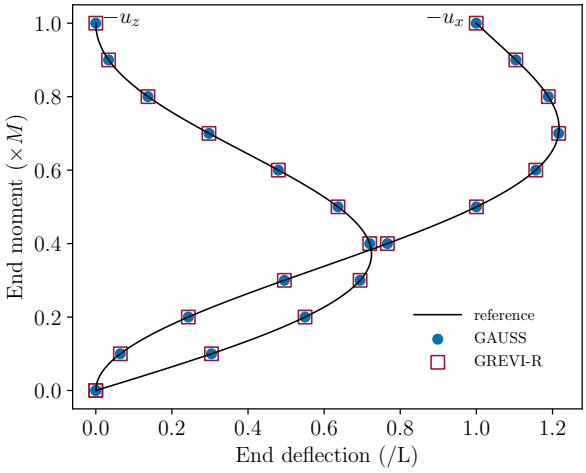

Figure 40: Cantilever beam subjected to an end moment modeled as an RMC shell: load-deflection curve for different quadratures, 8 maximally smooth quintic elements, and 10 load steps.

Table 7: Cantilever beam subjected to an end moment: Newton-Raphson iteration information for the last step for the RMC shell for GAUSS and GREVI-R rules with 8×1 maximally smooth quintic elements and 10 load steps. A residual norm of 1×10^8 is used as the tolerance for convergence; the initial guess of each load step of the Newton-Raphson method is the result of the previous load step.

Last load step iteration	Norm of the global residual vector	
	GAUSS	**GREVI-R**
1	2.1375831e+00	2.1375831e+00
2	1.3784626e+04	1.3772385e+04
3	2.0482486e+03	2.0464766e+03
4	9.0282056e+01	9.0286895e+01
5	1.5191433e+00	1.5372966e+00
6	1.8695243e+01	1.8591616e+01
7	7.2252014e-02	7.2043728e-02
8	2.2772531e+00	2.2790000e+00
9	8.4618374e-04	8.4450531e-04
10	2.1013817e-03	2.1033704e-03
11	1.0278893e-09	1.0262204e-09
Total iteration #	110	110

5.5 Hemispherical shell with a hole

The hemispherical shell problem tests a shell element's ability to represent combined membrane and bending modes [75]. The geometry is a hemisphere with radius $R = 10$, thickness $t = 0.04$, and an 18° hole as shown in Figure 41. Young's modulus is $E = 6.825 \times 10^7$ and Poisson's ratio is $\nu = 0.3$. The hemisphere is first loaded with four point loads, $P = 2$, on the equator with alternating sign. Only one quarter of the hemisphere is modeled due to symmetry. The radial displacement u_y at point B is monitored and compared against a reference solution of 0.0940 [75].

Figure 42 shows that for the RMC shell, GAUSS and GREVI-R again obtain almost identical

results for various degrees $p = 3$ to 6, and locking is largely alleviated by the higher-order bases.

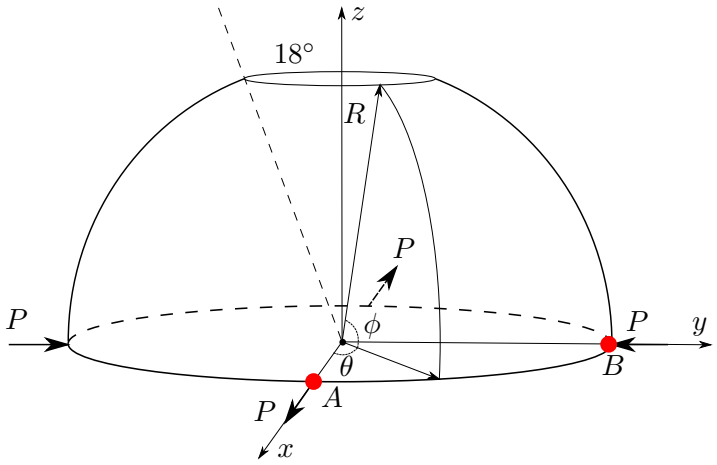

Figure 41: Schematic for the hemispherical shell problem [75].

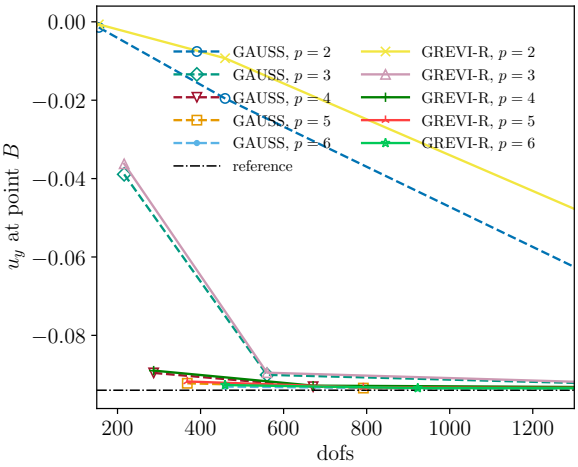

Figure 42: Hemispherical shell modeled as an RMC shell: Convergence of the maximum displacement u_y at point B for load $P = 2$ with GAUSS and GREVI-R rules, degrees $p = 2$ to 6, and maximally smooth elements. One quarter of the hemisphere is discretized with an initial 4×4 mesh.

We then apply the load $P = 200$ which results in large deformations and rotations. In this case, the reference solution of the radial displacement u_y at point B is -5.86799 [30]. Figure 43 shows the convergence of the radial displacement at point B for different quadrature rules with 10 equal load steps. Behaviors consistent with previous benchmarks are observed for this problem, i.e., for $p = 2$, GREVI-R is slightly worse than GAUSS, and for $p = 3$ to 6, they obtain almost identical results. To achieve a relative displacement error $|u_B - u_{\text{ref}}|/|u_{\text{ref}}| < 5\%$ at point B, for $p = 5$, both GAUSS and GREVI-R require 5×5 maximally smooth elements. The deformed configurations of the whole hemisphere are created by mirroring the quarter deformed configurations through symmetric planes, as shown in Figure 44. The Newton-Raphson iteration information for different quadratures is listed in Table 8. As can be seen, GREVI-R rule uses the same number of total iterations as the GAUSS

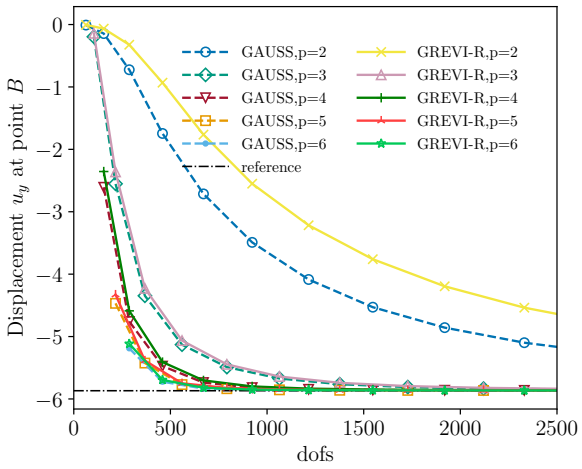

Figure 43: Hemispherical shell modeled as an RMC shell: Convergence of the displacement u_y at point B for load $P = 200$ with GAUSS and GREVI-R, degrees $p = 2$ to 6, maximally smooth elements and 10 load steps.

rule, and the convergence speed of the residual force in the last load step is comparable.

Table 8: Hemispherical shell modeled as an RMC shell: Newton-Raphson iteration behavior for GAUSS and GREVI-R rules with 5×5 maximally smooth quintic B-spline elements and 10 load steps. A residual norm of 1×10^7 is used as the tolerance for convergence; the initial guess of each load step of the Newton-Raphson method is the result of the previous load step.

Last load step iteration	Norm of the global residual vector	
	GAUSS	**GREVI-R**
1	1.4142136e+01	1.4142136e+01
2	2.6921064e+04	2.6655923e+04
3	6.4213095e+01	6.3142890e+01
4	3.0618180e+01	3.0807023e+01
5	1.2151047e+00	1.1772578e+00
6	2.1209916e-02	2.0617638e-02
7	1.6804269e-06	1.4196230e-06
8	1.0093059e-08	8.6660068e-09
Total iteration #	91	91

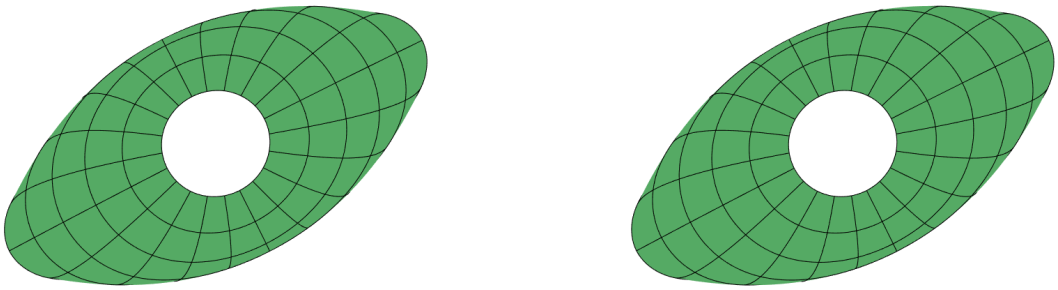

(a) GAUSS. (b) GREVI-R.

Figure 44: Hemispherical shell and the RMC shell: Deformed configurations with GAUSS and GREVI-R, maximally smooth quintic B-spline elements, $P = 200$ and 10 load steps, $|u_y - u_{\text{ref}}|/|u_{\text{ref}}| < 5\%$ at point B.

6 Conclusions

We proposed Greville quadrature schemes for isogeometric shell analysis. The quadrature points are chosen to be standard Greville abscissae for B-splines and NURBS, but the spaces from which the rules emanate are unusual. The proposed scheme for Reissner-Mindlin (RM) shells, referred to as GREVI-R, is a Greville quadrature scheme based on pth-order basis functions, but with one-order-lower continuity across element interfaces than the pth-order, maximally smooth, basis functions used for analysis. The proposed scheme for Kirchhoff-Love (KL) shells, referred to as GREVI-K, constructs the Greville quadrature points based on pth-order basis functions, but with continuity two orders lower than the maximally smooth basis used for analysis. The quadrature weights are determined by solving linear moment fitting equations. Both schemes may be thought of as reduced integration methods, but their properties are unlike those of standard reduced integration methods, which typically engender rank deficiency and spurious modes. Our proposed methods are shown, through eigenvalue analyses, to be free of rank deficiency and spurious modes. At the same time, they achieve similar accuracy, in terms of both displacement and stress, compared with full Gauss quadrature.

Asymptotically, regardless of the polynomial degrees, the proposed methods for RM and KL shell elements only involve four and nine in-plane quadrature points, respectively, per Bézier element, compared to the usual $(p+1) \times (p+1) = (p+1)^2$ in-plane quadrature points for elements with standard "full" Gauss integration. As increasing the basis order does not asymptotically increase degrees-of-freedom or the number of quadrature points for higher-order basis functions, the proposed quadrature schemes provide an efficient and robust way to alleviate locking and provide accurate displacements and stresses for shells. We also note that the proposed quadrature rules also help to improve efficiency of post-processing procedures to remove stress oscillations for lower-order elements.

The present approach to isogeometric RM and KL shell analysis is believed to provide insights to devise new quadrature rules for IGA. The concept of Greville abscissae is also applicable to unstructured spline meshes and offers research opportunities in these areas. However, a number of questions remain and further studies need to be performed. Our work is entirely based on engineering intuition and numerical studies. A mathematical foundation in terms of rigorous convergence rates is lacking. We opted to completely avoid rank deficiency and spurious modes, but this entailed more

Greville points than we initially desired. We think that even better accuracy may be attainable for the lowest-order cases, but our attempts so far have not attained success. We noticed one case in which a negative weight occurred for $p = 4$, but there was no indication of numerical instability for analysis. We also observed in test problems that non-uniform knot vectors may result in negative quadrature weights. The problem of maintaining accuracy and guaranteeing all weights are positive is a problem we hope to study in future work.

In IGA, higher-order curved shell elements mitigate membrane-bending locking. Is this the only simple and general solution to the problem? We don't know, but we think it will take special procedures to do so for lower-order shell elements. In this regard, see the reduced integration work of C. Adam and colleagues [14, 40]. This is a topic warrants further research.

We started this paper quoting Ekkehard Ramm that shells are the prima donnas of structural analysis. The truth of that statement, in the context of numerical analysis, is more evident than ever. There is still much room to improve existing methodology and the search for even better methods goes on.

7 Acknowledgments

This work was supported by the U.S. Department of Energy, Office of Science, Office of Advanced Scientific Computing Research, under Award Number DE-SC0017051, and by the Department of Defense, Navy, Contract: N68335-18-C-0289. Additional funding was also provided by Honeywell Federal Manufacturing & Technologies under Contract No. DE-NA0002839 with the U.S. Department of Energy. Thomas J.R. Hughes and Zhihui Zou also acknowledge support from the Office of Naval Research grant N00014-17-1-2039 and through the Department of Defense, Navy, Contract N68335-18-C-0014, respectively.

A Strain transformation matrix

The Green-Lagrange strain $\mathbf{E}$ can be represented in terms of the contravariant basis vectors $\{\mathbf{G}^i\}_{i=1}^3$ or local Cartesian basis vectors $\{\mathbf{e}_i^\ell\}_{i=1}^3$ as

$$\mathbf{E} = E_{ij}\mathbf{G}^i \otimes \mathbf{G}^j = E_{ij}^\ell \mathbf{e}_i^\ell \otimes \mathbf{e}_j^\ell. \tag{65}$$

By a change of basis, the relation between the local Cartesian components E_{ij}^ℓ and the covariant components E_{ij} can be written as

$$E_{kl}^\ell = \phi_{ik}\phi_{jl}E_{ij}, \tag{66}$$

where

$$\phi_{ik} = \mathbf{G}^i \cdot \mathbf{e}_k^\ell. \tag{67}$$

Note that we do not strictly follow the index notation with respect to the subscripts and superscripts in (65) and (66) because we choose to denote the local Cartesian coordinate bases in a more common way as e_i^ℓ. Through (66), we can transform the reduced Green-Lagrange strain vector $\tilde{\mathbf{E}}$, defined in (25) for a RM shell, into the local Cartesian coordinate system as

$$\tilde{\mathbf{E}}^\ell = \mathbf{T}\tilde{\mathbf{E}}, \tag{68}$$

where the transformation matrix $\mathbf{T}$ is defined as

$$\mathbf{T} = \begin{bmatrix} \phi_{11}^2 & \phi_{21}^2 & \phi_{31}^2 & \phi_{21}\phi_{31} & \phi_{11}\phi_{31} & \phi_{11}\phi_{21} \\ \phi_{12}^2 & \phi_{22}^2 & \phi_{32}^2 & \phi_{22}\phi_{32} & \phi_{12}\phi_{32} & \phi_{12}\phi_{22} \\ \phi_{13}^2 & \phi_{23}^2 & \phi_{33}^2 & \phi_{23}\phi_{33} & \phi_{13}\phi_{33} & \phi_{13}\phi_{23} \\ 2\phi_{12}\phi_{13} & 2\phi_{22}\phi_{23} & 2\phi_{32}\phi_{33} & \phi_{22}\phi_{33}+\phi_{32}\phi_{23} & \phi_{12}\phi_{33}+\phi_{32}\phi_{13} & \phi_{12}\phi_{23}+\phi_{22}\phi_{13} \\ 2\phi_{11}\phi_{13} & 2\phi_{21}\phi_{23} & 2\phi_{31}\phi_{33} & \phi_{21}\phi_{33}+\phi_{31}\phi_{23} & \phi_{11}\phi_{33}+\phi_{31}\phi_{13} & \phi_{11}\phi_{23}+\phi_{21}\phi_{13} \\ 2\phi_{11}\phi_{12} & 2\phi_{21}\phi_{22} & 2\phi_{31}\phi_{32} & \phi_{21}\phi_{32}+\phi_{31}\phi_{22} & \phi_{11}\phi_{32}+\phi_{31}\phi_{12} & \phi_{11}\phi_{22}+\phi_{21}\phi_{12} \end{bmatrix}. \tag{69}$$

For a KL shell, a similar transformation matrix for in-plane strains can be defined as

$$\mathbf{T}^{\mathrm{KL}} = \begin{bmatrix} \phi_{11}\phi_{11} & \phi_{21}\phi_{21} & \phi_{11}\phi_{21} \\ \phi_{12}\phi_{12} & \phi_{22}\phi_{22} & \phi_{12}\phi_{22} \\ 2\phi_{11}\phi_{12} & 2\phi_{21}\phi_{22} & \phi_{11}\phi_{22}+\phi_{21}\phi_{12} \end{bmatrix}. \tag{70}$$

Note that if the elasticity matrices $\mathbf{C}$ and $\mathbf{C}^{\mathrm{KL}}$ defined in Section 3.2 are directly formulated in the curvilinear coordinate system [76, 77], the transformation of the reduced Green-Lagrange strain is not required. However, if the constitutive model is obtained from a independent material library, the elasticity matrices returned may not be defined in the curvilinear coordinate system. In this case, the strain transformation process above offers a flexible way to handle the constitutive model.

B Discretization of the variation of the strain for RM shells

In this section, we introduce useful derivations from [30, 62], which are necessary for understanding and implementing the RM shell formulation employed in this work. This formulation defines the current director $\mathbf{d}$ at the quadrature points based on the continuous rotational concept, which has been shown to be more accurate in [30, 78], especially for higher-order spline bases, than interpolating $\mathbf{d}$ through the nodal director vectors in a discrete manner [11]. We refer interested readers to [30, 62] for more details.

B.1 Definition of the current director

The current director is defined as

$$\mathbf{d}^i(\xi^\alpha) = \Delta\mathbf{R}\mathbf{d}^{i-1}(\xi^\alpha) \tag{71}$$

where the superscripts i and $i-1$ indicate Newton-Raphson iterates, $\Delta\mathbf{R}$ is the incremental rotation tensor, and

$$\Delta\mathbf{R} = \mathbf{I} + c_1\boldsymbol{\Delta\Omega} + c_2\boldsymbol{\Delta\Omega}^2, \quad c_1 = \frac{\sin\Delta\omega}{\Delta\omega}, \quad c_2 = \frac{1-\cos\Delta\omega}{\Delta\omega^2}, \quad \Delta\omega = |\boldsymbol{\Delta\omega}| \tag{72}$$

where $\mathbf{I}$ is a 3×3 identity matrix, $\boldsymbol{\Delta\omega} = \boldsymbol{\Delta\omega}(\xi^\alpha) \in \mathbb{R}^d$ is the axial vector of the global incremental rotation at each quadrature point and

$$\boldsymbol{\Delta\Omega} = \begin{bmatrix} 0 & -\Delta\omega_3 & \Delta\omega_2 \\ \Delta\omega_3 & 0 & -\Delta\omega_1 \\ -\Delta\omega_2 & \Delta\omega_1 & 0 \end{bmatrix}. \tag{73}$$

The derivatives of the director can be written as

$$\mathbf{d}^i_{,\alpha} = \Delta\mathbf{R}_{,\alpha}\mathbf{d}^{i-1} + \Delta\mathbf{R}\,\mathbf{d}^{i-1}_{,\alpha}, \tag{74}$$

where

$$\Delta\mathbf{R}_{,\alpha} = c_{1,\alpha}\Delta\boldsymbol{\Omega} + c_1\Delta\boldsymbol{\Omega}_{,\alpha} + c_{2,\alpha}\Delta\boldsymbol{\Omega}^2 + c_2(\Delta\boldsymbol{\Omega}_{,\alpha}\Delta\boldsymbol{\Omega} + \Delta\boldsymbol{\Omega}\,\Delta\boldsymbol{\Omega}_{,\alpha}) \tag{75}$$

$$\Delta\boldsymbol{\Omega}_{,\alpha} = \operatorname{skew}\boldsymbol{\Delta\omega}_{,\alpha}, \quad c_{1,\alpha} = \Delta\omega_{,\alpha}\frac{\Delta\omega\cos\Delta\omega - \sin\Delta\omega}{\Delta\omega^2}, \quad c_{2,\alpha} = \Delta\omega_{,\alpha}\frac{\Delta\omega\sin\Delta\omega - 2 + 2\cos\Delta\omega}{\Delta\omega^3}, \tag{76}$$

$$\Delta\omega_{,\alpha} = \frac{\boldsymbol{\Delta\omega}_{,\alpha}\cdot\boldsymbol{\Delta\omega}}{\Delta\omega}. \tag{77}$$

Note that when $\Delta\omega$ is very small we take the limit values

$$c_1 = 1\ , \quad c_2 = \frac{1}{2} \quad \text{and} \quad c_{1,\alpha} = c_{2,\alpha} = \Delta\omega_{,\alpha} = 0 \tag{78}$$

to ensure numerical stability.

B.2 Discretization of the variation of the current director

The first variation of $\mathbf{d}$ is derived in [62] and can be written as

$$\delta\mathbf{d} = \mathbf{W}^{\mathrm{T}}\delta\boldsymbol{\omega}, \quad \mathbf{W} = \operatorname{skew}\mathbf{d}, \tag{79}$$

and the derivatives can be written as

$$\delta\mathbf{d}_{,\alpha} = \mathbf{W}^{\mathrm{T}}_{,\alpha}\delta\boldsymbol{\omega} + \mathbf{W}^{\mathrm{T}}\delta\boldsymbol{\omega}_{,\alpha}, \quad \mathbf{W}_{,\alpha} = \operatorname{skew}\mathbf{d}_{,\alpha}. \tag{80}$$

The second variation of $\mathbf{d}$ can be written as

$$\mathbf{h}\cdot\Delta\delta\mathbf{d} = \delta\boldsymbol{\omega}^{\mathrm{T}}\mathbf{M}(\mathbf{h})\Delta\boldsymbol{\omega}, \tag{81}$$

where $\mathbf{h}$ is an arbitrary vector and

$$\mathbf{M}(\mathbf{h}) = \frac{1}{2}(\mathbf{d}\mathbf{h}^{\mathrm{T}} + \mathbf{h}\mathbf{d}^{\mathrm{T}}) - (\mathbf{d}\cdot\mathbf{h})\mathbf{I}. \tag{82}$$

The derivatives of $\Delta\delta\mathbf{d}$ can be written as

$$\mathbf{h}\cdot\Delta\delta\mathbf{d}_{,\alpha} = \delta\boldsymbol{\omega}^{\mathrm{T}}_{,\alpha}\mathbf{M}(\mathbf{h})\Delta\boldsymbol{\omega} + \delta\boldsymbol{\omega}^{\mathrm{T}}\mathbf{M}_{,\alpha}(\mathbf{h})\Delta\boldsymbol{\omega} + \delta\boldsymbol{\omega}^{\mathrm{T}}\mathbf{M}(\mathbf{h})\Delta\boldsymbol{\omega}_{,\alpha}, \tag{83}$$

where

$$\mathbf{M}(\mathbf{h})_{,\alpha} = \frac{1}{2}(\mathbf{d}_{,\alpha}\mathbf{h}^{\mathrm{T}} + \mathbf{h}\mathbf{d}^{\mathrm{T}}_{,\alpha}) - (\mathbf{d}_{,\alpha}\cdot\mathbf{h})\mathbf{I}. \tag{84}$$

The increment of the axial vector and its derivatives are discretized with the spline basis defined in Section 2, e.g., B-spline basis $\{N_I\}_{I=1}^n$, as

$$\Delta\boldsymbol{\omega}^h = \sum_I^n N_I\Delta\boldsymbol{\omega}_I = \sum_I^n N_I\mathbf{T}_{3I}\Delta\boldsymbol{\beta}_I \quad \text{and} \quad \Delta\boldsymbol{\omega}^h_{,\alpha} = \sum_I^n N_{I,\alpha}\Delta\boldsymbol{\omega}_I = \sum_I^n N_{I,\alpha}\mathbf{T}_{3I}\Delta\boldsymbol{\beta}_I \tag{85}$$

where

$$\mathbf{T}_{3I} = \begin{cases} [\mathbf{a}_{1I} \quad \mathbf{a}_{2I}] & \text{for nodes in the smooth regions} \\ \mathbf{I}_{3\times3} & \text{for nodes along kinks} \end{cases} \tag{86}$$

$$\mathbf{a}_{\alpha I} = \Delta\mathbf{R}(\Delta\boldsymbol{\omega}_I)\mathbf{a}^{i-1}_{\alpha I}, \quad \mathbf{a}^{i-1}_{\alpha I} \text{ are the current nodal basis vectors} \tag{87}$$

$$\Delta\boldsymbol{\omega}_I = \mathbf{T}_{3I}\Delta\beta_I, \quad \Delta\beta_I \text{ is the local incremental nodal rotation vector.} \tag{88}$$

Note that to avoid drilling degrees-of-freedom, in smooth area, $\Delta\beta_I$ is chosen to be the local incremental nodal rotation vector which has only two components. However, along kinks, $\Delta\beta_I$ is the global incremental nodal rotation vector, i.e., $\Delta\beta_I = \Delta\boldsymbol{\omega}_I$, which has three components. In this case, the matrix $\mathbf{T}_{3I}$ is reduced to the identity as shown in (86).

The first variation of the director and its derivatives are discretized as

$$\delta\mathbf{d}^h = \mathbf{W}^{h\mathrm{T}}\delta\boldsymbol{\omega}^h = \sum_{I=1}^{n}\mathbf{T}_I\delta\boldsymbol{\beta}_I, \tag{89}$$

$$\delta\mathbf{d}^h_{,\alpha} = \sum_{I=1}^{n}\mathbf{T}_{I,\alpha}\delta\boldsymbol{\beta}_I, \tag{90}$$

where

$$\mathbf{T}_I = \mathbf{W}^{h\mathrm{T}}N_I\mathbf{T}_{3I}, \tag{91}$$

$$\mathbf{T}_{I,\alpha} = [\mathbf{W}^{h\mathrm{T}}_{,\alpha}N_I + \mathbf{W}^{h\mathrm{T}}N_{I,\alpha}]\mathbf{T}_{3I}. \tag{92}$$

The second variation of the director and its derivatives are discretized as

$$\mathbf{h}\cdot\Delta\delta\mathbf{d}^h = \sum_{I=1}^{n_p}\sum_{J=1}^{n_p}\delta\boldsymbol{\beta}_I^{\mathrm{T}}\mathbf{T}_{3I}^{\mathrm{T}}N_I\mathbf{M}^h(\mathbf{h})N_J\mathbf{T}_{3J}\delta\boldsymbol{\beta}_J = \sum_{I=1}^{n_p}\sum_{J=1}^{n_p}\delta\boldsymbol{\beta}_I^{\mathrm{T}}\hat{\boldsymbol{q}}_{IJ}^{\beta\beta}(\mathbf{h})\delta\boldsymbol{\beta}_J \tag{93}$$

$$\mathbf{h}\cdot\Delta\delta\mathbf{d}^h_{,\alpha} = \sum_{I=1}^{n_p}\sum_{J=1}^{n_p}\delta\boldsymbol{\beta}_I^{\mathrm{T}}\mathbf{T}_{3I}^{\mathrm{T}}[N_{I,\alpha}\mathbf{M}^h(\mathbf{h})N_J + N_I\mathbf{M}^h_{,\alpha}(\mathbf{h})N_J + N_I\mathbf{M}^h(\mathbf{h})N_{J,\alpha}]\mathbf{T}_{3J}\delta\boldsymbol{\beta}_J \tag{94}$$

$$= \sum_{I=1}^{n_p}\sum_{J=1}^{n_p}\delta\boldsymbol{\beta}_I^{\mathrm{T}}\hat{\boldsymbol{m}}_{IJ,\alpha}^{\beta\beta}(\mathbf{h})\delta\boldsymbol{\beta}_J \tag{95}$$

where

$$\hat{\boldsymbol{q}}_{IJ}^{\beta\beta}(\mathbf{h}) = \mathbf{T}_{3I}^{\mathrm{T}}N_I\mathbf{M}^h(\mathbf{h})N_J\mathbf{T}_{3J} \tag{96}$$

$$\hat{\boldsymbol{m}}_{IJ,\alpha}^{\beta\beta}(\mathbf{h}) = \mathbf{T}_{3I}^{\mathrm{T}}[N_{I,\alpha}\mathbf{M}^h(\mathbf{h})N_J + N_I\mathbf{M}^h_{,\alpha}(\mathbf{h})N_J + N_I\mathbf{M}^h(\mathbf{h})N_{J,\alpha}]\mathbf{T}_{3J} \tag{97}$$

and $\mathbf{M}^h(\mathbf{h})$ and $\mathbf{M}^h_{,\alpha}(\mathbf{h})$ are calculated by inserting interpolated values of $\mathbf{h}^h$ and $\mathbf{h}^h_{,\alpha}$ into (82) and (84), respectively.

B.3 Matrix formulation

The discretized midsurface $\bar{\mathbf{x}}^h$ in the current configuration can be written as

$$\bar{\mathbf{x}}^h = \bar{\mathbf{X}}^h + \mathbf{u}^h, \tag{98}$$

where the discretized initial midsurface $\bar{\mathbf{X}}^h$ and displacement $\mathbf{u}^h$ are represented as

$$\bar{\mathbf{X}}^h = \sum_{I=1}^{n}\mathbf{P}_I N_I, \tag{99}$$

$$\mathbf{u}^h = \sum_{I=1}^{n}\mathbf{u}_I N_I. \tag{100}$$

Substituting $\bar{\mathbf{x}}^h$, $\delta\mathbf{d}^h$ and $\delta\mathbf{d}^h_{,\alpha}$, computed with (98), (89) and (90), into (43) to (45) gives the discretized first variation of the strains as

$$\begin{aligned}
\delta\boldsymbol{\epsilon}^h &= \sum_{I=1}^{n} \begin{bmatrix} N_{I,1}\bar{\mathbf{x}}_{,1}^{\mathrm{T}} \\ N_{I,2}\bar{\mathbf{x}}_{,2}^{\mathrm{T}} \\ N_{I,1}\bar{\mathbf{x}}_{,2}^{\mathrm{T}} + N_{I,2}\bar{\mathbf{x}}_{,1}^{\mathrm{T}} \end{bmatrix} \delta\mathbf{u}_I, \\
\delta\boldsymbol{\kappa}^h &= \sum_{I=1}^{n} \begin{bmatrix} N_{I,1}\mathbf{d}_{,1}^{\mathrm{T}} & \bar{\mathbf{x}}_{,1}^{\mathrm{T}}\mathbf{T}_{I,1} \\ N_{I,2}\mathbf{d}_{,2}^{\mathrm{T}} & \bar{\mathbf{x}}_{,2}^{\mathrm{T}}\mathbf{T}_{I,2} \\ N_{I,2}\mathbf{d}_{,1}^{\mathrm{T}} + N_{I,1}\mathbf{d}_{,2}^{\mathrm{T}} & \bar{\mathbf{x}}_{,1}^{\mathrm{T}}\mathbf{T}_{I,2} + \bar{\mathbf{x}}_{,2}^{\mathrm{T}}\mathbf{T}_{I,1} \end{bmatrix} \begin{bmatrix} \delta\mathbf{u}_I \\ \delta\boldsymbol{\beta}_I \end{bmatrix}, \\
\delta\boldsymbol{\gamma}^h &= \sum_{I=1}^{n} \begin{bmatrix} N_{I,1}\mathbf{d}^{\mathrm{T}} & \bar{\mathbf{x}}_{,1}^{\mathrm{T}}\mathbf{T}_I \\ N_{I,2}\mathbf{d}^{\mathrm{T}} & \bar{\mathbf{x}}_{,2}^{\mathrm{T}}\mathbf{T}_I \end{bmatrix} \begin{bmatrix} \delta\mathbf{u}_I \\ \delta\boldsymbol{\beta}_I \end{bmatrix}.
\end{aligned} \tag{101}$$

Substituting $\bar{\mathbf{x}}^h$, $\delta\mathbf{d}^h$, $\Delta\delta\mathbf{d}^h$, $\delta\mathbf{d}^h_{,\alpha}$ and $\Delta\delta\mathbf{d}^h_{,\alpha}$, computed with (98), (89), (93), (90) and (95), into (46) to (48) gives the discretized second variation of the strains as

$$\Delta\delta\boldsymbol{\epsilon}^h = \begin{bmatrix} \Delta\delta\epsilon^h_{11} \\ \Delta\delta\epsilon^h_{22} \\ 2\Delta\delta\epsilon^h_{12} \end{bmatrix}, \quad \Delta\delta\boldsymbol{\kappa}^h = \begin{bmatrix} \Delta\delta\kappa^h_{11} \\ \Delta\delta\kappa^h_{22} \\ 2\Delta\delta\kappa^h_{12} \end{bmatrix}, \quad \text{and} \quad \Delta\delta\boldsymbol{\gamma}^h = \begin{bmatrix} \Delta\delta\gamma^h_1 \\ \Delta\delta\gamma^h_2 \end{bmatrix}, \tag{102}$$

where

$$\Delta\delta\varepsilon^h_{\alpha\beta} = \frac{1}{2}(\delta\bar{\mathbf{x}}^h_{,\alpha}\cdot\Delta\bar{\mathbf{x}}^h_{,\beta} + \delta\bar{\mathbf{x}}^h_{,\beta}\cdot\Delta\bar{\mathbf{x}}^h_{,\alpha}) = \sum_{I=1}^{n_p}\sum_{J=1}^{n_p}\frac{1}{2}\delta\mathbf{u}_I^T(N_{I,\alpha}N_{J,\beta} + N_{I,\beta}N_{J,\alpha})\mathbf{I}\Delta\mathbf{u}_J, \tag{103}$$

$$\Delta\delta\kappa^h_{\alpha\beta} = \frac{1}{2}\sum_{I=1}^{n_p}\sum_{J=1}^{n_p}\delta\mathbf{u}_I^T[N_{I,\alpha}\mathbf{T}_{J,\beta} + N_{I,\beta}\mathbf{T}_{J,\alpha}]\Delta\boldsymbol{\beta}_J + \delta\boldsymbol{\beta}_I^T[N_{J,\beta}\mathbf{T}_{I,\alpha}^{\mathrm{T}} + N_{J,\alpha}\mathbf{T}_{I,\beta}^{\mathrm{T}}]\Delta\mathbf{u}_J \tag{104}$$

$$+ \delta\boldsymbol{\beta}_I^T(\hat{\boldsymbol{m}}^{\beta\beta}_{IJ,\beta}(\bar{\mathbf{x}}_{,\alpha}) + \hat{\boldsymbol{m}}^{\beta\beta}_{IJ,\alpha}(\bar{\mathbf{x}}_{,\beta}))\Delta\boldsymbol{\beta}_J, \tag{105}$$

$$\Delta\delta\gamma^h_\alpha = \delta\mathbf{u}_I^T N_{I,\alpha}\mathbf{T}_J\Delta\boldsymbol{\beta}_J + \delta\boldsymbol{\beta}_I^T N_{J,\alpha}\mathbf{T}_I^{\mathrm{T}}\Delta\mathbf{u}_J + \delta\boldsymbol{\beta}_I^T\hat{\boldsymbol{q}}^{\beta\beta}_{IJ}(\bar{\mathbf{x}}_{,\alpha})\Delta\boldsymbol{\beta}_J. \tag{106}$$

Substitution of (101) into the first equation of (42) leads to the nodal strain-displacement matrix

$$\mathbf{B}_I = \begin{bmatrix} N_{I,1}\bar{\mathbf{x}}_{,1}^{\mathrm{T}} + \xi^3 N_{I,1}\mathbf{d}_{,1}^{\mathrm{T}} & \xi^3\bar{\mathbf{x}}_{,1}^{\mathrm{T}}\mathbf{T}_{I,1} \\ N_{I,2}\bar{\mathbf{x}}_{,2}^{\mathrm{T}} + \xi^3 N_{I,2}\mathbf{d}_{,2}^{\mathrm{T}} & \xi^3\bar{\mathbf{x}}_{,2}^{\mathrm{T}}\mathbf{T}_{I,2} \\ N_{I,2}\bar{\mathbf{x}}_{,1}^{\mathrm{T}} + N_{I,1}\bar{\mathbf{x}}_{,2}^{\mathrm{T}} + \xi^3 N_{I,2}\mathbf{d}_{,1}^{\mathrm{T}} + \xi^3 N_{I,1}\mathbf{d}_{,2}^{\mathrm{T}} & \xi^3\bar{\mathbf{x}}_{,1}^{\mathrm{T}}\mathbf{T}_{I,2} + \xi^3\bar{\mathbf{x}}_{,2}^{\mathrm{T}}\mathbf{T}_{I,1} \\ N_{I,1}\mathbf{d}^{\mathrm{T}} & \bar{\mathbf{x}}_{,1}^{\mathrm{T}}\mathbf{T}_I \\ N_{I,2}\mathbf{d}^{\mathrm{T}} & \bar{\mathbf{x}}_{,2}^{\mathrm{T}}\mathbf{T}_I \end{bmatrix}. \tag{107}$$

Therefore, the IJth nodal submatrix of the material stiffness matrix can be written as

$$\mathbf{K}^{\mathrm{mat}}_{IJ} = \int_\Omega \mathbf{B}_I^{\mathrm{T}}\mathbf{C}\mathbf{B}_J \mathrm{d}\Omega. \tag{108}$$

Substitution of (102) into (42) and (41) leads the IJth nodal submatrix of the geometric stiffness matrix as

$$\mathbf{K}^{\mathrm{geom}}_{IJ} = \int_\Omega \begin{bmatrix} \mathbf{K}^{\mathrm{geom}}_{IJ_{11}} & \mathbf{K}^{\mathrm{geom}}_{IJ_{12}} \\ \mathbf{K}^{\mathrm{geom}}_{IJ_{21}} & \mathbf{K}^{\mathrm{geom}}_{IJ_{22}} \end{bmatrix} \mathrm{d}\Omega, \tag{109}$$

where

$$\mathbf{K}^{\text{geom}}_{IJ_{11}} =(N_{I,1}N_{J,1}\tilde{S}^1 + N_{I,2}N_{J,2}\tilde{S}^2 + N_{I,1}N_{J,2}\tilde{S}^3 + N_{I,2}N_{J,1}\tilde{S}^3)\mathbf{I}, \tag{110}$$

$$\mathbf{K}^{\text{geom}}_{IJ_{12}} =\xi^3\tilde{S}^1N_{I,1}\mathbf{T}_{J,1} + \xi^3\tilde{S}^2N_{I,2}\mathbf{T}_{J,2} + \xi^3\tilde{S}^3(N_{I,1}\mathbf{T}_{J,2} + N_{I,2}\mathbf{T}_{J,1}) + (\tilde{S}^4N_{I,1} + \tilde{S}^5N_{I,2})\mathbf{T}_J, \tag{111}$$

$$\mathbf{K}^{\text{geom}}_{IJ_{21}} =\xi^3\tilde{S}^1N_{J,1}\mathbf{T}^{\mathrm{T}}_{I,1} + \xi^3\tilde{S}^2N_{J,2}\mathbf{T}^{\mathrm{T}}_{I,2} + \xi^3\tilde{S}^3(N_{J,1}\mathbf{T}^{\mathrm{T}}_{I,2} + N_{J,2}\mathbf{T}^{\mathrm{T}}_{I,1}) + (\tilde{S}^4N_{J,1} + \tilde{S}^5N_{J,2})\mathbf{T}^{\mathrm{T}}_I, \tag{112}$$

$$\mathbf{K}^{\text{geom}}_{IJ_{22}} =\xi^3\tilde{S}^1\hat{\mathbf{m}}^{\beta\beta}_{IJ,1}(\bar{\mathbf{x}}_{,1}) + \xi^3\tilde{S}^2\hat{\mathbf{m}}^{\beta\beta}_{IJ,2}(\bar{\mathbf{x}}_{,2}) + \xi^3\tilde{S}^3(\hat{\mathbf{m}}^{\beta\beta}_{IJ,1}(\bar{\mathbf{x}}_{,2}) + \hat{\mathbf{m}}^{\beta\beta}_{IJ,2}(\bar{\mathbf{x}}_{,1})) + \tilde{S}^4\hat{\boldsymbol{q}}^{\beta\beta}_{IJ}(\bar{\mathbf{x}}_{,1}) + \tilde{S}^5\hat{\boldsymbol{q}}^{\beta\beta}_{IJ}(\bar{\mathbf{x}}_{,2}). \tag{113}$$

Here $\tilde{S}^1$ to $\tilde{S}^5$ are the stress components of $\tilde{\mathbf{S}}$ calculated by (35).

The nodal internal force vector $\mathbf{F}^{\text{int}}_I$ is defined as

$$\mathbf{F}^{\text{int}}_I = \int_\Omega \mathbf{B}^{\mathrm{T}}_I\tilde{\mathbf{S}}\,\mathrm{d}\Omega. \tag{114}$$

The external force vector is calculated using standard approaches for RM shells [61] and omitted here.

C Discretization of the variation of the strain for KL shells

In this section, we introduce the discretizations of the variations of strains and their matrix formulations for KL shells [9, 79].

C.1 Discretization of the variation of the current director

The current director $\mathbf{d}$ for KL shells is defined as (30). The first and second variations of $\mathbf{d}$ are given in [79] as

$$\delta\mathbf{d} =\frac{1}{\|\mathbf{p}\|}(\mathbf{I} - \mathbf{d}\mathbf{d}^{\mathrm{T}})\delta\mathbf{p}, \tag{115}$$

$$\Delta\delta\mathbf{d} =\frac{1}{\|\mathbf{p}\|}\left(\Delta\delta\mathbf{p} - \Delta\delta\|\mathbf{p}\|\mathbf{d}\right) + \frac{1}{\|\mathbf{p}\|^2}\left(2\delta\|\mathbf{p}\|\Delta\|\mathbf{p}\|\mathbf{d} - \delta\|\mathbf{p}\|\Delta\mathbf{p} - \Delta\|\mathbf{p}\|\delta\mathbf{p}\right), \tag{116}$$

where

$$\mathbf{p} =\bar{\mathbf{x}}_{,1}\times\bar{\mathbf{x}}_{,2}, \tag{117}$$

$$\delta\mathbf{p} =\delta\bar{\mathbf{x}}_{,1}\times\bar{\mathbf{x}}_{,2} + \bar{\mathbf{x}}_{,1}\times\delta\bar{\mathbf{x}}_{,2}, \tag{118}$$

$$\Delta\delta\mathbf{p} =\delta\bar{\mathbf{x}}_{,1}\times\Delta\bar{\mathbf{x}}_{,2} + \Delta\bar{\mathbf{x}}_{,1}\times\delta\bar{\mathbf{x}}_{,2}, \tag{119}$$

$$\delta\|\mathbf{p}\| =\mathbf{d}\cdot\delta\mathbf{p}, \tag{120}$$

$$\Delta\delta\|\mathbf{p}\| =\Delta\mathbf{d}\cdot\delta\mathbf{p} + \mathbf{d}\cdot\Delta\delta\mathbf{p}. \tag{121}$$

Discretizing $\delta\mathbf{p}$ leads to

$$\delta\mathbf{p}^h = \sum_{I=1}^{n}\mathbf{H}_I\delta\mathbf{u}_I, \tag{122}$$

where

$$\mathbf{H}_I = -N_{I,1}\boldsymbol{\Omega}(\bar{\mathbf{x}}_{,2}) + N_{I,2}\boldsymbol{\Omega}(\bar{\mathbf{x}}_{,1}) \tag{123}$$

and

$$\boldsymbol{\Omega}(\mathbf{h}) = \begin{bmatrix} 0 & -h_3 & h_2 \\ h_3 & 0 & -h_1 \\ -h_2 & h_1 & 0 \end{bmatrix} \tag{124}$$

for any vector $\mathbf{h} = [h_1,\, h_2,\, h_3]^{\mathrm{T}}$.

Discretizing $\Delta\delta\mathbf{p}$ leads to

$$\mathbf{h} \cdot \Delta\delta\mathbf{p}^h = \sum_{I=1}^{n}\sum_{J=1}^{n} \delta\mathbf{u}_I^{\mathrm{T}}\mathbf{L}_{IJ}(\mathbf{h})\Delta\mathbf{u}_J, \tag{125}$$

where

$$\mathbf{L}_{IJ}(\mathbf{h}) = (N_{I,1}N_{J,2} + N_{J,1}N_{I,2})\boldsymbol{\Omega}(\mathbf{h}). \tag{126}$$

Substituting (122) into (115) results in

$$\delta\mathbf{d}^h = \frac{1}{\|\mathbf{p}\|}\sum_{I=1}^{n}(\mathbf{I} - \mathbf{d}\mathbf{d}^{\mathrm{T}})\mathbf{H}_I\delta\mathbf{u}_I. \tag{127}$$

Substituting (122), (125) and (127) into (120) and (121), respectively, results in

$$\delta\|\mathbf{p}\|^h = \sum_{I=1}^{n}\mathbf{d}^{\mathrm{T}}\mathbf{H}_I\delta\mathbf{u}_I, \tag{128}$$

$$\Delta\delta\|\mathbf{p}\|^h = \sum_{I=1}^{n}\sum_{J=1}^{n}\delta\mathbf{u}_I^{\mathrm{T}}\left(\frac{1}{\|p\|}\mathbf{H}_I^{\mathrm{T}}(\mathbf{I} - \mathbf{d}\mathbf{d}^{\mathrm{T}})\mathbf{H}_J + \mathbf{L}_{IJ}(\mathbf{d})\right)\delta\mathbf{u}_J. \tag{129}$$

Substitution of (122), (125), (128) and (129) into (116) leads to

$$\mathbf{h} \cdot \Delta\delta\mathbf{d}^h = \frac{1}{\|\mathbf{p}\|}\sum_{I=1}^{n}\sum_{J=1}^{n}\delta\mathbf{u}_I^{\mathrm{T}}\mathbf{Q}_{IJ}(\mathbf{h})\Delta\mathbf{u}_J, \tag{130}$$

where

$$\mathbf{Q}_{IJ}(\mathbf{h}) = \mathbf{L}_{IJ}(\mathbf{h}) - (\mathbf{d}\cdot\mathbf{h})\left(\frac{1}{\|\mathbf{p}\|}\mathbf{I} - \mathbf{L}_{IJ}(\mathbf{d})\right) + \frac{1}{\|\mathbf{p}\|}\mathbf{H}_I^{\mathrm{T}}((\mathbf{d}\cdot\mathbf{h})\mathbf{d}\mathbf{d}^{\mathrm{T}} - \mathbf{d}\mathbf{h}^{\mathrm{T}} - \mathbf{h}\mathbf{d}^{\mathrm{T}})\mathbf{H}_J. \tag{131}$$

C.2 Matrix formulation

The discretization of the first variation of the membrane strain, $\delta\boldsymbol{\epsilon}^h$, for KL shells is the same as the first equation of (101) for RM shell. Therefore, the nodal strain-displacement matrix for the *membrane* stiffness is given as

$$\mathbf{B}_I^{\mathrm{m}} = \begin{bmatrix} N_{I,1}\bar{\mathbf{x}}_{,1}^{\mathrm{T}} \\ N_{I,2}\bar{\mathbf{x}}_{,2}^{\mathrm{T}} \\ N_{I,2}\bar{\mathbf{x}}_{,1}^{\mathrm{T}} + N_{I,1}\bar{\mathbf{x}}_{,2}^{\mathrm{T}} \end{bmatrix}. \tag{132}$$

Substituting $\bar{\mathbf{x}}^h$ and $\delta\mathbf{d}^h$ into (50), we obtain the discretized first variation of the bending strain as

$$\delta\boldsymbol{\kappa}^h = \sum_{I=1}^{n} \begin{bmatrix} -N_{I,11}\mathbf{d}^{\mathrm{T}} - \frac{1}{\|\mathbf{p}\|}\bar{\mathbf{x}}_{,11}^{\mathrm{T}}(\mathbf{I}-\mathbf{d}\mathbf{d}^{\mathrm{T}})\mathbf{H}_I \\ -N_{I,22}\mathbf{d}^{\mathrm{T}} - \frac{1}{\|\mathbf{p}\|}\bar{\mathbf{x}}_{,22}^{\mathrm{T}}(\mathbf{I}-\mathbf{d}\mathbf{d}^{\mathrm{T}})\mathbf{H}_I \\ -2N_{I,12}\mathbf{d}^{\mathrm{T}} - 2\frac{1}{\|\mathbf{p}\|}\bar{\mathbf{x}}_{,12}^{\mathrm{T}}(\mathbf{I}-\mathbf{d}\mathbf{d}^{\mathrm{T}})\mathbf{H}_I \end{bmatrix} \delta\mathbf{u}_I, \tag{133}$$

$$\delta\boldsymbol{\kappa}^h = \sum_{I=1}^{n} \mathbf{B}_I^{\mathrm{b}}\delta\mathbf{u}_I, \tag{134}$$

where

$$\mathbf{B}_I^{\mathrm{b}} = \begin{bmatrix} -N_{I,11}\mathbf{d}^{\mathrm{T}} - \frac{1}{\|\mathbf{p}\|}\bar{\mathbf{x}}_{,11}^{\mathrm{T}}(\mathbf{I}-\mathbf{d}\mathbf{d}^{\mathrm{T}})\mathbf{H}_I \\ -N_{I,22}\mathbf{d}^{\mathrm{T}} - \frac{1}{\|\mathbf{p}\|}\bar{\mathbf{x}}_{,22}^{\mathrm{T}}(\mathbf{I}-\mathbf{d}\mathbf{d}^{\mathrm{T}})\mathbf{H}_I \\ -2N_{I,12}\mathbf{d}^{\mathrm{T}} - 2\frac{1}{\|\mathbf{p}\|}\bar{\mathbf{x}}_{,12}^{\mathrm{T}}(\mathbf{I}-\mathbf{d}\mathbf{d}^{\mathrm{T}})\mathbf{H}_I \end{bmatrix} \tag{135}$$

is the nodal strain-displacement matrix for *bending* stiffness. Then, substituting $\delta\boldsymbol{\epsilon}^h$ and $\delta\boldsymbol{\kappa}^h$ into the first equation of (49) and (41) leads to the IJth nodal submatrix of the material stiffness matrix as

$$\mathbf{K}_{IJ}^{\mathrm{mat}} = \int_{\Omega} \mathbf{B}_I^{\mathrm{T}}\mathbf{C}^{\mathrm{KL}}\mathbf{B}_J \mathrm{d}\Omega, \tag{136}$$

where

$$\mathbf{B}_I = \mathbf{B}_I^{\mathrm{m}} + \xi^3\mathbf{B}_I^{\mathrm{b}}. \tag{137}$$

The discretized second variation of the membrane strain, $\Delta\delta\boldsymbol{\epsilon}^h$, for KL shells is the same as the first equation of (102). Substituting $\bar{\mathbf{x}}^h$, $\delta\mathbf{d}^h$ and $\Delta\delta\mathbf{d}^h$ into (51), we obtain the discretized second variation of the bending strain as

$$\Delta\delta\boldsymbol{\kappa}^h = \begin{bmatrix} \Delta\delta\kappa_{11}^h \\ \Delta\delta\kappa_{22}^h \\ 2\Delta\delta\kappa_{12}^h \end{bmatrix}, \tag{138}$$

where

$$\Delta\delta\kappa_{\alpha\beta}^h = \frac{1}{\|\mathbf{p}\|}\sum_{I=1}^{n}\sum_{J=1}^{n} \delta\mathbf{u}_I^{\mathrm{T}}\left(N_{I,\alpha\beta}\left(\mathbf{I}-\mathbf{d}\mathbf{d}^{\mathrm{T}}\right)\mathbf{H}_J + N_{J,\alpha\beta}\mathbf{H}_I^{\mathrm{T}}\left(\mathbf{I}-\mathbf{d}\mathbf{d}^{\mathrm{T}}\right) + \mathbf{Q}_{IJ}(\bar{\mathbf{x}}_{,\alpha\beta})\right)\Delta\mathbf{u}_I. \tag{139}$$

Substitution of the first equation of (102) and (138) into the second equation of (49) and (41) leads to the IJth nodal submatrix of the geometric stiffness matrix as

$$\mathbf{K}_{IJ}^{\mathrm{geom}} = \int_A \mathbf{K}_{IJ_{11}}^{\mathrm{geom}} + \mathbf{K}_{IJ_{22}}^{\mathrm{geom}} + \mathbf{K}_{IJ_{12}}^{\mathrm{geom}} \mathrm{d}\Omega, \tag{140}$$

where

$$\mathbf{K}_{IJ_{11}}^{\text{geom}} = \left(N_{I,1}N_{J,1}\mathbf{I} + \frac{\xi^3}{\|\mathbf{p}\|} \left(N_{I,11} \left(\mathbf{I} - \mathbf{d}\mathbf{d}^{\mathrm{T}} \right) \mathbf{H}_J + N_{J,11}\mathbf{H}_I^{\mathrm{T}} \left(\mathbf{I} - \mathbf{d}\mathbf{d}^{\mathrm{T}} \right) + \mathbf{Q}_{IJ}(\bar{\mathbf{x}}_{,11}) \right) \right) \tilde{S}^1, \quad (141)$$

$$\mathbf{K}_{IJ_{22}}^{\text{geom}} = \left(N_{I,2}N_{J,2}\tilde{S}_m^2\mathbf{I} + \frac{\xi^3}{\|\mathbf{p}\|} \left(N_{I,22} \left(\mathbf{I} - \mathbf{d}\mathbf{d}^{\mathrm{T}} \right) \mathbf{H}_J + N_{J,22}\mathbf{H}_I^{\mathrm{T}} \left(\mathbf{I} - \mathbf{d}\mathbf{d}^{\mathrm{T}} \right) + \mathbf{Q}_{IJ}(\bar{\mathbf{x}}_{,22}) \right) \right) \tilde{S}^2, \quad (142)$$

$$\mathbf{K}_{IJ_{12}}^{\text{geom}} = \left(N_{I,2}N_{J,1}\tilde{S}_m^3\mathbf{I} + \frac{2\xi^3}{\|\mathbf{p}\|} \left(N_{I,12} \left(\mathbf{I} - \mathbf{d}\mathbf{d}^{\mathrm{T}} \right) \mathbf{H}_J + N_{J,12}\mathbf{H}_I^{\mathrm{T}} \left(\mathbf{I} - \mathbf{d}\mathbf{d}^{\mathrm{T}} \right) + \mathbf{Q}_{IJ}(\bar{\mathbf{x}}_{,12}) \right) \right) \tilde{S}^3. \quad (143)$$

Here $\tilde{S}^i$ is the ith component of $\tilde{\mathbf{S}}$ calculated by

$$\tilde{\mathbf{S}} = \mathbf{C}^{\mathrm{KL}}(\boldsymbol{\epsilon} + \xi^3\boldsymbol{\kappa}). \quad (144)$$

The nodal internal force vector $\mathbf{F}_I^{\text{int}}$ is defined as

$$\mathbf{F}_I^{\text{int}} = \int_\Omega \mathbf{B}_I^{\mathrm{T}}\tilde{\mathbf{S}}\,\mathrm{d}\Omega. \quad (145)$$

References

[1] E. Ramm, Form und Tragverhalten, in: E. Ramm, E. Schunck (Eds.), Heinz Isler Schalen, Karl Krämer Verlag: Stuttgart, 29–34, 1986.

[2] E. Ramm, W. A. Wall, Shell Structures—a Sensitive Interrelation between Physics and Numerics, International Journal for Numerical Methods in Engineering 60 (1) (2004) 381–427.

[3] T. J. R. Hughes, J. A. Cottrell, Y. Bazilevs, Isogeometric Analysis: CAD, Finite Elements, NURBS, Exact Geometry and Mesh Refinement, Computer Methods in Applied Mechanics and Engineering 194 (39) (2005) 4135–4195.

[4] L. Piegl, W. Tiller, The NURBS Book, Springer-Verlag, New York, 1997.

[5] X. Li, T. W. Sederberg, S-Splines: A Simple Surface Solution for IGA and CAD, Computer Methods in Applied Mechanics and Engineering 350 (2019) 664–678.

[6] T. Sederberg, J. Zheng, A. Bakenov, A. Nasri, T-Splines and T-NURCCs, in: ACM SIGGRAPH 2003 Papers, SIGGRAPH '03, ACM, New York, NY, USA, 477–484, 2003.

[7] D. Thomas, L. Engvall, S. Schmidt, K. Tew, M. Scott, U-Splines: Spline over Unstructured Meshes, Preprint, https://coreform.com/usplines .

[8] J. Warren, H. Weimer, Subdivision Methods for Geometric Design, Morgan Kaufmann Publishers, San Francisco, 2002.

[9] J. Kiendl, K.-U. Bletzinger, J. Linhard, R. Wüchner, Isogeometric shell analysis with Kirchhoff-Love elements, Computer Methods in Applied Mechanics and Engineering 198 (49-52) (2009) 3902–3914.

[10] D. J. Benson, Y. Bazilevs, M. C. Hsu, T. J. R. Hughes, A large deformation, rotation-free, isogeometric shell, International Journal for Numerical Methods in Engineering, 200 (2011) 1367 – 1378.

[11] D. J. Benson, Y. Bazilevs, M. C. Hsu, T. J. R. Hughes, Isogeometric shell analysis: The Reissner-Mindlin shell, Computer Methods in Applied Mechanics and Engineering 199 (5-8) (2010) 276–289.

[12] R. Echter, B. Oesterle, M. Bischoff, A hierarchic family of isogeometric shell finite elements, Computer Methods in Applied Mechanics and Engineering 254 (2013) 170–180.

[13] D. Benson, S. Hartmann, Y. Bazilevs, M.-C. Hsu, T. J. R. Hughes, Blended Isogeometric Shells, Computer Methods in Applied Mechanics and Engineering 255 (2013) 133–146.

[14] C. Adam, S. Bouabdallah, M. Zarroug, H. Maitournam, Improved Numerical Integration for Locking Treatment in Isogeometric Structural Elements. Part II: Plates and Shells, Computer Methods in Applied Mechanics and Engineering 284 (2015) 106–137.

[15] C. Adam, S. Bouabdallah, M. Zarroug, H. Maitournam, Improved Numerical Integration for Locking Treatment in Isogeometric Structural Elements, Part I: Beams, Computer Methods in Applied Mechanics and Engineering 279 (2014) 1–28.

[16] S. Bieber, B. Oesterle, E. Ramm, M. Bischoff, A Variational Method to Avoid Locking—Independent of the Discretization Scheme, International Journal for Numerical Methods in Engineering 114 (8) (2018) 801–827.

[17] Z. Zou, M. A. Scott, D. Miao, M. Bischoff, B. Oesterle, W. Dornisch, An Isogeometric Reissner–Mindlin Shell Element Based on Bézier Dual Basis Functions: Overcoming Locking and Improved Coarse Mesh Accuracy, Computer Methods in Applied Mechanics and Engineering 370 (2020) 113283.

[18] L. Beirão Da Veiga, T. J. R. Hughes, J. Kiendl, C. Lovadina, J. Niiranen, A. Reali, H. Speleers, A Locking-Free Model for Reissner–Mindlin Plates: Analysis and Isogeometric Implementation via NURBS and Triangular NURPS, Mathematical Models and Methods in Applied Sciences 25 (08) (2015) 1519–1551.

[19] T. J. R. Hughes, M. Cohen, M. Haroun, Reduced and Selective Integration Techniques in the Finite Element Analysis of Plates, Nuclear Engineering and Design 46 (1) (1978) 203–222.

[20] T. J. Hughes, R. L. Taylor, W. Kanoknukulchai, A simple and efficient finite element for plate bending, International Journal for Numerical Methods in Engineering 11 (10) (1977) 1529–1543.

[21] R. Bouclier, T. Elguedj, A. Combescure, Locking Free Isogeometric Formulations of Curved Thick Beams, Computer Methods in Applied Mechanics and Engineering 245-246 (2012) 144–162.

[22] D. Miao, M. Borden, M. Scott, D. Thomas, Bézier $\bar{\text{B}}$ Projection, Computer Methods in Applied Mechanics and Engineering 335 (2018) 273–297.

[23] S. Lee, J. Rhiu, A New Efficient Approach to the Formulation of Mixed Finite Element Models for Structural Analysis, International Journal for Numerical Methods in Engineering 23 (9) (1986) 1629–1641.

[24] W. Wagner, F. Gruttmann, A Robust Non-Linear Mixed Hybrid Quadrilateral Shell Element, International Journal for Numerical Methods in Engineering 64 (5) (2005) 635–666.

[25] S. Klinkel, F. Gruttmann, W. Wagner, A Mixed Shell Formulation Accounting for Thickness Strains and Finite Strain 3d Material Models, International Journal for Numerical Methods in Engineering 74 (6) (2008) 945–970.

[26] R. Bouclier, T. Elguedj, A. Combescure, Efficient Isogeometric NURBS-Based Solid-Shell Elements: Mixed Formulation and $\bar{\text{B}}$ -Method, Computer Methods in Applied Mechanics and Engineering 267 (2013) 86–110.

[27] B. Oesterle, R. Sachse, E. Ramm, M. Bischoff, Hierarchic isogeometric large rotation shell elements including linearized transverse shear parametrization, Computer Methods in Applied Mechanics and Engineering 321 (2017) 383–405.

[28] O. Zienkiewicz, R. Taylor, J. Too, Reduced Integration Technique in General Analysis of Plates and Shells, International Journal for Numerical Methods in Engineering 3 (2) (1971) 275–290.

[29] T. J. R. Hughes, R. L. Taylor, W. Kanoknukulchai, A Simple and Efficient Finite Element for Plate Bending, International Journal for Numerical Methods in Engineering 11 (10) (1977) 1529–1543.

[30] W. Dornisch, R. Müller, S. Klinkel, An Efficient and Robust Rotational Formulation for Isogeometric Reissner–Mindlin Shell Elements, Computer Methods in Applied Mechanics and Engineering 303 (2016) 1–34.

[31] T. J. R. Hughes, T. E. Tezduyar, Finite Elements Based upon Mindlin Plate Theory with Particular Reference to the Four-Node Bilinear Isoparametric Element, Journal of Applied Mechanics 48 (3) (1981) 587.

[32] H. C. Huang, E. Hinton, A New Nine Node Degenerated Shell Element with Enhanced Membrane and Shear Interpolation, International Journal for Numerical Methods in Engineering 22 (1) (1986) 73–92.

[33] K. Park, G. Stanley, A Curved C^0 Shell Element Based on Assumed Natural-Coordinate Strains, Journal of Applied Mechanics 53 (2) (1986) 278.

[34] K.-J. Bathe, E. Dvorkin, A Formulation of General Shell Elements—the Use of Mixed Interpolation of Tensorial Components, International Journal for Numerical Methods in Engineering 22 (3) (1986) 697–722.

[35] K.-U. Bletzinger, M. Bischoff, E. Ramm, A Unified Approach for Shear-Locking-Free Triangular and Rectangular Shell Finite Elements, Computers and Structures (2000) 14.

[36] F. Koschnick, M. Bischoff, N. Camprubí, K.-U. Bletzinger, The Discrete Strain Gap Method and Membrane Locking, Computer Methods in Applied Mechanics and Engineering 194 (21-24) (2005) 2444–2463.

[37] J. F. Caseiro, R. A. F. Valente, A. Reali, J. Kiendl, F. Auricchio, R. J. Alves de Sousa, On the Assumed Natural Strain Method to Alleviate Locking in Solid-Shell NURBS-Based Finite Elements, Computational Mechanics 53 (6) (2014) 1341–1353.

[38] N. Büchter, E. Ramm, D. Roehl, Three-Dimensional Extension of Non-Linear Shell Formulation Based on the Enhanced Assumed Strain Concept, International Journal for Numerical Methods in Engineering 37 (15) (1994) 2551–2568.

[39] M. Bischoff, E. Ramm, Shear deformable shell elements for large strains and rotations, International Journal for Numerical Methods in Engineering 40 (23) (1997) 4427–4449.

[40] C. Adam, T. J. R. Hughes, S. Bouabdallah, M. Zarroug, H. Maitournam, Selective and Reduced Numerical Integrations for NURBS-Based Isogeometric Analysis, Computer Methods in Applied Mechanics and Engineering 284 (2015) 732–761.

[41] R. Echter, M. Bischoff, Numerical Efficiency, Locking and Unlocking of NURBS Finite Elements, Computer Methods in Applied Mechanics and Engineering 199 (5-8) (2010) 374–382.

[42] T. J. R. Hughes, A. Reali, G. Sangalli, Efficient Quadrature for NURBS-Based Isogeometric Analysis, Computer Methods in Applied Mechanics and Engineering 199 (5) (2010) 301–313.

[43] K. A. Johannessen, Optimal Quadrature for Univariate and Tensor Product Splines, Computer Methods in Applied Mechanics and Engineering 316 (2017) 84–99.

[44] F. Auricchio, F. Calabrò, T. J. R. Hughes, A. Reali, G. Sangalli, A Simple Algorithm for Obtaining Nearly Optimal Quadrature Rules for NURBS-Based Isogeometric Analysis, Computer Methods in Applied Mechanics and Engineering 249-252 (2012) 15–27.

[45] M. Bartoň, R. Ait-Haddou, V. M. Calo, Gaussian Quadrature Rules for C^1 Quintic Splines with Uniform Knot Vectors, Journal of Computational and Applied Mathematics 322 (2017) 57–70.

[46] R. Ait-Haddou, M. Bartoň, V. M. Calo, Explicit Gaussian Quadrature Rules for C^1 Cubic Splines with Symmetrically Stretched Knot Sequences, Journal of Computational and Applied Mathematics 290 (2015) 543–552.

[47] M. Bartoň, V. M. Calo, Gaussian Quadrature for Splines via Homotopy Continuation: Rules for C^2 Cubic Splines, Journal of Computational and Applied Mathematics 296 (2016) 709–723.

[48] F. Calabrò, G. Sangalli, M. Tani, Fast Formation of Isogeometric Galerkin Matrices by Weighted Quadrature, Computer Methods in Applied Mechanics and Engineering 316 (2017) 606–622.

[49] D. Schillinger, S. J. Hossain, T. J. R. Hughes, Reduced Bézier Element Quadrature Rules for Quadratic and Cubic Splines in Isogeometric Analysis, Computer Methods in Applied Mechanics and Engineering 277 (2014) 1–45.

[50] S. Klinkel, L. Chen, W. Dornisch, A NURBS Based Hybrid Collocation–Galerkin Method for the Analysis of Boundary Represented Solids, Computer Methods in Applied Mechanics and Engineering 284 (2015) 689–711.

[51] D. Schillinger, M. J. Borden, H. K. Stolarski, Isogeometric collocation for phase-field fracture models, Computer Methods in Applied Mechanics and Engineering 284 (2015) 583–610.

[52] D. Schillinger, J. A. Evans, A. Reali, M. A. Scott, T. J. R. Hughes, Isogeometric Collocation: Cost comparison with Galerkin methods and extension to adaptive hierarchical NURBS discretizations, Computer Methods in Applied Mechanics and Engineering 267 (2013) 170 – 232.

[53] F. Auricchio, L. Beirao de Veiga, T. J. R. Hughes, A. Reali, G. Sangalli, Isogeometric collocation for elastostatics and explicit dynamics, ICES Report 12-07 .

[54] F. Auricchio, L. B. Da Veiga, T. J. R. Hughes, A. Reali, G. Sangalli, Isogeometric Collocation for Methods, Mathematical models & methods in applied sciences 20 (11) (2010) 2075–2107.

[55] R. W. Johnson, Higher Order B-Spline Collocation at the Greville Abscissae, Applied Numerical Mathematics 52 (1) (2005) 63–75.

[56] F. Maurin, F. Greco, L. Coox, D. Vandepitte, W. Desmet, Isogeometric Collocation for Kirchhoff–Love Plates and Shells, Computer Methods in Applied Mechanics and Engineering 329 (2018) 396–420.

[57] Z. Zou, Isogeometric Shell Analysis: Multi-patch Coupling and Overcoming Locking, Ph.D. thesis, Brigham Young University, Provo, 2020.

[58] W. J. Gordon, R. F. Riesenfeld, B-Spline Curves and Surfaces, in: Computer Aided Geometric Design, Elsevier, 95–126, 1974.

[59] D. R. Forsey, R. H. Bartels, Hierarchical B-spline refinement, ACM SIGGRAPH Computer Graphics 22 (4) (1988) 205–212, ISSN 0097-8930.

[60] M. Bischoff, W. A. Wall, K. U. Bletzinger, E. Ramm, Models and Finite Elements for Thin-walled Structures, in: E. Stein, R. de Borst, T. J. R. Hughes (Eds.), Encyclopedia of Computational Mechanics, Vol. 2, Solids, Structures and Coupled Problems, chap. 3, Wiley, 59–137, 2004.

[61] T. J. R. Hughes, The Finite Element Method: Linear Static and Dynamic Finite Element Analysis, Dover Publications, Mineola, NY, 2000.

[62] F. Gruttmann, R. Sauer, W. Wagner, Theory and Numerics of Three-dimensional Beams with Elastoplastic Material Behaviour, International Journal for Numerical Methods in Engineering 48 (12) (2000) 1675–1702.

[63] S. Hubrich, P. Di Stolfo, L. Kudela, S. Kollmannsberger, E. Rank, A. Schröder, A. Düster, Numerical Integration of Discontinuous Functions: Moment Fitting and Smart Octree, Computational Mechanics 60 (5) (2017) 863–881.

[64] M. Joulaian, S. Hubrich, A. Düster, Numerical Integration of Discontinuities on Arbitrary Domains Based on Moment Fitting, Computational Mechanics 57 (6) (2016) 979–999.

[65] G. Strang, G. Fix, An Analysis of the Finite Element Method, Wellesley-Cambridge Press, Wellesley, Mass, 2nd edition edn., 2008.

[66] T. J. Hughes, J. A. Evans, A. Reali, Finite Element and NURBS Approximations of Eigenvalue, Boundary-Value, and Initial-Value Problems, Computer Methods in Applied Mechanics and Engineering 272 (2014) 290–320.

[67] D. C. Thomas, M. A. Scott, J. A. Evans, K. Tew, E. J. Evans, Bézier projection: a unified approach for local projection and quadrature-free refinement and coarsening of NURBS and T-splines with particular application to isogeometric design and analysis, Computer Methods in Applied Mechanics and Engineering 284 (2015) 55–105.

[68] Z. Zou, M. A. Scott, M. J. Borden, D. C. Thomas, W. Dornisch, E. Brivadis, Isogeometric Bézier Dual Mortaring: Refineable Higher-Order Spline Dual Bases and Weakly Continuous Geometry, Computer Methods in Applied Mechanics and Engineering 333 (2018) 497–534.

[69] D. Miao, Z. Zou, M. A. Scott, M. J. Borden, D. C. Thomas, Isogeometric Bézier Dual Mortaring: The Enriched Bézier Dual Basis with Application to Second- and Fourth-Order Problems, Computer Methods in Applied Mechanics and Engineering 363 (2020) 112900.

[70] S. Timoshenko, S. Woinowsky-Krieger, Theory of Plates and Shells, McGraw-Hill College, New York, 2 edition edn., 1959.

[71] R. Macneal, R. Harder, A Proposed Standard Set of Problems to Test Finite Element Accuracy, Finite Elements in Analysis and Design 1 (1) (1985) 3–20.

[72] L. Greco, M. Cuomo, L. Contrafatto, A Reconstructed Local $\bar{\mathrm{B}}$ Formulation for Isogeometric Kirchhoff–Love Shells, Computer Methods in Applied Mechanics and Engineering 332 (2018) 462–487.

[73] K. Y. Sze, X. H. Liu, S. H. Lo, Popular Benchmark Problems for Geometric Nonlinear Analysis of Shells, Finite Elements in Analysis and Design 40 (11) (2004) 1551–1569.

[74] T. X. Duong, F. Roohbakhshan, R. A. Sauer, A New Rotation-Free Isogeometric Thin Shell Formulation and a Corresponding Continuity Constraint for Patch Boundaries, Computer Methods in Applied Mechanics and Engineering 316 (2017) 43–83.

[75] R. MacNeal, Finite Elements: Their Design and Performance, M. Dekker, New York, 1994.

[76] R. A. Sauer, T. X. Duong, On the Theoretical Foundations of Thin Solid and Liquid Shells, Mathematics and Mechanics of Solids 22 (3) (2017) 343–371.

[77] R. A. Sauer, T. X. Duong, C. J. Corbett, A Computational Formulation for Constrained Solid and Liquid Membranes Considering Isogeometric Finite Elements, Computer Methods in Applied Mechanics and Engineering 271 (2014) 48–68.

[78] W. Dornisch, S. Klinkel, B. Simeon, Isogeometric Reissner–Mindlin Shell Analysis with Exactly Calculated Director Vectors, Computer Methods in Applied Mechanics and Engineering 253 (2013) 491–504.

[79] J. Kiendl, M.-C. Hsu, M. C. H. Wu, A. Reali, Isogeometric Kirchhoff–Love Shell Formulations for General Hyperelastic Materials, Computer Methods in Applied Mechanics and Engineering 291 (2015) 280–303.